ELECTRODEPOSITION OF METAL ON GALLIUM ARSENIDE NANOWIRES

by

Chao Liu
B.Sc., Shandong Normal University, 2008

A THESIS SUBMITTED IN PARTIAL FULFILLMENT OF
THE REQUIREMENTS FOR THE DEGREE OF

MASTER OF SCIENCE

In the
Department of Physics
Faculty of Science

SIMON FRASER UNIVERSITY

Summer 2011

APPROVAL

Name: **Chao Liu**

Degree: **Master of Science**

Title of Thesis: **Electrodeposition of Metal on Gallium Arsenide Nanowires**

Examining Committee:

Chair: **Dr. J. Steven Dodge**
Associate Professor, Physics

_____

Dr. Karen Kavanagh
Senior Supervisor
Professor, Physics

_____

Dr. Simon Watkins
Supervisor
Professor, Physics

_____

Dr. Patricia Mooney
Supervisor
Professor, Physics

_____

Dr. Erol Girt
Internal Examiner
Associate Professor, Physics

Date Defended/Approved: June 27, 2011

ABSTRACT

In the majority of reported studies, metal contacts to semiconductor nanowires (NWs) have been fabricated using high-resolution electron-beam lithography with metal evaporation. In our study, copper (Cu) or iron (Fe) electrical contacts to as-grown gallium arsenide (GaAs) nanowires have been fabricated via electrodeposition. For nominally undoped GaAs nanowires, we find that Cu or Fe has a preference for nucleation and growth on the gold catalyst avoiding the sidewalls. For carbon-doped nanowires with higher conductivity, Cu nucleation and growth began to occur on the sidewalls as well as on the gold catalyst. COMSOL finite element analysis, carried out to simulate the experimental results, was used to discuss the growth mechanism in terms of nanowire sample surface, conductivity and morphology.

Keywords: nanowire; electrodeposition; GaAs; conductivity

心随野鹤白云外,

梦卧宙宇千年间.

Hello World, I am coming.

L.Y.C @ 2011

ACKNOWLEDGEMENTS

First and foremost I would like to thank my senior supervisor, Dr. Karen Kavanagh, who has supported and encouraged me throughout my graduate career. My first project did not go well for the first year, Dr. Kavanagh proposed this new project idea and provided lots of valuable academic insights and editorial comments during the research. I especially thank her for providing me opportunities to present my work at international conferences, helping me improve my English and presentation skills.

I would also like to thank Dr. Simon Watkins and his graduate student Omid Salehzadeh Einabad, for their collaboration, support and scientific suggestions regarding my work. This work could not be done without their constant supply of experimental samples.

I would also like to acknowledge past and present members of the Kavanagh lab, Dr. Zhiliang Bao and Dr. Wenjie Li, especially Sarmita Majumder, who offered helpful guidance and taught me to be patient and careful for the electrodeposition experiment.

I also thank Dr. Patricia Mooney and Dr. Erol Girt, for the valuable discussion about trend and lifestyle in academia and industry. Finally, I would like to thank my close friends and family, in Canada and China, who were always there to encourage me.

I am grateful to the Physics department, as a small and comfort community, provided me a memorable learning experience and I do enjoy my days in SFU physics.

My dream is to build a high-tech company before I turn 35, the graduate study experience will help me along the way chasing my dreams.

TABLE OF CONTENTS

Approval ii
Abstract iii
Dedication iv
Acknowledgements v
Table of Contents vii
List of Figures ix
List of Tables xii

Introduction 1

1: Electrodeposition 3
1.1 Electrodeposition overview 3
1.1.1 Nernst's equation and overpotential 4
1.1.2 Butler-Volmer equation 5
1.2 Electrode/electrolyte interface 6
1.2.1 Metal/electrolyte interfaces 6
1.2.2 Semiconductor/electrolyte interfaces 8
1.3 Previous work on electrodeposited epitaxial metal on GaAs 9
1.4 Electrodeposition setup 10
1.5 Experimental parameters: current density and initial voltage 12
1.6 Experimental procedures 12

2: Nanowire Samples 15
2.1 NW samples 15
2.2 Wettability of sample surfaces 17
2.2.1 As-received sample surfaces 18
2.2.2 GaAs NW surfaces after ammonium hydroxide etching 20
2.3 Removal of gold 21
2.4 Light-assisted electrodeposition 24
2.5 Electrodeposition of metal on InAs NWs 25

3: Results 27
3.1 Electrodeposition of Cu on GaAs NWs 27
3.1.1 Unintentionally-doped GaAs NWs - Type A Ga precursor (TEGa) 27
3.1.2 Unintentionally-doped GaAs NWs: Type B Ga precursor (TMGa) 29
3.2 GaAs NWs intentionally doped with carbon 31
3.2.1 Type A TEGa precursor 32
3.2.2 Carbon-doped GaAs NWs with Type B (TMGa) precursors 37
3.2.1 Core-shell (Type B -Type A) GaAs NWs 38

3.3 Electrodeposition of Fe on GaAs nanowires 40
3.4 Electrodeposition of metal on InAs nanowires 45
3.4.1 NRC InAs NWs 45
3.4.2 Electrodeposition of Cu on InAs NWs from Dr. Watkins' group 49
3.5 Experiment with light illumination 49
3.6 Metal deposition without gold catalyst 50
3.6.1 Electrodeposition of Cu on gold nanoparticle samples 50
3.6.2 Cu growth without gold catalyst 51

4: Discussion 56
4.1 Current and resistivity calculation 56
4.2 COMSOL simulation 61
4.2.1 Cu deposition on InAs NWs 62
4.2.2 Electric field simulation for low conductivity GaAs NWs 67
4.3 Other factors important to metal nucleation 73
4.3.1 Geometry and depletion width 73
4.3.2 Gold catalysts 74
4.3.3 Overpotential 74
4.4 Sample surface 76
4.4.1 Surface oxidation 76
4.4.2 Incorporation of carbon 77
4.5 Cu contact for *I-V* measurement 77

5: Summary 79

Appendices 82
Appendix A : Potential time relation 82

Bibliography 87

LIST OF FIGURES

Figure 1.1: Schematic diagram of an electrodeposition cell. 3
Figure 1.2: Schematic diagram of a double layer on an electrode 7
Figure 1.3: Potential drop at the semiconductor-electrolyte interface (schematic). 9
Figure 1.4: (a) XRD θ-2θ scans of Cu/GaAs deposited at 53°C onto (001) oriented substrate and (b) SEM image of the sample surface. [9] 10
Figure 1.5: Schematic diagram of the electrodeposition setup. 11
Figure 1.6: Schematic diagram of a sample prepared with photoresist masking.. 12
Figure 2.1: Illustration of the contact angle of a liquid droplet on a substrate. 17
Figure 2.2: Tilted-view SEM images of different as-received sample surfaces 19
Figure 2.3 Plots of contact angle versus NW (a) diameter, (b) length, and (c) density and (d) sample gold thickness 20
Figure 2.4: SEM images before and after gold etching in KI/I_2 solutions.. 23
Figure 2.5: Transmission intensity for a LED flashlight measured in air and through a Kimax glass beaker. 25
Figure 3.1: SEM images of Type A GaAs NWs before (left) and after (right) electrodeposition of Cu for 40 s. 27
Figure 3.2: TEM bright field images of a Types A GaAs NW 29
Figure 3.3: BF TEM images of Type A GaAs NWs grown without CBr_4 30
Figure 3.4: SEM images of GaAs NWs before (a) and after (b, c) Cu electrodeposition for 30 s. 31
Figure 3.5: SEM images of Type A intentionally carbon-doped GaAs NWs before (left) and after (right) electrodeposition of Cu for 40 s. 33
Figure 3.6: TEM images of Type A intentionally carbon-doped GaAs NWs after deposition of Cu.. 33
Figure 3.7: TEM bright field image (left) of one GaAs NW and its dark field image (right) from a Cu diffraction spot 34
Figure 3.8: TEM bright field images of GaAs NWs after electrodeposition of Cu for 40 s (left) and 80 s (right). 34
Figure 3.9: Top: TEM images of GaAs NWs after electrodeposition of Cu for 80 s.. 36
Figure 3.10: SEM images of GaAs NWs (Type A carbon-doped) with large diameters after deposition of Cu for 40s. 37

Figure 3.11: SEM images of GaAs NWs before (a) and after (b,c) electrodeposition of Cu for 30 s. 38
Figure 3.12: SEM images of undoped core, carbon-doped shell GaAs NWs before (left) and after (right) electrodeposition of Cu for 40 s. 39
Figure 3.13: Plot of Cu diameter on the sides of the NW vs. NW diameter. 39
Figure 3.14: SEM images of GaAs NWs before (left) and after (right) electrodeposition of Fe for 30 s. 40
Figure 3.15: Plot of calculated Fe nanoparticle volume as a function of NW diameter. 41
Figure 3.16: TEM images of the GaAs NW after deposition of Fe for 30 s. 42
Figure 3.17: STEM image of a GaAs NW after deposition of Fe. 43
Figure 3.18: A STEM image of the Au end of another wire electrodeposited with Fe and EDS pattern. 44
Figure 3.19: SEM images of InAs NWs from NRC obtained from two regions of the same SiO_2/InP patterned wafer 45
Figure 3.20: SEM image of one InAs NW growing through a SiO_2 masked InP substrate.. 46
Figure 3.21: SEM images of InAs NWs with different array sizes after electrodeposition of Cu for 30 s. 47
Figure 3.22: Left: SEM image of one of the InAs NW after deposition of Cu. Right: EDS spectrum of the red area shown in (a). 47
Figure 3.23: SEM images (45 ° tilted) of InAs NWs after electrodeposition of Fe for 30 s. 48
Figure 3.24: SEM images of InAs NWs before (a) and after (b) electrodeposition of Cu for 40 s. 49
Figure 3.25: SEM images of GaAs NWs after electrodeposition of Cu for 30 s. 50
Figure 3.26: SEM images of Cu deposition on a gold nanoparticle/GaAs substrate sample as a function of deposition time. 51
Figure 3.27: SEM images of carbon-doped GaAs NWs (Type A) after 40 s electrodeposition of Cu. 53
Figure 3.28: TEM images of GaAs NWs where the Au was etched prior to electrodeposition of Cu (40 s). 54
Figure 3.29: TEM bright field image of a ZB GaAs NW with associated SAD pattern.. 55
Figure 3.30: Potential change as a function of deposition time. 86
Figure 4.1: (a) NW current and calculated resistivity versus NW diameter and (b) current versus NW cross-sectional area for Cu deposition. 58
Figure 4.2: Calculated current versus NW diameter (a) and NW cross-sectional area (b) for Fe deposition 61
Figure 4.3: Sketch of the simulation deposition cell. 63
Figure 4.4: Copper ion concentration (mol/m^3), isopotential lines (black), total flux stream lines (white), and electrode displacement in the cell after 1 second of operation. 66

Figure 4.5: Copper ion concentration (mol/m^3), isopotential lines, total flux stream lines, and electrode displacement in the cell after (a) 2 s, (b) 3 s, (c) 4 s and (d) 5 s of operation. 67

Figure 4.6: GaAs NW sample sketch and lightning rod picture. 68

Figure 4.7: Geometry of the electrolytic cell. 69

Figure 4.8: Simulation results of (a) current density (A/m^2) and (b) electric field (V/m) distribution 71

Figure 4.9: Simulation results of (a) current density (A/m^2) and (b) electric field (V/m) distribution in the cell for GaAs NWs with conductivity 10^6 S/m. 72

Figure 4.10: SEM image of GaAs NWs after Cu deposition for 5 s with 40 mA/mm^2 75

Figure 4.11: SEM images of a nanoprobe touching electrodeposited Cu on a GaAs NW head. 78

Figure 5.1: Sketch of low-doped NW sample before and after electrodeposition. 79

Figure 5.2: Sketch of highly-doped NW sample before and after electrodeposition. 80

LIST OF TABLES

Table 2.1: Summary of NW samples deposited in this work. 16

Table 2.2 The liquid-vapour interfacial energy density (surface tension) for water-air, ethanol-air and 9.6% Aqueous ammonia (ammonium hydroxide) – air interfaces at room temperature. [15] 21

INTRODUCTION

Semiconductor nanowires have attracted wide attention as building blocks for the next generation of nanoelectronic components or solar cells. While significant work had been done on the bottom up fabrication of these one-dimensional nanostructures, direct assembling or incorporating nanowires into nanosystems is important both for characterization and for creating new functionality.

Various methods have been developed to assemble metal contacts onto semiconductor NWs. There are two different kinds: end bonded or side contacts. A common method for both types is to disperse the NWs onto an insulating substrate with pre-patterned alignment markers and then fabricate the contacts through electron beam lithography and metal evaporation [1][2][3]. Such contacts have also been achieved by electrodeposition onto NWs dispersed onto pre-patterned metal electrodes [4] or directly on the ends or sidewalls with the NWs still attached to the growth substrate [5].

In this work we studied the assembly of copper (Cu) and iron (Fe) contacts on as-grown, GaAs and InAs vertical NWs using electrodeposition. During deposition, the whole NW is surrounded by electrolyte, which makes both end and side contacts possible under certain conditions. The experimental methods and some previous experimental results on electrodeposition of metal on GaAs bulk sample will be reviewed briefly in Chapter 1. Chapter 2 will discuss the electrodeposition experimental details, and sample preparation including evaluating the wettability of NW surfaces. We will present the

experimental results in Chapter 3 and the analysis of the growth mechanisms in Chapter 4 in terms of NW conductivity, morphology and surface oxidation.

1: ELECTRODEPOSITION

1.1 Electrodeposition overview

Electrodeposition is the process of reducing metal ions into a solid by supplying electrons to the electrode. A typical electrochemical cell consists of two electrodes immersed in an electrolyte with a DC power supply connected to both electrodes. A schematic of the set-up for Cu deposition on our GaAs NW sample is shown in Figure 1.1 where the electrolyte consists of copper sulphate ($CuSO_4$) dissolved in de-ionized water.

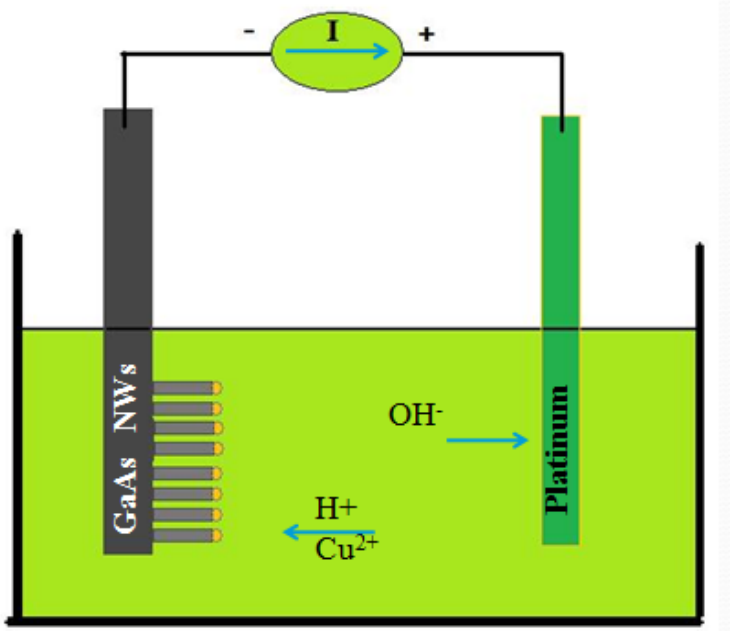

Figure 1.1: Schematic diagram of an electrodeposition cell. Galvanostatic electrodeposition uses a constant current source with two electrodes: cathode and anode.

At the cathode (GaAs NW sample), positively charged ions (H^+ and Cu^{2+}) are attracted to the sample surface, reduced, and bonded to form a solid on the electrode (Cu) or evolve as gas (H_2). While at the anode (platinum), negatively charged ions (SO_4^{2-} and OH^-) are attracted and become oxidized. The major reactions can be written as:

Cathode: $Cu^{2+} + 2e^- \rightarrow Cu$ (1.1)

Anode: $4OH^- - 4e^- \rightarrow O_2 + 2H_2O$ (1.2)

In our experiment, we used a constant current power source (galvanostatic electrodeposition). Many researchers use a constant voltage power source (potentiostatic electrodeposition), where an extra reference electrode is used to control the cathode voltage. That works best when the cathode is a good conductor with a reproducible, low resistance contact. In our case, variations in both the bulk resistivity of the GaAs cathode and the resistance of its ohmic contact meant that the control of current maintained a constant voltage drop and flux of ions within the electrolyte.

1.1.1 Nernst's equation and overpotential

Based on the principle of microscopic reversibility in electrochemistry, there is a reverse reaction occurring during Cu deposition:

$$Cu \rightarrow Cu^{2+} + 2e^- \quad (1.3)$$

The Nernst equation gives the cathode potential required at equilibrium, E_{eq},, i.e. when no net current is flowing across the electrode/electrolyte interface [6]:

$$E_{eq} = E_0 + \frac{RT}{zF} lna \quad , \quad (1.4)$$

where R is the universal gas constant, T is the absolute temperature, F is the Faraday constant, z is number of electrons for the exchange reactions, which is 2 for Cu

deposition, and *a* is the chemical activity, which equals the molar concentration of electron or acceptor ion in a dilute solutions. E_0 is the standard hydrogen potential, given the hydrogen chemical activity, a_{H+}= 1. For copper sulphate with a 0.1 mol/L concentration, we know the standard potential for Cu^{2+} → Cu is 0.337 V [7], thus:

$$E_{eq} = 0.337 + \frac{0.059}{2} \times \log(0.1) = 0.308\ V \tag{1.5}$$

When the electrodes are connected to an electric power source that provides excess charge, the equilibrium will be broken. The departure of the electrode potential from its equilibrium value is called the overpotential.

$$\eta = E - E_{eq} \tag{1.6}$$

1.1.2 Butler-Volmer equation

The Butler–Volmer equation is one of the most fundamental equations in electrochemistry describing the relationship between current density and electrode potential, considering that both a cathodic and an anodic reaction occur on the same electrode [6]:

$$I = A \cdot i_0 \cdot \left\{ \exp\left[\frac{(1-\alpha)nF}{RT}(E - E_{eq})\right] - \exp\left[-\frac{\alpha nF}{RT}(E - E_{eq})\right] \right\} \tag{1.7}$$

I is electrode current, i_0 is exchange current density, n is number of electrons involved in the electrode reaction, A is electrode active surface area, and α is charge transfer coefficient. The Butler-Volmer equation developed in the 1960's is based on pure metal electrodes. The process becomes more complicated when you have both metal and semiconductor electrodes in the electrodeposition system explained further in the next section.

1.2 Electrode/electrolyte interface

The electrode/electrolyte interface is very important for electrodeposition. Under equilibrium conditions, the interface region is electrically neutral; the time-averaged forces for every electrolyte ion are the same. The rate of deposition of Cu is the same as the rate of dissolution. When the substrate is biased negatively from equilibrium, current flows and the consequences to the interface charge varies for different electrodes, and depends on whether it is a metal, semiconductor or insulator.

1.2.1 Metal/electrolyte interfaces

Three different models in history have been proposed to describe the interfacial layer [6]. The first one is a parallel-plate capacitor model by Helmholtz and Perrin[6], which treats the electrified interfaces as two sheets of charge with same magnitude and opposite sign. Hence we have the term "double layer". Then Gouy-Chapman proposed a diffuse–charge model, which freed the ions from the sheet and introduced a diffuse region where the movement of ions is affected by electric forces and thermal jostling [6]. The Stern model combined the above two, suggesting an inner Helmholtz layer and an outer diffusion layer [6]. The combination of these three is the most commonly used within certain limitations. Fundamental questions remain to be solved for a better understanding of the electrified double-layer region. But generally we can treat the interface as shown in Fig.1.2.

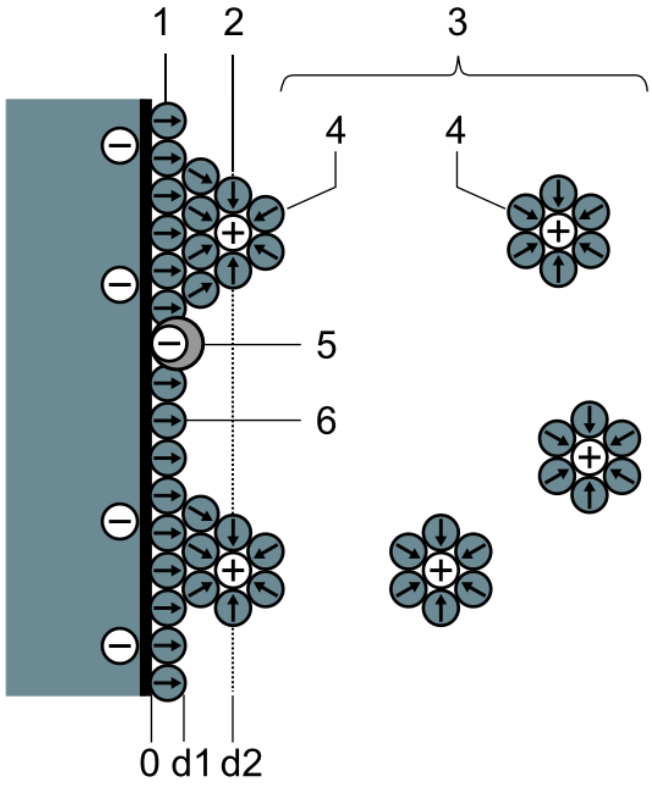

Figure 1.2: Schematic diagram of a doublelayer on an electrode: 1. Inner Helmholtz layer, largely occupied by water dipoles and a very few unsolvated negative ions, which can be considered as a hydration sheath of the electrode. 2. Outer Helmholtz layer, largely distributed solvated positive ions. 3. Electrolyte diffusion layer. 4. Solvated ions. 5. Adsorbed foreign ion. 6. Water molecules [8].

The Helmholtz layer (inner and outer) is 1.5 to 2.0 times the thickness of a mono-molecular water layer, smaller than 1 nm. Similar to the diffusion layer in the electrolyte, interfacial excess charge on the metal electrode is distributed from the solid face towards the interior forming a diffuse layer of excess electrons. This diffusive layer is called the "surface charge layer". The thickness of the diffusion and space charge layers depend on the concentration of mobile charge carriers, characterized by the Debye length, L_d.

$$\frac{1}{L_d} = \sqrt{\frac{e^2 n}{\varepsilon k T}} \tag{1.8}$$

where n is the concentration of charge carriers, e is the elementary charge on an electron, k is Boltzman's constant, T is temperature, and ε is the permittivity. For metal electrodes, with large electron densities (10^{22} cm^{-3}), the space charge layer thickness is small, less than the thickness of one monatomic layer. So the potential drop across the Helmholtz layer is large, thus creating a very strong interfacial electric field (10^9 Vm^{-1}), which extends perhaps only 0.5 nm into the electrolyte [6].

1.2.2 Semiconductor/electrolyte interfaces

Compared to metals, semiconductors have a much lower charge carrier density. The semiconductor space charge layer is in the range 100 nm – 1 μm for low-doped semiconductors (10^{14} ~10^{15} cm^{-3}) and drops to 10 nm – 100 nm for heavily-doped semiconductors. Since the carrier concentration is lower the Debye length is longer and hence a semiconductor surface is a more difficult surface for a metal nuclei to form compared to Au. The thickness of the electrolyte diffusion layer is in the range of 10 to 100 nm in aqueous ionic solutions of low ionic concentration (specify what is low in brackets) comparable to the thickness of the depletion layer in a heavily-doped semiconductor[9]. So for intrinsic semiconductors (< 10^{14} cm^{-3}), we can treat the semiconductor/electrolyte interface like the reverse of a metal/electrolyte interface. As shown in Fig 1.3, the voltage drop occurs primarily inside the semiconductor, and very little on the electrolyte side.

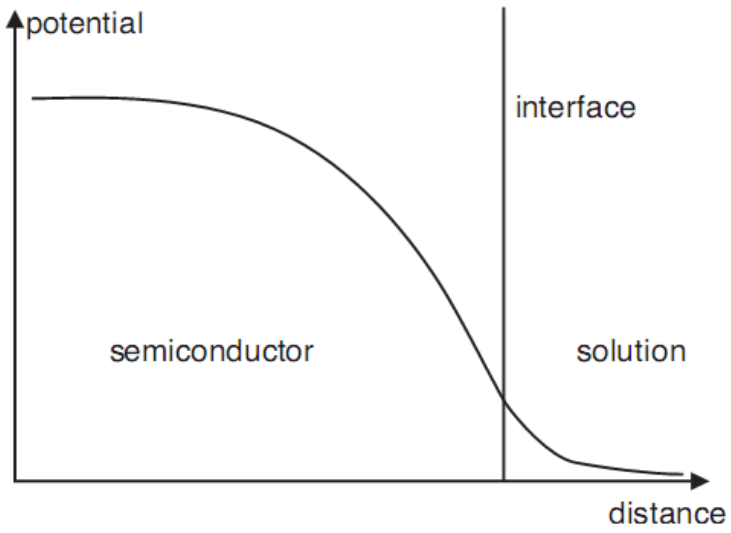

Figure 1.3: Potential drop at the semiconductor-electrolyte interface (schematic) [9].

1.3 Previous work on electrodeposited epitaxial metal on GaAs

Previous work by Dr. Zhiliang Bao showed that epitaxial Cu can be electrodeposited onto single crystalline GaAs substrate. The optimal growth condition determined was 53 °C with a current density 0.1 mA/mm^2 from pure $CuSO_4$ (0.1 M) [10]. Figure 1.4 shows an x-ray diffraction θ-2θ scan of Cu/GaAs (001) and a SEM image of the sample surface. We can see that the Cu film surface shows well-aligned pyramidal shapes.

Dr. Bao also summarised three key process parameters that are essential to achieve epitaxial Fe deposition on GaAs substrate. One is the addition of ammonium sulphate to the electrolyte: optimum epitaxy occurs for $(NH4)_2SO_4/FeSO_4$ ratios of 1:3. The second is setting the deposition current density to 0.1 mA/mm^2. The third is using ammonium hydroxide to etch the GaAs native oxide before electrodeposition [11].

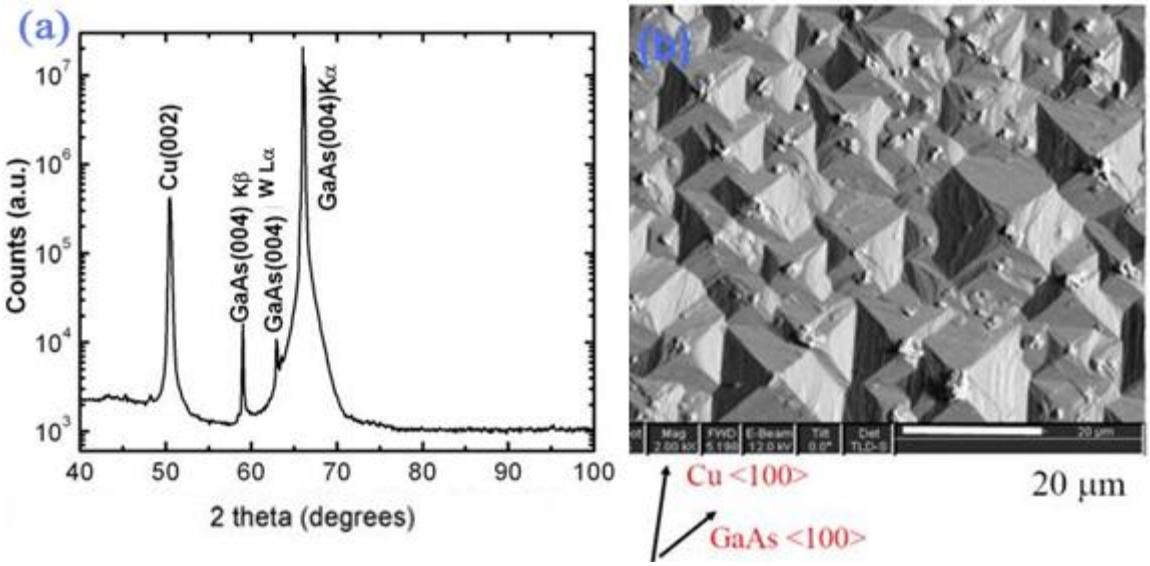

Figure 1.4: (a) XRD θ-2θ scans of Cu/GaAs deposited at 53°C onto (001) oriented substrate and (b) SEM image of the sample surface [10].

1.4 Electrodeposition setup

Figure 1.5 shows photographs of the electrodeposition system. It consisted of a glass beaker (Kimax 20 ml) on a support stand with anode and cathode suspended, and a computer-controlled power supply (Keithley 2400). The power supply provided a constant current from 10 pA to 1 A within a voltage compliance range ±100 V. A labview program was used to control the current output and record the voltage and current data. We used platinum wire as the anode. Ohmic contact between the GaAs substrate and the experimental apparatus was made via InGa liquid alloy on the backside of the sample (not the nanowire side). The nanowire side faced the platinum wire inside the cell. Stainless steel tweezers (Almedic #3 Switzerland) with a sharp and tight tip were

used to hold the sample. Photoresist, as an inert insulator, was used to define the

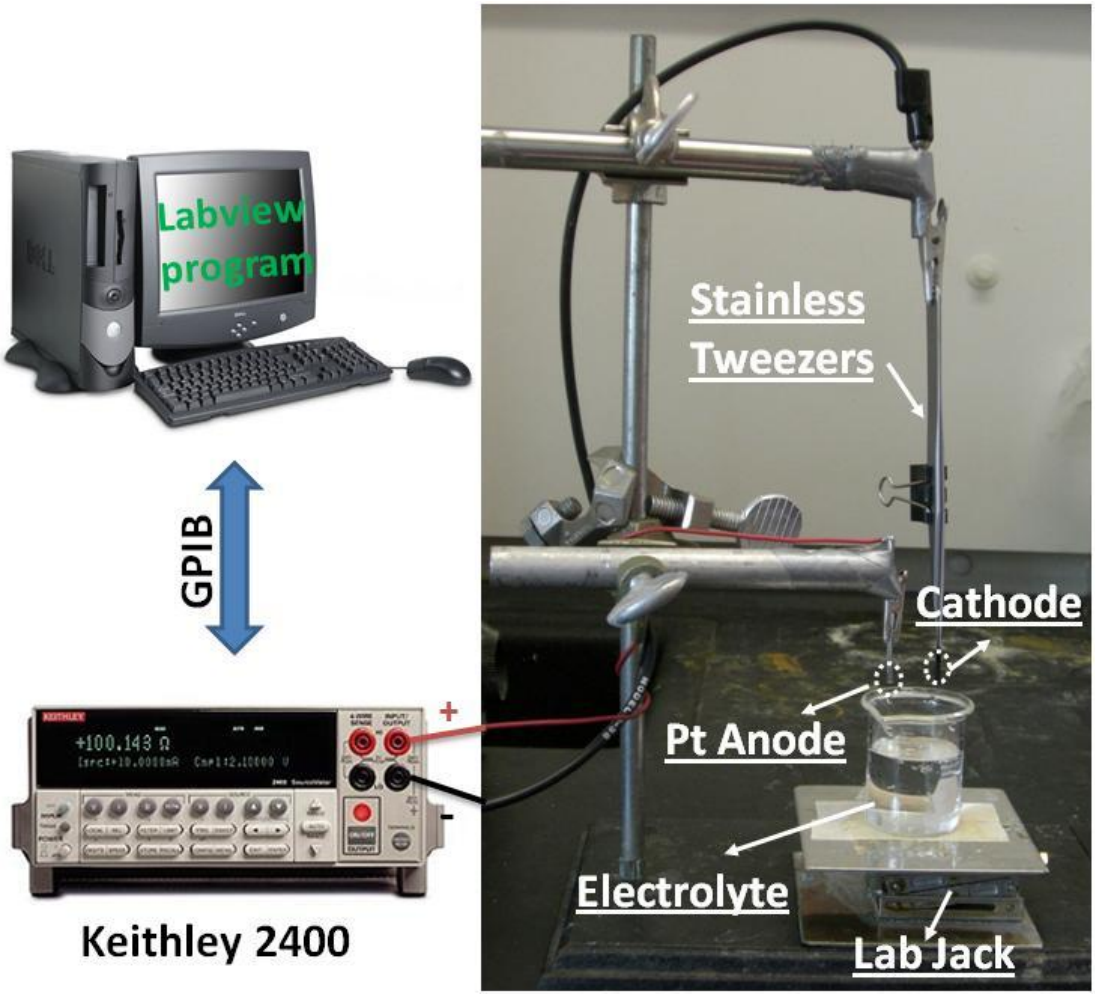

Figure 1.5: Schematic diagram of the circuit with a photo of the deposition cell.

growth window for the sample. As shown in Figure 1.6, photoresist was painted on the backside as well as on the edges of the GaAs NW sample.

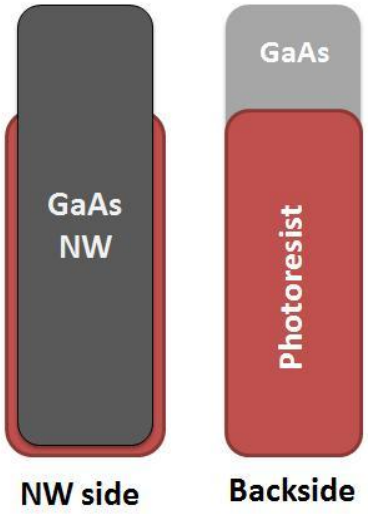

Figure 1.6: Schematic diagram of a sample prepared with photoresist masking. The red areas represent photoresist. The sample side with NWs appears darker compared to a polished GaAs substrate.

1.5 Experimental parameters: current density and initial voltage

For all samples, two different initial open circuit voltages: 50 V or 100 V were applied. We found no differences in the experimental results. The average area of the NWs versus the whole substrate was 40%. Therefore, we used 40% of the optimum value 0.1 mA/mm^2 indicated from Dr. Bao's work, giving 0.04 mA /mm^2 as the current density. When a larger current density, 0.1 mA/mm^2, was applied to certain samples the results showed no significant difference from those runs at 0.04 mA/mm^2.

1.6 Experimental procedures

Cleaning of the glass beakers and samples is very important to avoid any possible contamination of the sample and electrolyte. This is also vital for the epitaxial metal growth. Glassware and the platinum electrode were cleaned using an ultra-sonicating bath

in isopropanol then doubly-deionized water (DDI), each for 5 minutes. This process removes any micro-dust or other particulate matter that may interfere with the metal deposition.

Samples were prepared by cleaving the as-received GaAs NW sample into 15-30 mm^2 pieces. The backside and the edges of the sample piece were then coated with photoresist. After sufficient drying of the photoresist paint at room temperature (10 hours), the deposition area was measured for calculation of current.

The oxide etching solution consisted of ammonium hydroxide (10%) made by diluting 28% ammonium hydroxide with doubly deionized (DDI) water. The electrolytes consisted of 0.1 M $CuSO_4$ using DDI water for Cu or 0.1 M $FeSO_4$ with 0.3 M $(NH_4)_2SO_4$ for Fe.

Ohmic contact was made to the substrate backside; the area was first etched with 10% ammonium hydroxide and then dried. A large area of InGa was scratched onto the surface and stainless tweezers were securely attached to the substrate.

The dried platinum wire and tweezers with sample attached were assembled onto the experiment stand. The sample was first etched for 10 seconds in 10% ammonium hydroxide to remove the native oxide then immersed in DDI water for another 10 seconds. The power supply was turned on and then the sample under open-circuit voltage was immersed in the electrolyte for metal deposition. The deposition time (20 – 60 s) was controlled by a labview program; the power was turned off when the deposition process reached the preset time.

After deposition, the sample was rinsed in acetone to remove the photoresist and then cleaned with isopropanol and deionized water. The InGa contact could be removed

by ammonium hydroxide using a cotton swab. The beakers and platinum wire were immersed in concentrated sulphuric acid and then rinsed by deionized water. The beakers and platinum wire were stored when not in use immersed in 2-propanol inside a sealed large beaker, to prevent contamination.

After our sample was totally dried, the deposited structure was studied using scanning electron microscopy (FEI Strata Dual Beam 235 Scanning Electron Microscope) (SEM) operating at 5 keV. The NWs were mechanically transferred to a carbon-coated grid for TEM analysis using a FEI Tecnai 20 field emission Scanning Transmission Electron Microscope (STEM) operating at 200 keV.

2: NANOWIRE SAMPLES

2.1 NW samples

GaAs and InAs NWs from Dr. Simon Watkins' group (Simon Fraser University) and InAs NWs from Dr. Philip Poole (Institute for Microstructural Sciences, NRC Canada) were used for the deposition experiments. All wires were (111) oriented and grown on (111)B oriented single crystalline substrates. Table 2.1 lists the details of the NW samples used for this work. GaAs nanowires were grown epitaxially on *n*-type Si-doped GaAs substrates by gold-catalyzed vapour liquid solid (VLS) growth in a metalorganic vapour phase epitaxy (MOVPE) reactor. To control conductivity, growth with a carbon dopant source were investigated. The carbon concentration was controlled with the addition of carbon tetrabromide gas (CBr_4) during growth. The As precursor was tertiarybutylarsine (TBAs) while there were two different types of Ga precursors, Type A: triethylgallium (TEGa) and Type B: trimethylgallium (TMGa) [12][13].

Unintentional carbon doping of GaAs NWs can occur via the Ga precursor used in the MOCVD growth as a function of temperature, as well as from intentional carbon doping when CBr_4 was added. Nevertheless, for convenience, "doped or undoped NWs" refers to GaAs NWs grown using either TEGa or TMGa with TBAs precursors and with or without CBr_4, respectively. "Core-shell NWs" refers to wires grown with an undoped GaAs core, followed by a doped GaAs shell.

InAs NWs obtained from Dr. Watkin's group were grown at a temperature of 440 °C using trimethylindium (TMIn) as the group III precursor and TBAs as the group V

precursor. The NWs were unintentionally doped and the substrate was *n*-type GaAs doped with Si (~ $5x10^{17}/cm^3$).

InAs NWs from NRC were grown epitaxially on *n*-type InP substrates without gold catalyst. These wires were grown from small patterned openings (~160 nm) in a 20 nm thick S_iO_2 layer that covered the entire top surface of the InP wafer.

Table 2.1: Summary of NW samples deposited in this work.

NW	MOCVD Run No.	Ga or In Precursor	Doping	Metal Deposited	Time (s)	Location	Section
GaAs	5849	TEGa	CBr_4	Cu	40	Au	3.2.1
	5902		undoped	Cu	40	Au	3.1.1
	5906 coreshell		2/3 CBr_4 1/3undoped	Fe	30	Au	3.3
	6027	TMGa	CBr_4	Cu	30	Au	3.2.2
	6026		undoped	Cu	30	Au	3.1.2
	6059	Core TMGa Shell TEGa	undoped CBr_4	Cu	40	Au and sidewall	3.2.3
InAs	6060	TMIn	undoped	Cu	40	Au and sidewall	3.4.2
	NRC	TMIn	undoped	Cu, Fe	30	Top and sidewall	3.4.1

2.2 Wettability of sample surfaces

We investigated the effects of sample preparation on water repellancy as measured by the contact angle of liquid drops on each surface. Although the NW substrates are totally immersed in the electrolyte during the deposition this does not necessarily mean that the entire NW was in contact with the electrolyte.

Young's Equation describes the contact angle Θ_c of a liquid droplet on a flat, solid surface as a function of interfacial surface tensions (Figure 2.1):

$$\cos \Theta_c = (\gamma_{SV} - \gamma_{SL})/\gamma_{LV} \quad , \qquad (2.1)$$

where γ_{SV}, γ_{SL}, and γ_{LV} are the solid-vapour, solid-liquid, and liquid-vapour interfacial surface tensions, respectively, in units of force per unit length. A lower γ_{LV} or γ_{SL} will cause a smaller contact angle. Sample surfaces were examined using a contact angle instrument consisting of an optical microscope and built-in software for angle measurement (VCA Optima located in Dr. Hogan Yu's Lab in 4D Labs) [14].

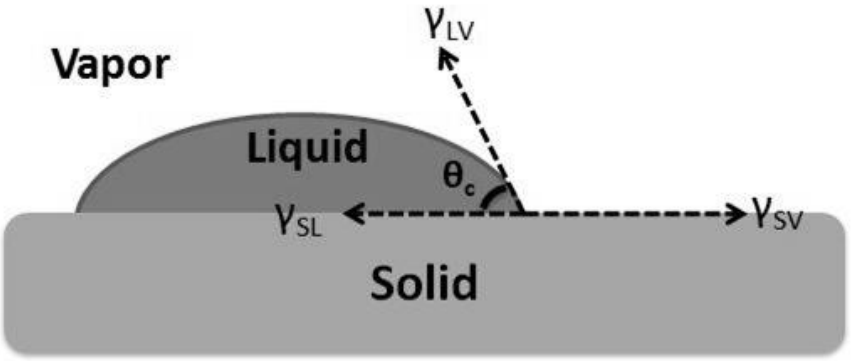

Figure 2.1: Illustration of the contact angle, θ_c, of a liquid droplet on a substrate as a function of the interfacial surface tensions, γ solid liquid (SV), solid vapour (SV) and liquid vapour (LV).

2.2.1 As-received sample surfaces

Figure 2.2 shows different as-received sample surfaces under SEM and the corresponding de-ionized water droplet on the surface under an optical microscope. The measurement of contact angle was obtained from the optical images of the liquid drop interfaces for each sample surface. The red lines on each image are tangents to the drop and substrate surfaces at their intersection.

The pure as-received GaAs (111) *B* substrates were hydrophobic, with a contact angle ranging from 65° to 70°. The evaporation of Au nanoparticles onto these GaAs substrates made the surface more hydrophobic, with larger contact angles ranging from 85° to 100°. Even larger contact angles, greater than 150°, were found for some of the NW samples, e.g. (c) and (d) while others (e) and (f) had contact angles of zero becoming hydrophilic.

The wetting properties of GaAs NWs have been reported to be a function of surface geometry, the length of the NWs [15], the wire density and the morphology of NWs [16]. It is found that hydrophobic behavior becomes more pronounced as the length of the nanowires increases [15]. Figure 2.3 shows a series of contact angle measurements taken for different as-received GaAs NW samples as a function of NW diameter, length, and density and the gold thickness. Consistent with the literature reports, nanowire diameters greater than 200 nm, or lengths greater than 2 μm, or density less than 15 μm^{-2}, about half of the samples are hydrophobic with average contact angles of 140°. The NWs with higher densities are mostly those that also had smaller diameters. These results indicate that surface preparation to enhance wetting is required.

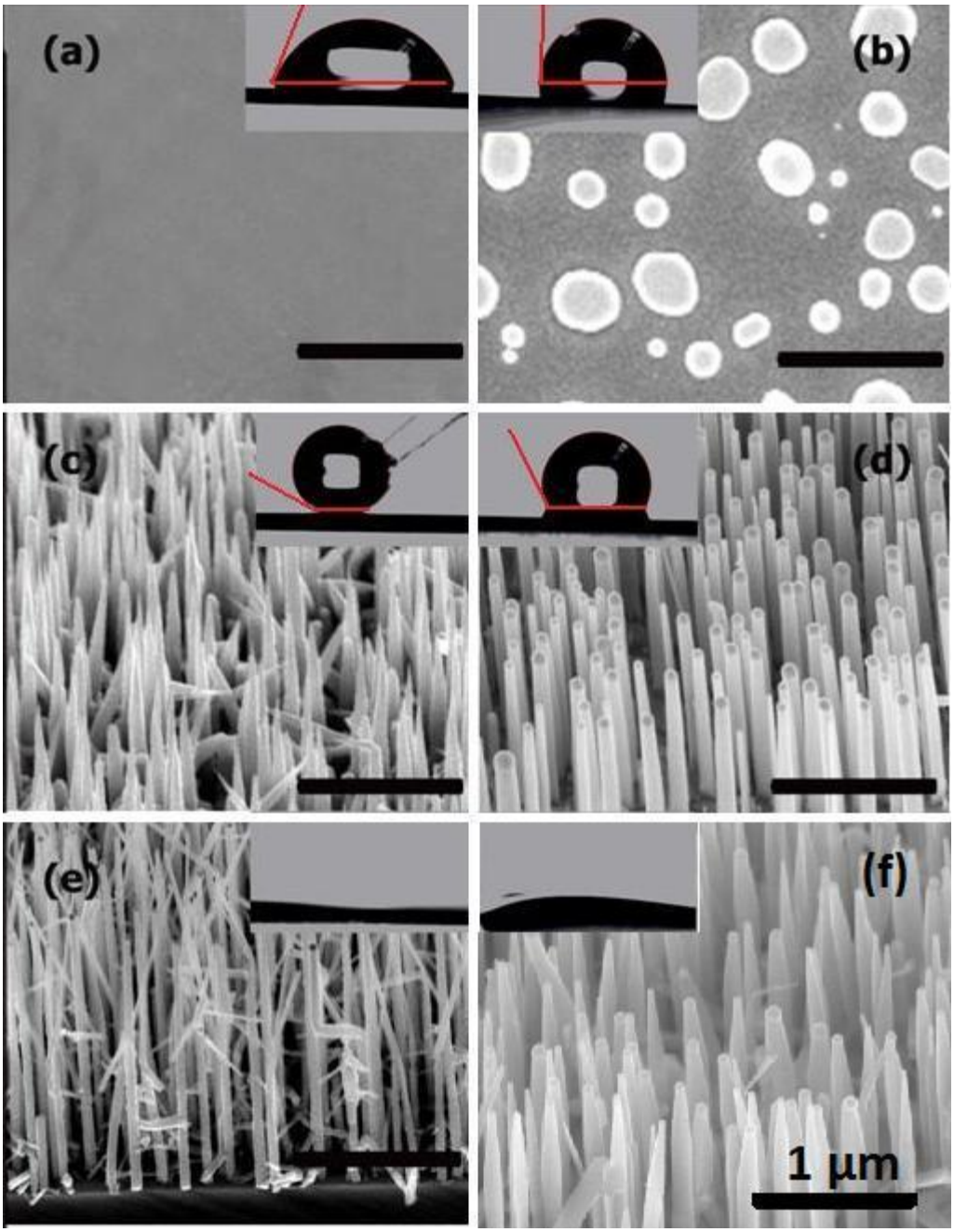

Figure 2.2: Tilted-view SEM images of different as-received sample surfaces and the corresponding optical photograph of a deionized-water droplet on the surface: (a) GaAs (111) *B* substrate. (b) same GaAs substrate but with Au nanoparticles evaporated and annealed in preparation for nanowire growth. (c) - (f): GaAs NWs grown from gold thicknesses of 2 nm, 2 nm, 0.5 nm and 1.5 nm. The added red lines are tangents to the drop surface and substrate at their intersection. The resulting angle is the contact angle.

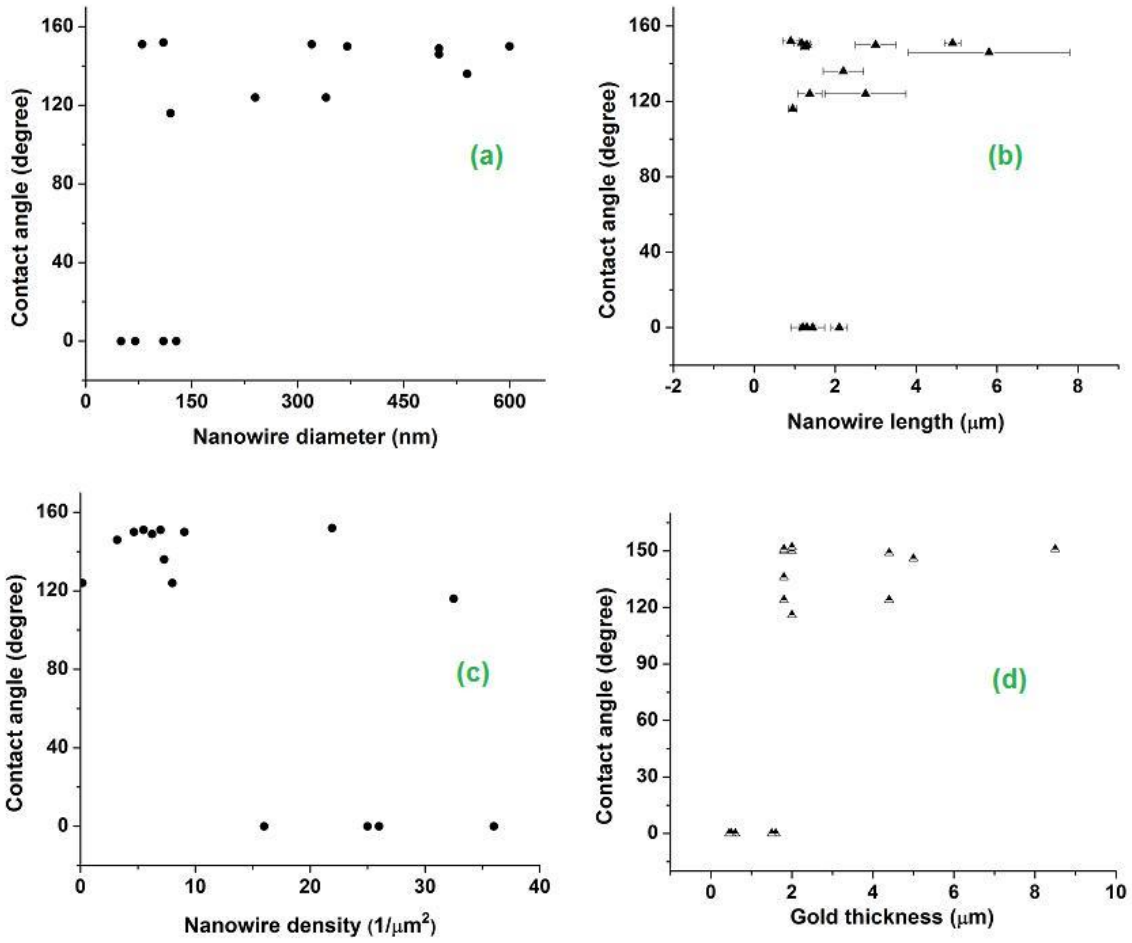

Figure 2.3. Plots of contact angle versus NW (a) diameter, (b) length, and (c) density and (d) gold film thickness (before annealing to form gold nanoparticles for MOCVD NW growth).

2.2.2 GaAs NW surfaces after ammonium hydroxide etching

It has been reported that alkaline treated GaAs bulk surfaces are hydrophilic [17], attributed to the OH groups left on the GaAs surfaces. Our GaAs substrates and NW samples when etched in $(NH_4)OH$, also became hydrophilic with the solution completely wetting the surface like those in Figure 2.2 (e) or (f). All samples also became hydrophilic after immersion in ethanol, consistent with its lower surface tension

compared to water [18]. Table 2.2 compares surface tensions for air interfaces with water, ethanol and ammonium hydroxide (9.6%). Ethanol has a much lower surface tension compared to water, or ammonium hydroxide. Experiments with dipping the nanowires in ethanol followed by rinsing in water prior to electrodeposition showed that ethanol treated GaAs NW surfaces also became hydrophilic.

Interface with air	γ (mN·m^{-1})
Water	72.86
Ethanol	22.39
Ammonium Hydroxide (9.6%)	67.85

Table 2.2 The liquid-vapour interfacial surface tension for water-air, ethanol-air and 9.6% Aqueous ammonia (ammonium hydroxide) – air interfaces at room temperature. [19]

2.3 Removal of gold

To check the effect of the Au catalyst on NW electrodeposition a method to remove the gold before deposition was needed. There are two commonly used wet etching solutions that dissolve gold [20] including (1) mixtures of nitric acid (HNO_3) and hydrochloric acid (HCl) (ratio 1: 3) and (2) fresh aqueous solution of I_2 and KI (aqueous tri-iodide) (KI : I_2 : H_2O = 4 g : 1 g : 40 ml). Fresh solutions are necessary since the iodine oxidizes easily in water. It is known that nitric acid will damage a GaAs surface [21], therefore, we chose to use aqueous tri-iodide to remove the Au catalysts. Figure 2.4 (b) shows SEM images of GaAs substrates with gold nanoparticles only and nanowires

with Au catalysts after etching in tri-iodide. In both cases the Au particles are gone but there is obvious damage to the nanowires. Similar damage was reported for Ge NWs when etched in KI/I_2. [22] They reduced this problem by adding HCl to the etching solution, which protected the Ge NWs likely by a chlorine-based surface passivation. Based on this work we carried out a second set of Au etching experiments adding HCl to the tri-iodide etching solution (2 mL 35% HCl in 15 mL tri-iodide). Figure 2.4 (b left) shows an SEM image of the same Au nanoparticle GaAs sample as in (a left) but after such etching. We can see that there are round-shaped depressions left on the substrate, which likely indicate the original location of gold nanoparticles that had reacted with the substrate, or that the etch has caused new damage to the GaAs substrate. Similarly, Figure 2.4 (c right) shows an SEM image of GaAs NWs that shows clearly that the gold catalysts were removed with minimal damage to the GaAs NWs. (The size of the Au nanoparticles on GaAs in this case were larger than those used to grow the NW samples shown.)

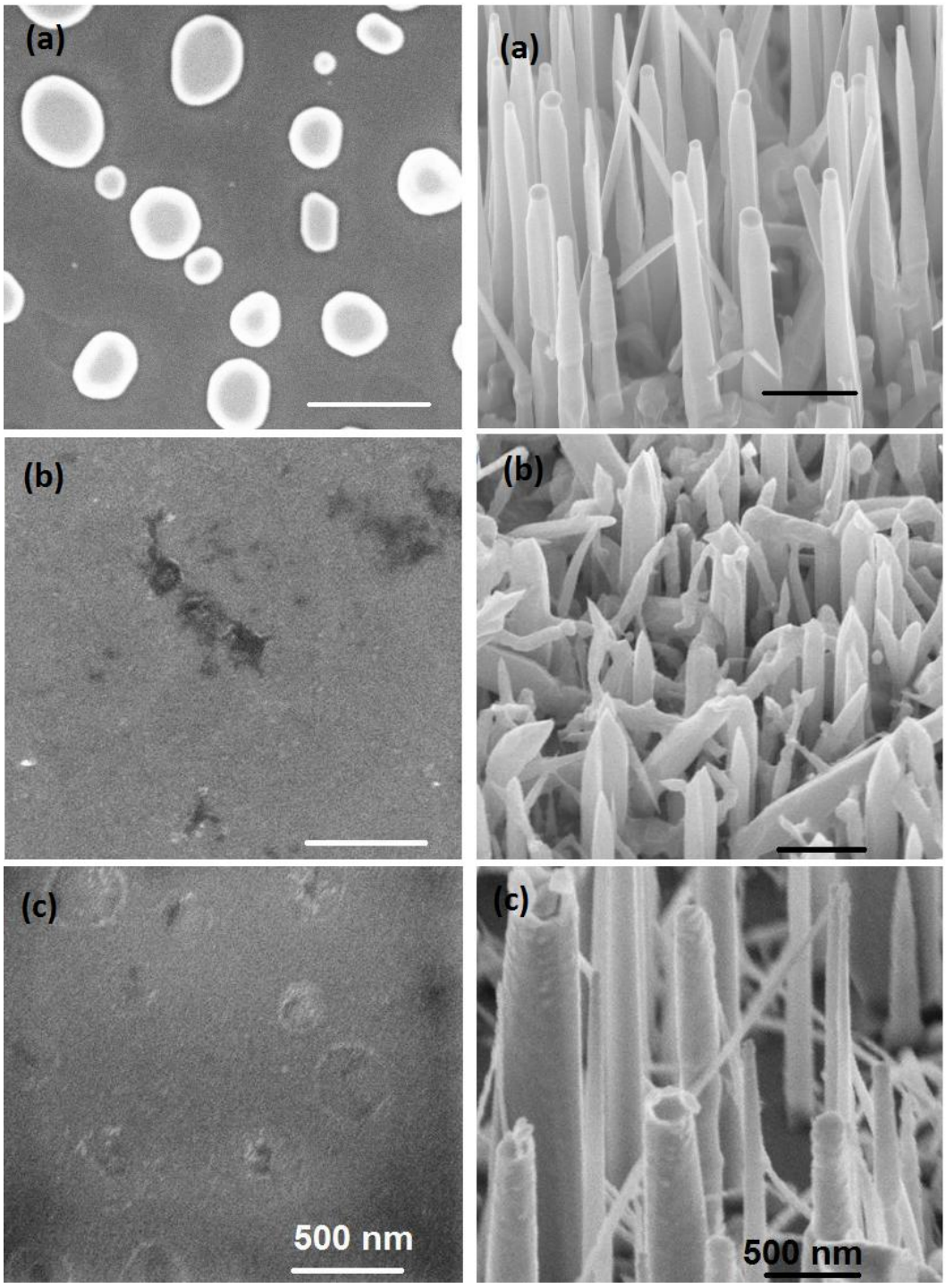

Figure 2.4: SEM images left side: gold nanoparticles on GaAs (111) sample, right side GaAs NWs: (a) as-deposited and (b) and (c) after gold etching in KI/I_2 solutions:(b) without HCl, and (c) with HCl.

2.4 Light-assisted electrodeposition

Photocurrent can be generated from GaAs NWs under visible or ultraviolet (UV) illumination [23]. Experimental results of photoconductivity measurements for GaN nanowires also indicate that the generated current from the NW increased considerably under UV illumination [24]. Light-assisted electrochemical deposition of metal films on Si or GaAs substrates has been reported years ago [25][26]. The deposition rate increases significantly for Au on *p*-Si under illumination (l00-W tungsten-halogen lamp) compared to in the dark [25]. Also, there is intensive study about photo-electrochemical deposition used to form patterned metal films [26]. Since our GaAs nanowires were potentially carbon-doped, meaning *p*-type, it was interesting to check if light during electrodeposition would have an effect on metal growth rates.

To investigate the effect of light exposure, electrodeposition experiments were performed on GaAs substrates as a function of illumination from an LED white light source. The band gap energy of intrinsic GaAs (1.42 eV at room temperature) is equivalent to the energy of a photon with a wavelength of 870 nm (infrared). Since we used a glass beaker (Kimax 20 mL No.14000) to hold the electrolyte and sample, it was important to measure the transmission spectra of the light source through glass to predict the intensity spectra that would expose our GaAs substrates.

Figure 2.5 shows transmission spectra measured using a spectrometer (spm-002 by Photon Control) with a spectral detection range from ultra violet (UV), (200 nm) to near-infrared (1700 nm). The source generated light with two major peaks at 440 nm and 550 nm with absorption losses of 50% through the glass. The UV light from a lamp (peak position 254 nm) was totally absorbed by the glass. For the electrodeposition experiment,

the LED flashlight was oriented to project parallel to the nanowires (perpendicular to the GaAs substrate surface). The light was turned on before ammonium etching and maintained throughout the subsequent deposition process.

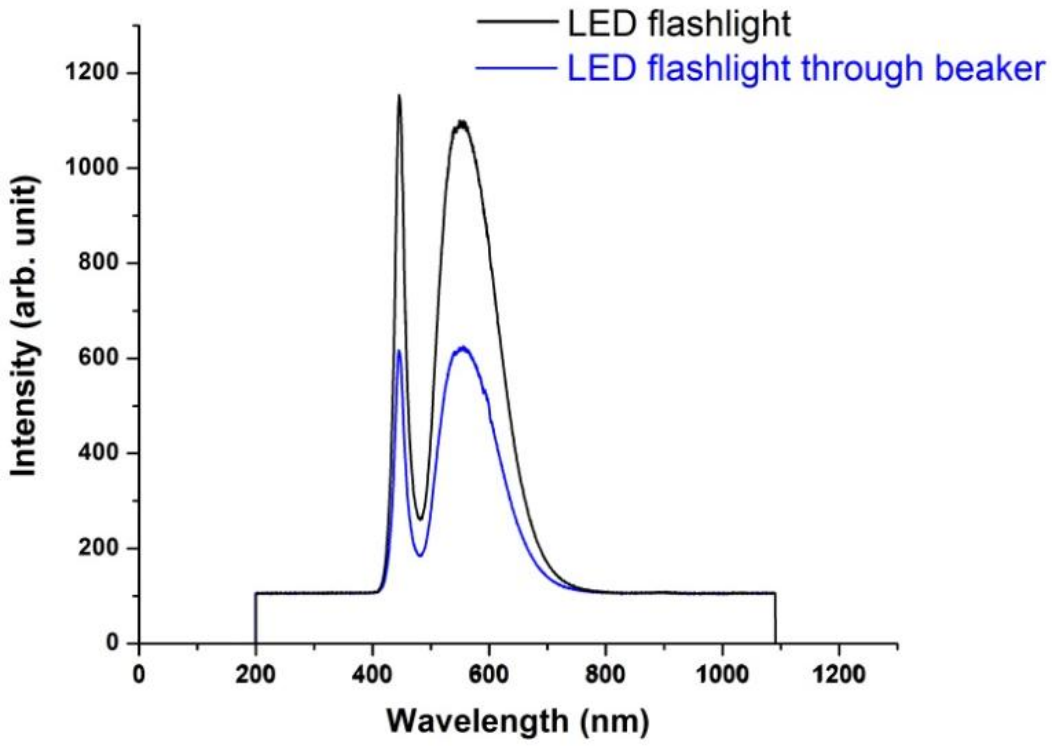

Figure 2.5: Transmission intensity for a LED flashlight measured in air and through a Kimax glass beaker.

2.5 Electrodeposition of metal on InAs NWs

Previous work in the literature on electrochemical deposition of metal on InAs NWs or InAs bulk samples was not found. Unpublished results by a former student, Jon Bratwold, found that electrodeposition of Fe on InAs (100) single crystalline substrates was feasible with ammonium hydroxide etching. Plan view TEM showed that such Fe films had a preferred growth orientation. Ammonium hydroxide (10 %) was reported to

be used for indium surface preparation prior to growing metal contacts on InAs bulk samples using electron-beam evaporation [27]. Thus, we used the same surface preparation that we used for GaAs NWs for the preparation of copper deposition on InAs NWs. We also chose to use similar electrodeposition parameters, i.e. electrolyte concentration: 0.1 mol/L $CuSO_4$, current density: 0. 1 mA/mm^2 and at room temperature.

3: RESULTS

This chapter is organized into six sections with SEM and TEM results from the electrodeposition of two metals (Fe, Cu) onto two different semiconductor NWs (InAs and GaAs).

3.1 Electrodeposition of Cu on GaAs NWs

3.1.1 Unintentionally-doped GaAs NWs - Type A Ga precursor (TEGa)

Figure 3.1 shows SEM images comparing Type A GaAs NWs before and after electrodeposition of Cu. After MOCVD growth, most of the NWs are vertically perpendicular to the substrate, in the (111)B direction. Gold nanoparticles can be seen at the tips of each NW. After electrodeposition, the Au seeds become coated with Cu. It appears that Cu deposits only at the top of the NW.

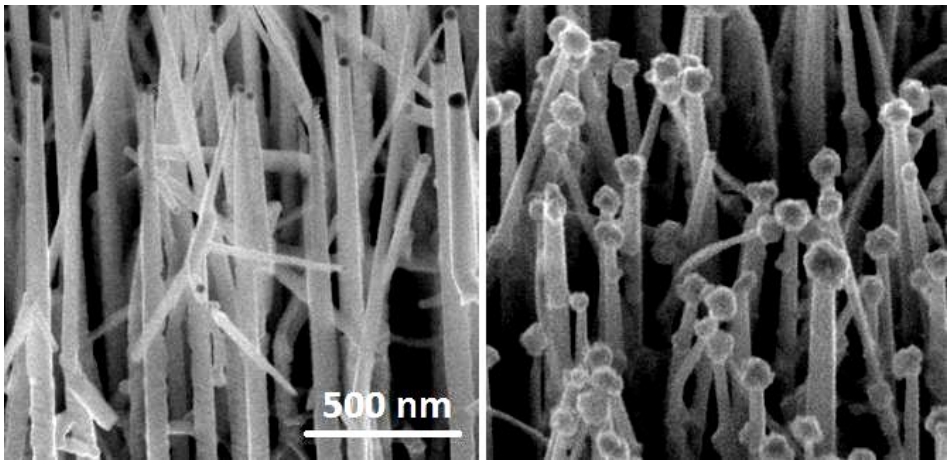

Figure 3.1: SEM images of undoped Type A GaAs NWs before (left) and after (right) electrodeposition of Cu for 40 s.

TEM images shown in Figure 3.2 of these wires give a higher magnification-view of their crystal structure. The first image is a low magnification image of the entire wire after removal from the substrate onto the grid. The image at the bottom right is the enlarged view of the top part of the NW. We can see that the Cu/Au particle looks darker due to its greater thickness compared to the GaAs. The large period fringes visible are most likely due to translational Moiré fringes from overlapping Au-Cu regions with different lattice constants. The spacing between the Moiré fringes (1.6 ± 0.3 nm), compares to the calculated spacing of translational Moiré fringes from Au-Cu (111) (1.81 nm) [28]. From the BF images (a) and (c) we can see that the Cu crystal has hexagonal facets, which indicates a single crystalline epitaxial material. The selected area diffraction pattern in (b) shows that the GaAs wire is (110) oriented in the plane of the image with a growth direction of [111] as expected. The Cu and Au diffraction spots are not clearly visible from this wire.

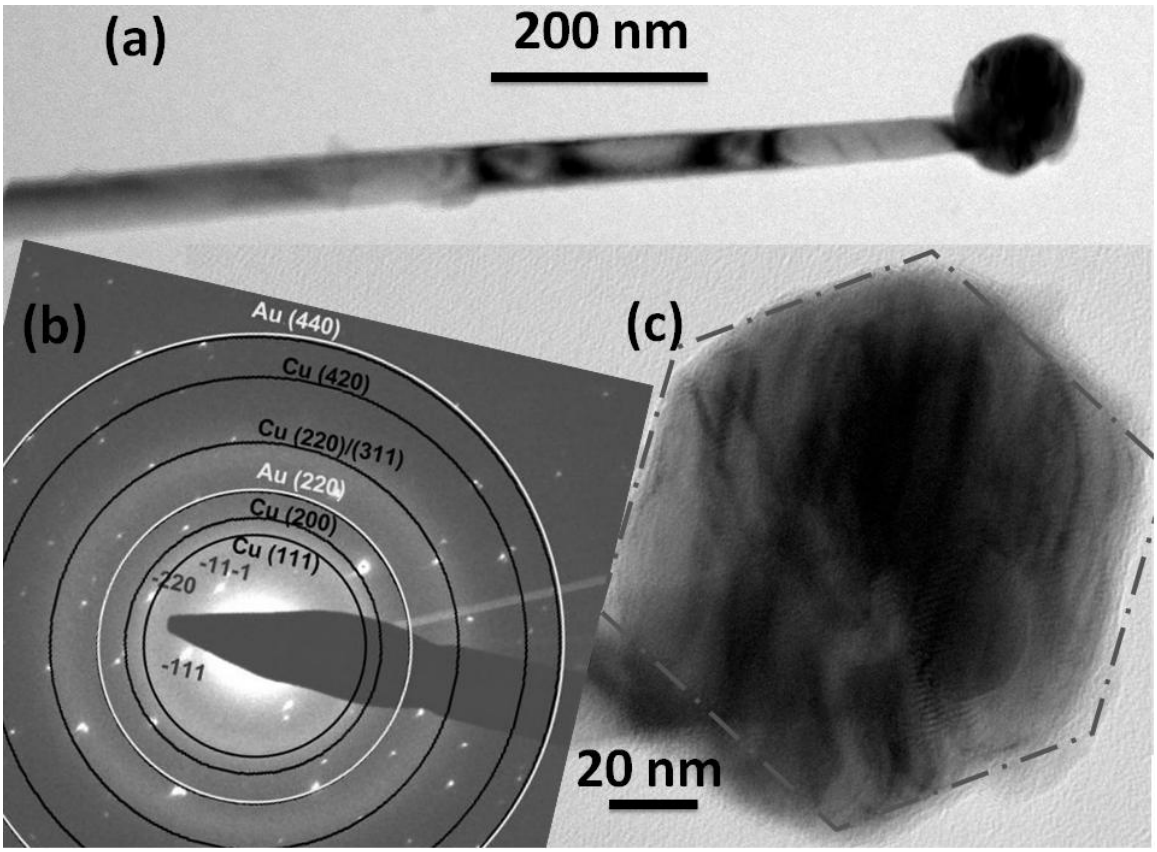

Figure 3.2: TEM bright field images of a undoped Type A GaAs NW: (a)(c), and the SAD pattern from the Au end region, (b) after electrodeposition of Cu for 40 s. Image (c) shows the enlarged version of the top part of the NW (a). In graph (b) the circled indexed points are diffraction spots from GaAs. The solid line circles are calculated diffraction rings for polycrystalline Au and the dashed line circles are calculated diffraction rings for polycrystalline Cu.

3.1.2 Unintentionally-doped GaAs NWs: Type B Ga precursor (TMGa)

The difference between NW growth using TMGa and TEGa precursors is fully discussed in references [12] [13]. Briefly, tapering has been found for Type A GaAs NWs (TEGa) while Type B (TMGa) NWs exhibit much higher axial growth rates, as well as a dramatic reduction in tapering. It was also found that growth with CBr_4 is associated with less

tapering for Type A GaAs NWs. Figure 3.3 shows Type A NWs grown with and without CBr_4. The geometry of Type B NWs is similar to (b1), regardless of whether CBr_4 is added.

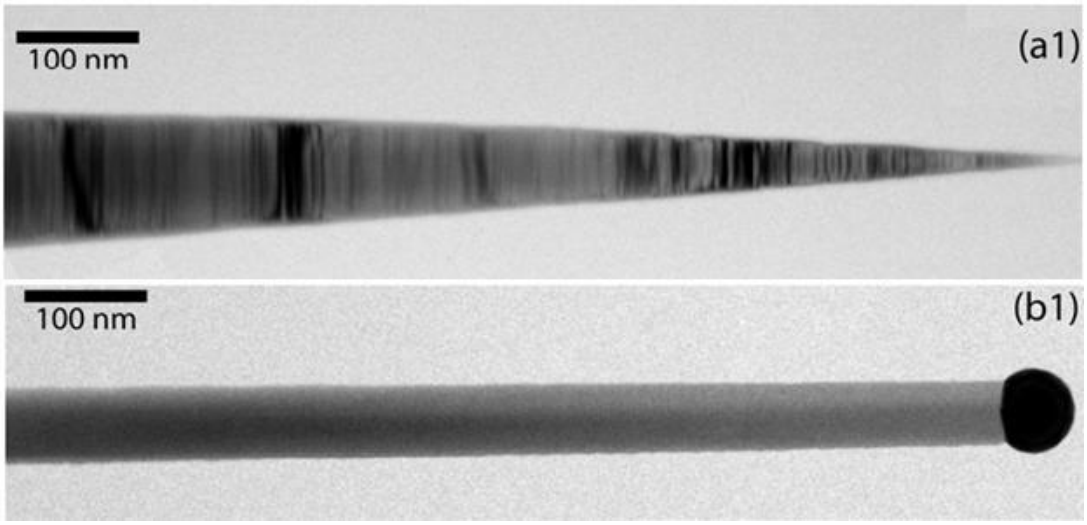

Figure 3.3: BF TEM images of Type A GaAs NWs grown without CBr_4 (a1) and with CBr_4 (b1), respectively. (a1) shows the extreme condition for tapering while in certain cases there is still a gold catalyst left on top of the NW [12].

Figure 3.4 shows SEM images of Type B GaAs NWs (a) before and (b) after Cu deposition for 30 sec. We can see in Fig. 3.4 (b) that the previously vertically-aligned nanowires have bent together to form clusters. This is due to a known capillary effect during preparation before electrodeposition[29]. Others have shown that it can be eliminated by introducing an electric field during drying[30]. We tried to dry the sample with 100 V for 5 minutes directly after electrodeposition. It did not stop our coalescence. More details need to be analyzed, such as the distance between the sample surface and counter electrode. For these experiments this distance is only 1 mm while it was ~ 2 cm

in our case. The diameters of these NWs ranged from 60 to 120 nm, averaging 70 nm. Combining a top view with tilted images, the Cu crystals are distinguished from the substrate surface or nanowires as isolated faceted particles are found around the bottom of the NWs, as well as at the top. The diameter of the Cu on top of the NWs is not uniform, which is possibly due to the cluster structure.

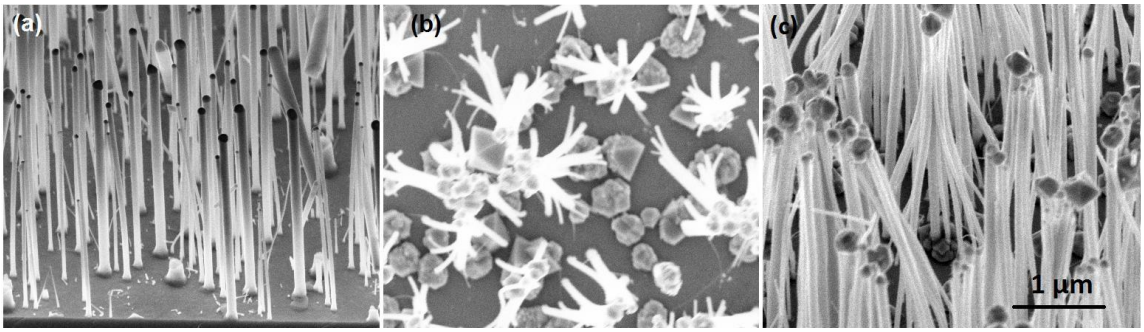

Figure 3.4: SEM images of type B GaAs NWs before (a) and after (b, c) Cu electrodeposition for 30 s. (b) is a top view while (a) and (c) are tilted images (45°). The arrows point to examples of Cu crystals.

3.2 GaAs NWs intentionally doped with carbon

Three different kinds of GaAs NWs intentionally doped with carbon using CBr_4 were examined for deposition. The first two varied the type of Ga precursor, Type A or Type B. The third samples were core-shell with a Type A core and a Type B shell. The effects of these growth conditions on the effectiveness of carbon doping was unknown. The intention was to investigate variations in the conductivity in the NWs by monitoring the rate of metal electrodeposition.

3.2.1 Type A TEGa precursor

Figure 3.5 shows SEM images of intentionally carbon-doped Type A GaAs NWs before and after Cu electrodeposition. Cu is predominantly found on the top of the NWs or as isolated large crystals on the substrate. As seen in the TEM images of Figure 3.6 (c), these GaAs NW grew along the (111) direction and thickness fringes appear around the NW centre and edge. The diffraction pattern indicates that the electron beam was perpendicular to a GaAs (112) plane, with the Cu (111) planes almost parallel to the the GaAs (111) planes. Gold (111) also aligns with the GaAs (111) planes, in an epitaxial arrangement [31].

Dark field TEM images of one of these wires are shown in Figure 3.6 (b). They indicate that the Cu at the top of GaAs is a single crystal of orientation [112] the same as the GaAs crystal and Au. Figure 3.7 shows TEM bright field and dark field images of another GaAs NW with the same orientation. We can see that the Cu crystal is a perfect hexagonal shape, surrounding the Au catalyst (the darker part) inside. The dark field image confirms that we have single crystalline copper growing on top of single crystalline GaAs.

Figure 3.8 illustrates the increase of the Cu crystal volume on top of two different intentionally carbon-doped Type A GaAs NW with double the deposition time, (from 40 s to 80 s) under otherwise similar experimental conditions. Longer deposition times gave larger Cu particles.

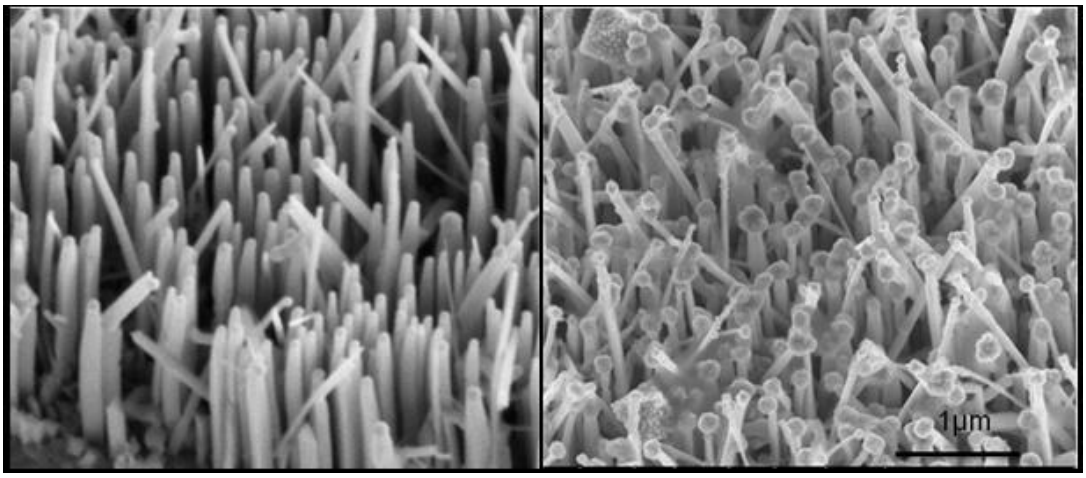

Figure 3.5: SEM images of Type A intentionally carbon-doped GaAs NWs before (left) and after (right) electrodeposition of Cu for 40 s.

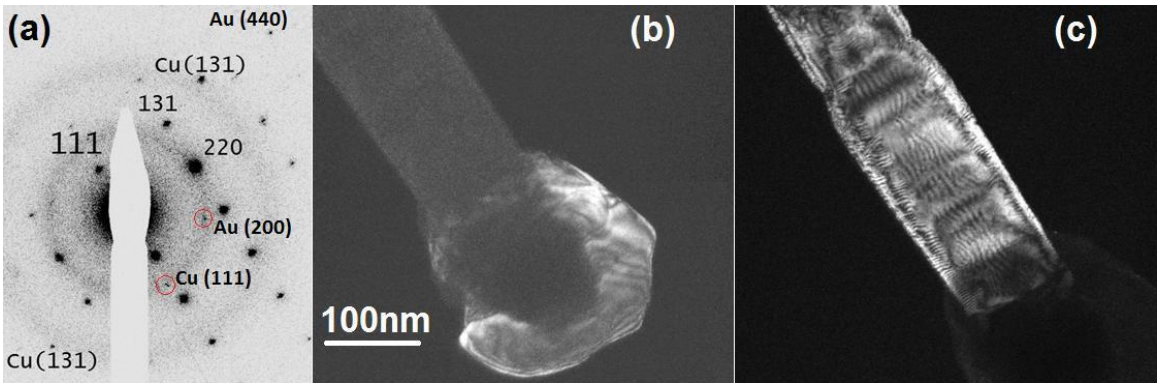

Figure 3.6: TEM images of Type A intentionally carbon-doped GaAs NWs after deposition of Cu. Image (a) is the SAD pattern showing a (112) zincblende orientation. The indexed spots are GaAs with other Cu and Au spots indicated. Dark field images (b) and (c) were obtained using a Cu (131) and a GaAs (220) diffraction spot, respectively.

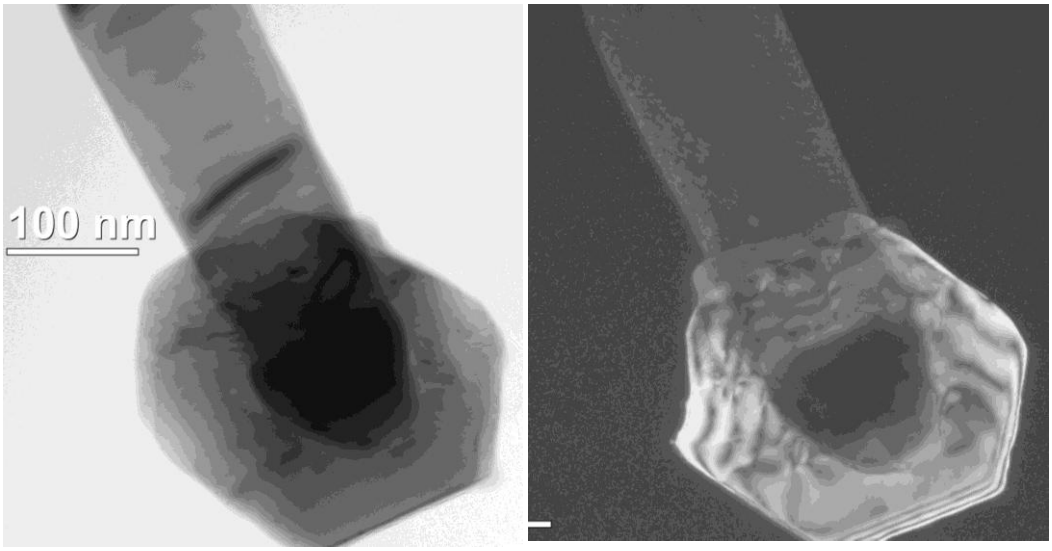

Figure 3.7: TEM bright field image (left) of one GaAs NW and its dark field image (right) from a Cu diffraction spot. The fringes are due to thickness variations. There are also dislocations visible within the Cu.

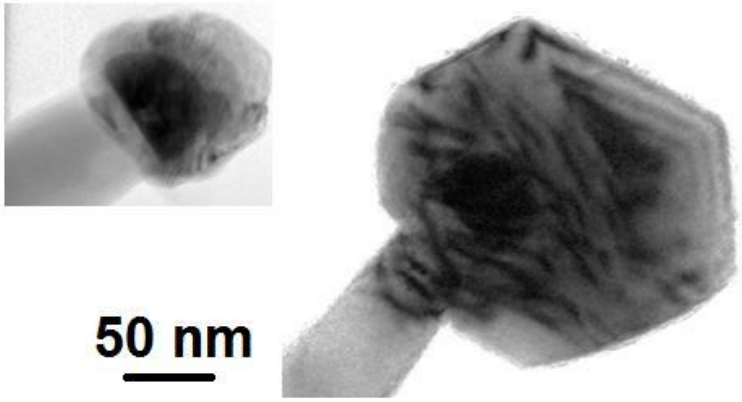

Figure 3.8: TEM bright field images of intentionally carbon-doped GaAs NWs after electrodeposition of Cu for 40 s (left) and 80 s (right). The two NWs have similar diameters and the deposition experimental parameters are the same. The dark fringes are interference from thickness variations.

3.2.1.B Nanowire diameter and geometry

Due to the distribution of diameters of the Type A GaAs NWs, we are able to analyse the relationship between NW diameter and the volume of deposited Cu. Figure 3.9 shows the experimental results for one GaAs sample with NW diameters ranging from 50 nm to 140 nm. Calculation of the Cu volume is based on the assumption that the Cu nanoparticle is a sphere. Some data points have larger error bars because the Cu crystals actually are facetted with different radii at different orientations. We corrected the Cu volume by deducting the volume of the inside gold hemisphere and GaAs core. The linear fit intersects the x-axis at 50 nm, suggesting that there may not have been copper growing on GaAs NWs with diameters less than 50 nm.

We also found Cu nanoparticles growing around the nanowire shaft as well as at the top for larger diameter (~ 1 μm) NWs. Figure 3.10 shows SEM images from Type A C-doped GaAs NWs. The gold nanoparticle size is not uniform, with diameter varying from 50 nm to 1 μm. We can see that polycrystalline Cu nanoparticles have grown around the large diameter nanowires while the others with smaller diameter only have Cu at the top.

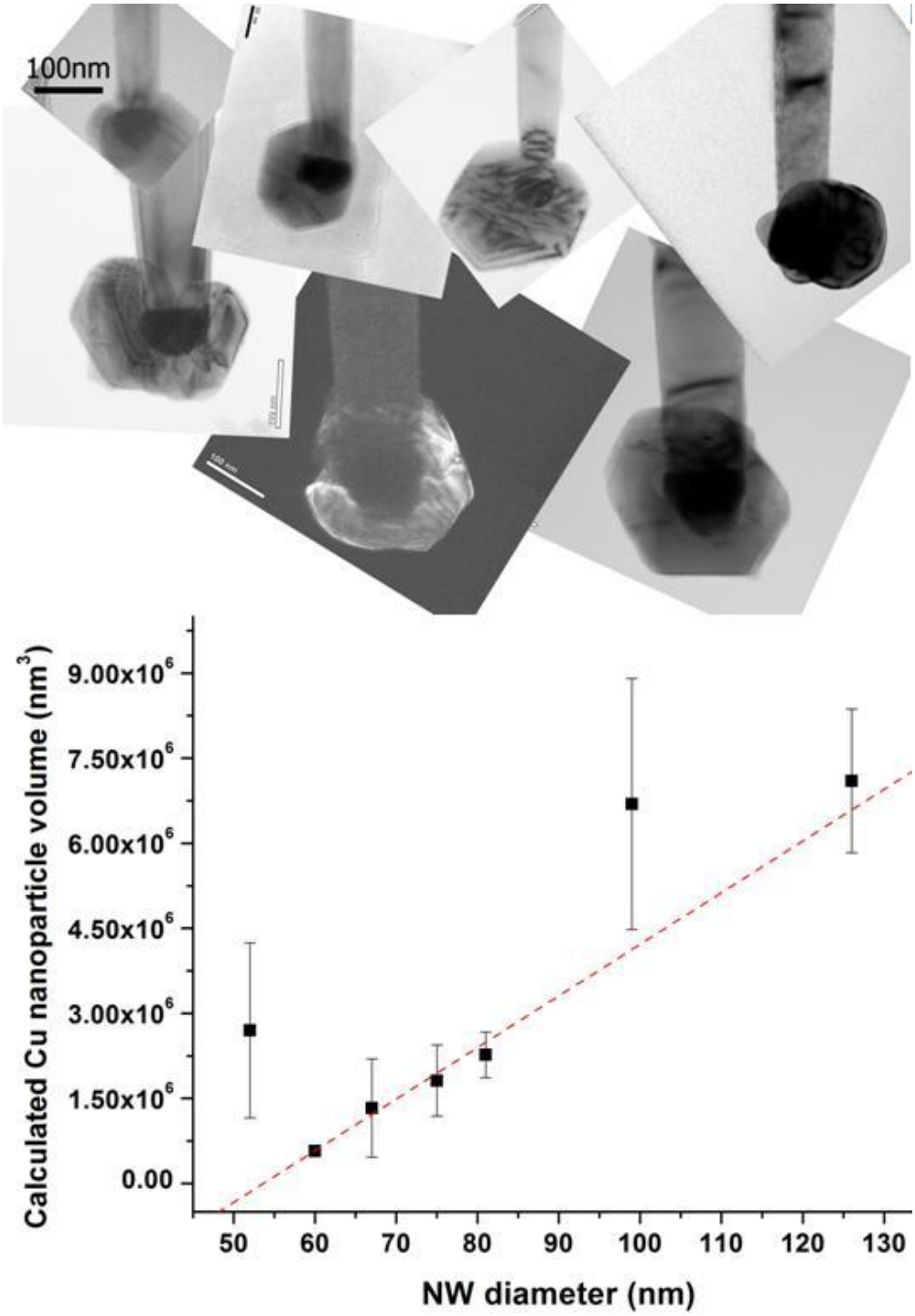

Figure 3.9: Top: TEM images of intentionally carbon-doped GaAs NWs (type A) after electrodeposition of Cu for 80 s. Bottom: Plot of calculated Cu nanoparticle volume as a function of NW diameter. The dotted line is the best linear fit.

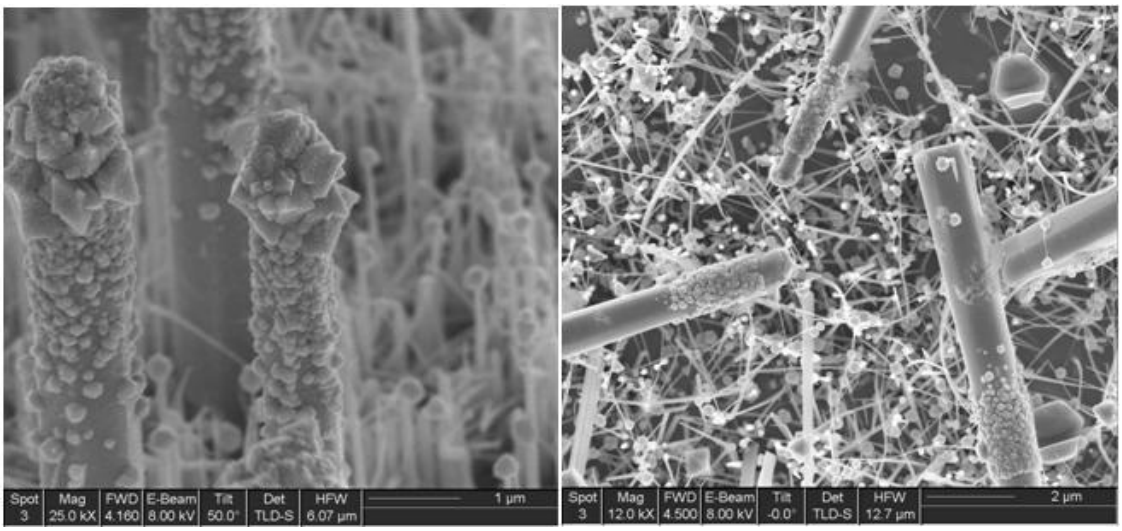

Figure 3.10: SEM images of GaAs NWs (Type A carbon-doped) with large diameters after deposition of Cu for 40s.

3.2.2 Carbon-doped GaAs NWs with Type B (TMGa) precursors

The Type B GaAs NWs intentionally doped with CBr4 had diameters that ranged from 40 nm to 120 nm, with an average diameter of 50 nm. As shown in Figure 3.11, the NWs also adhered together due to the capillary effect. Similar to undoped GaAs NWs grown with Type A (TEGa) precursors, we found Cu only grew around the NW bottom and at the top. An evaluation of the relationship between NW diameter and Cu volume was not carried out since clustering made it too difficult to distinguish how many wires belonged to each Cu nanoparticle.

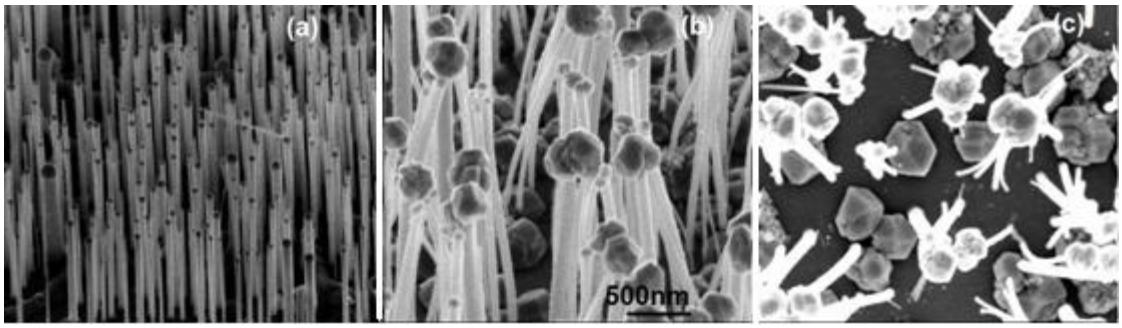

Figure 3.11: SEM images of GaAs NWs before (a) and after (b, c) electrodeposition of Cu for 30 s. (a)(b) are tilted images while (c) is a top-down view.

3.2.1 Core-shell (Type B -Type A) GaAs NWs

A core-shell GaAs NW sample was made by first growing an undoped core using Type B (TMGa) (200 s) with a 1 nm annealed gold layer, and then growing a CBr4 - doped Type A (TEGa) shell (400 s). The diameters of the NWs ranged from 60 nm to 120 nm, with an average length of 1.5 μm. Figure 3.12 (left) shows that a little tapering is visible near the top part of most NWs, which is due to a change from undoped to doped core growth at the Au end. Figure 3.12 (right) clearly shows that Cu has grown on the sides around the NW while a large Cu particle still exists on top of the NW. Also for certain wires, it appears nothing grew right below the top part of the NW, which is likely due to the depletion of Cu ions near the Au tip. Analysis of the Cu shell diameter and the core NW diameter (Figure 3.13) indicates that the Cu diameter increases for NWs with larger diameters.

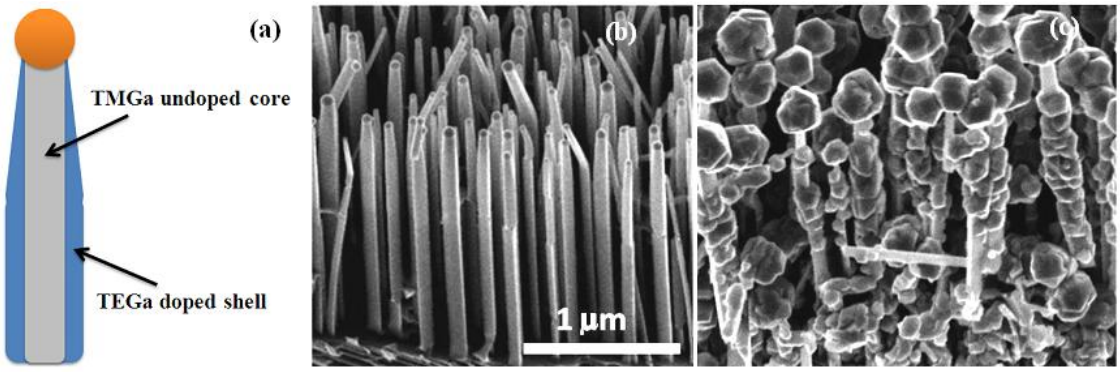

Figure 3.12: Sketch of the NW sample (a) and SEM images of undoped core, carbon-doped shell GaAs NWs before (b) and after (c) electrodeposition of Cu for 40 s.

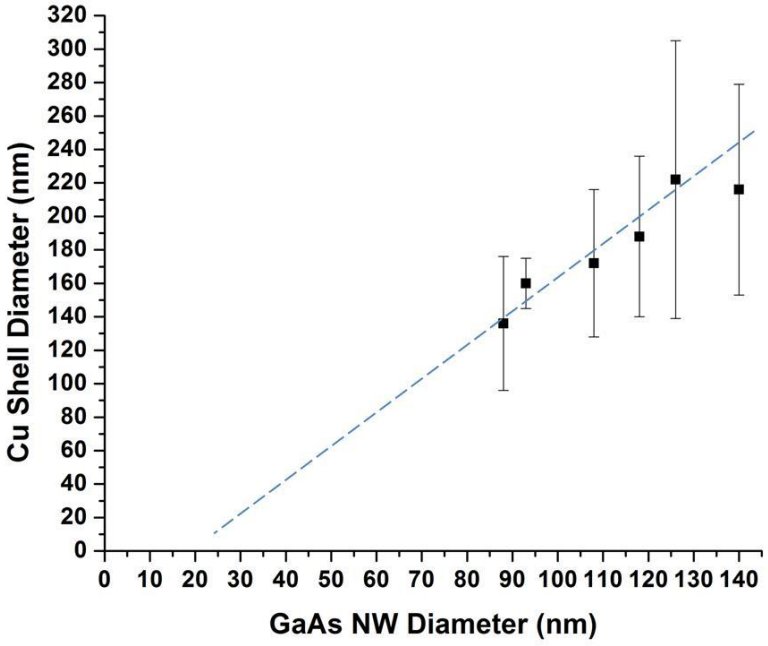

Figure 3.13: Plot of Cu crystal diameter growing on the sides of the NW versus NW diameter.

3.3 Electrodeposition of Fe on GaAs nanowires

Fe was deposited onto Type A GaAs NWs grown with CBr_4 for the first part of the growth, followed by no CBr_4 precursor during the last part of the growth. It was found that tapering occurs when the carbon source is turned off [12]. As we can see in the SEM images shown in Figure 3.14 the upper part of the GaAs NW is tapered while the lower part is uniform in diameter. Again, Fe is only depositing on the top end of the NW where the Au is. The SEM image shows that no Fe has grown on the smallest wires.

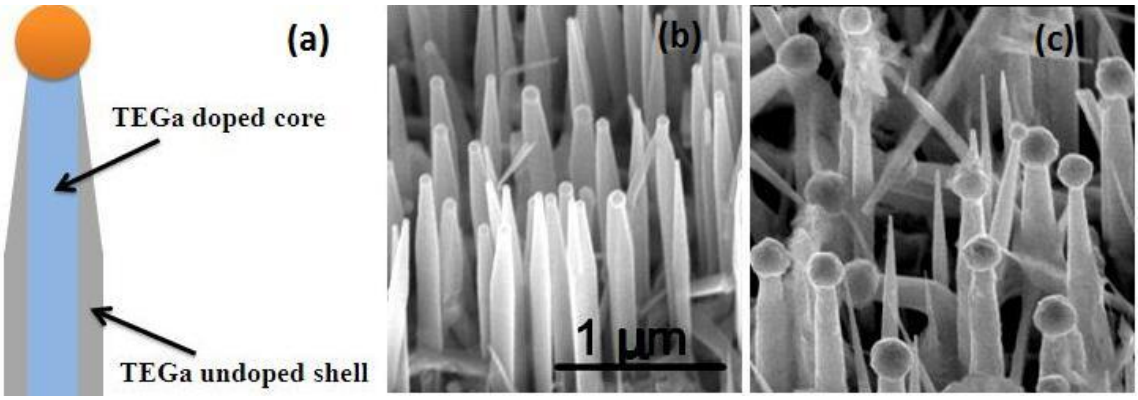

Figure 3.14: Sketch of the NW sample (a) and SEM images of GaAs NWs before (b) and after (c) electrodeposition of Fe for 30 s. Tapering in the wires towards the Au end occurred when the CBr_4 was turned off in the later part of the growth.

Figure 3.15 is the plot of Fe volume versus NW diameter. We assumed again spherical-shaped particles for the volume calculation of Fe nanoparticle. The best linear fit has a threshold of 30 nm, indicating that there is no growth of Fe on NWs with a diameter smaller than 30 nm.

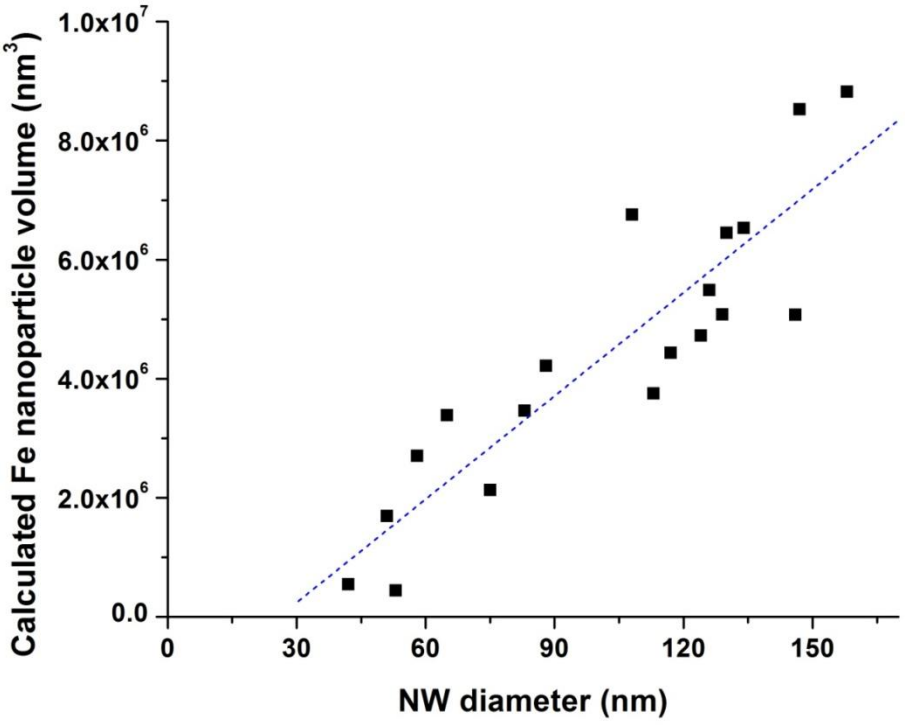

Figure 3.15: Plot of calculated Fe nanoparticle volume as a function of NW diameter. The dotted line is the best linear fit with a intercept of 30 nm.

Figure 3.16 shows TEM and an associated SAD pattern for one of the nanowires from the sample in Figure 3.14. The TEM image shows that the NW grew along a (111) direction but that the Fe is not single crystalline. The Fe diffraction spots are indexed on the SAD. The dark field image intensity from the Fe spot is not uniform everywhere in the Fe region.

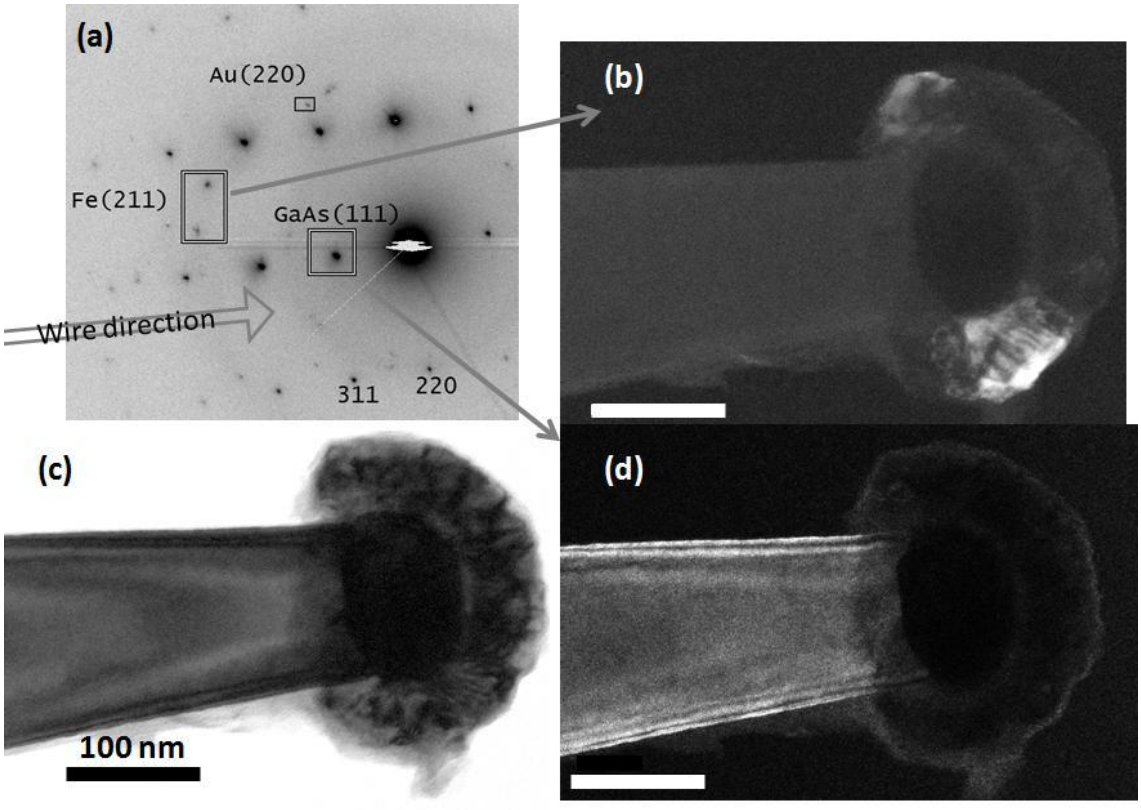

Figure 3.16: TEM images of the GaAs NW after deposition of Fe for 30 s. (c): BF image and (a) SAD pattern. Dark field images (c) from Fe (211) spot, (d) from GaAs (111) spot.

Figures 3.17 and 3.18 show EDS spectra from two spots on the wire sample imaged in Figure 3.16. They confirm that there is no detectable Fe growth on the GaAs sidewalls. From the EDS spectrum from spot (1) of Figure 3.19 we can see that a large Fe peak is detected. And there is no oxygen peak, which confirms the deposit is Fe not FeO_x.

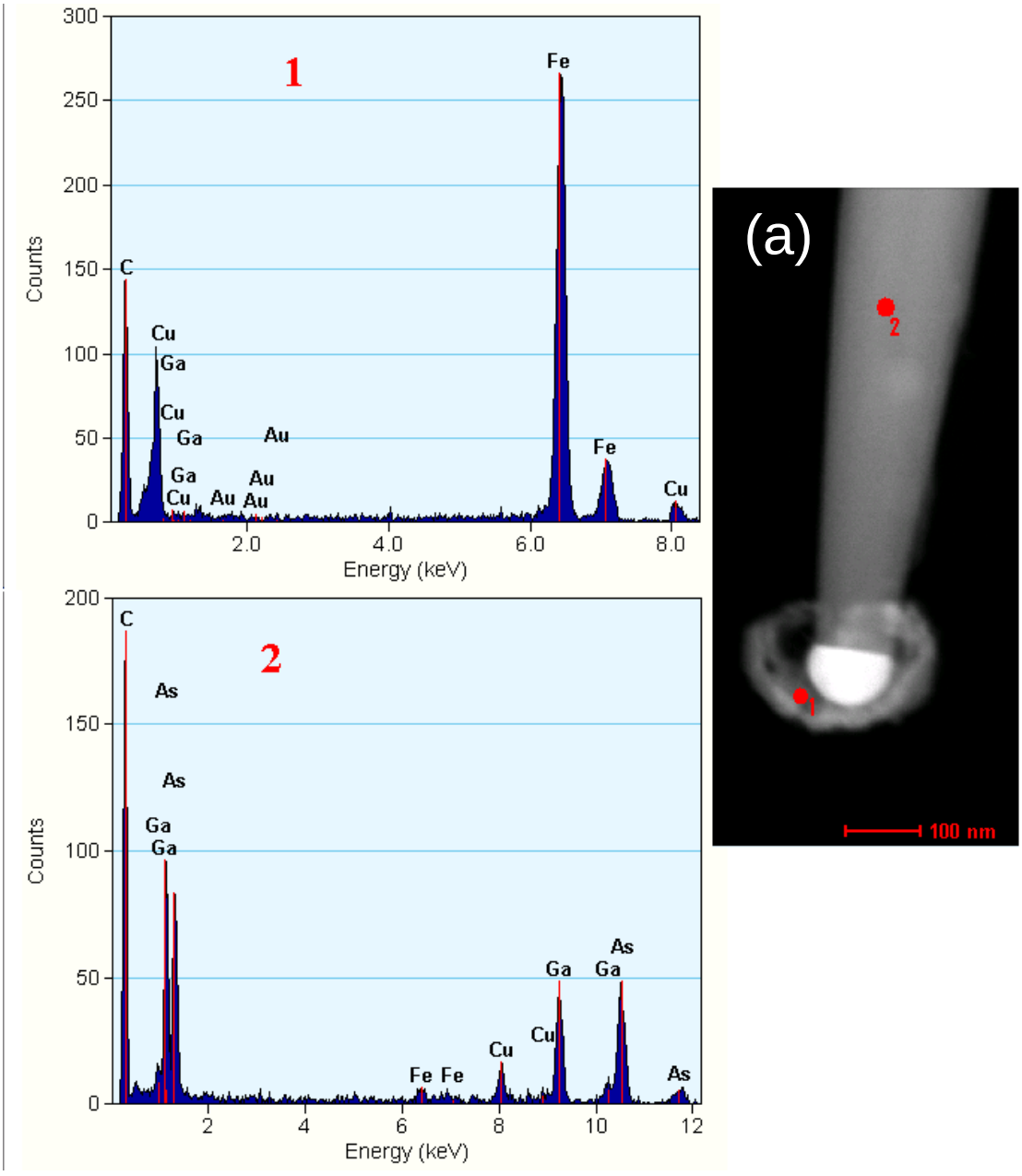

Figure 3.17: (a) STEM image of a GaAs NW after deposition of Fe. The numbers indicate the location where the EDS spectra (1) and (2) were obtained. The carbon (C) and Cu signals are from the holey carbon-coated TEM grid (copper mesh).

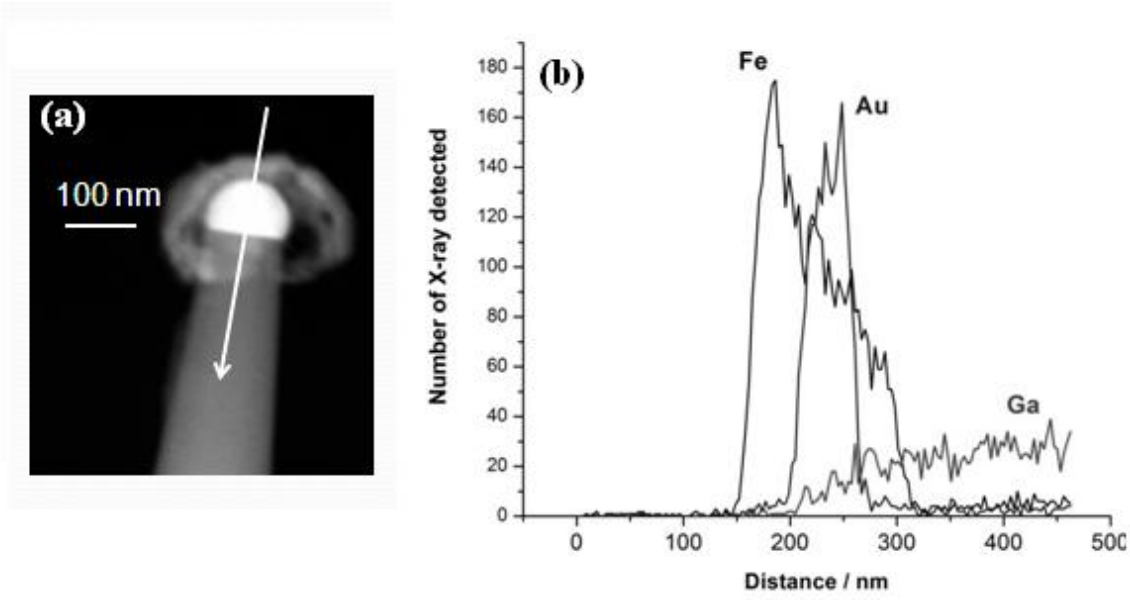

Figure 3.18: (a) A STEM image of the Au end of another wire electrodeposited with Fe. The arrow shows the path of the focused electron probe that was used to excite x-rays collected by the EDS detector. (b) The resulting analysis of EDS spectra as a function of position along the arrow. We can see that the Fe region covers the Au region and the intensities both drops to zero within 20 nm when on the GaAs wire.

The Ga signal declines towards the Au end, which is related to its decrease in diameter. There is Ga detected in the Au. The Ga signal that overlaps the Fe signal suggests that the Fe is growing on the wire but more likely it has simply grown out from the Au. There is no Fe signal on the wire away from the Au.

3.4 Electrodeposition of metal on InAs nanowires

3.4.1 NRC InAs NWs

The NRC InAs nanowires were patterned into different arrays with different number of wires. Figure 3.19 (a) shows an SEM image from one area of the sample showing that the wires have typically a diameter of 160 nm, with an average length 1.5 μm and average NW spacing of 340 nm. Figure 3.19 (b) shows another region on the same sample with fewer wires in a line with a spacing of 380 nm. The EDS spectrum is shown in Figure 3.20 obtained using an electron beam energy of 5 keV. The peaks identified include those from the InAs wire, InP substrate, and the SiO_2 layer.

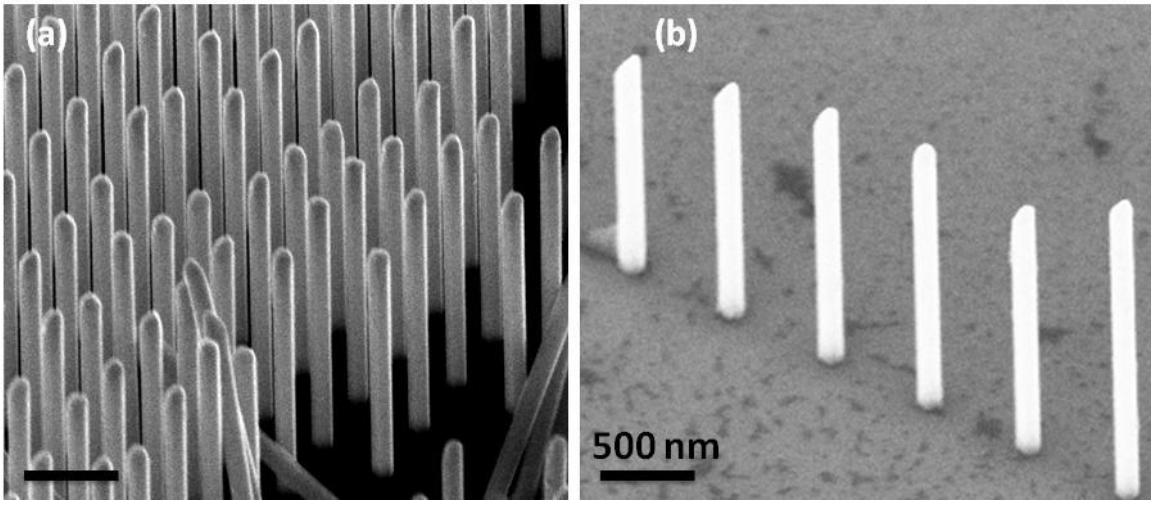

Figure 3.19: SEM images of InAs NWs from NRC obtained from two regions of the same SiO_2/InP patterned wafer, sample tilted 45°.

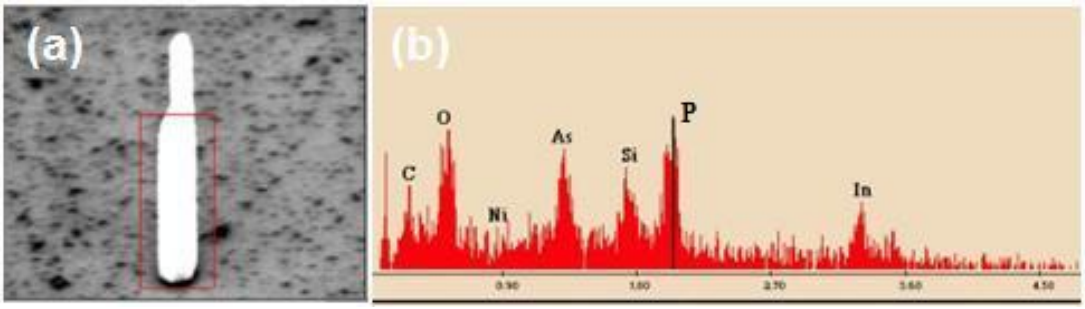

Figure 3.20: (a): SEM image of one InAs NW growing through a SiO_2 masked InPsubstrate. (b): EDS spectrum from the rectangular region in (a).

3.4.1.A Electrodeposition of Cu

There were different sizes of NW arrays in the sample but all wires had the same diameter of 160 nm. To choose the electrodeposition current applied by the constant current supply such that the current density was 0.1 mA/mm^2 the total sample area was equal to the number of InAs nanowires times this individual areas. Figure 3.21 shows the experimental results for different patterns of InAs NW arrays on the same sample electrodeposited simultaneously. We can see that the single InAs NWs are fully covered with Cu uniformly all over the wire. Compared to the single NW, less copper is found in the NW forest where the wires have the same size but a larger number and density. This is probably due to depletion of Cu ions. According to the EDS spectrum of Figure 3.22, the solid that has grown around the InAs NW is Cu and not CuO. CuO would have generated a much stronger O peak.

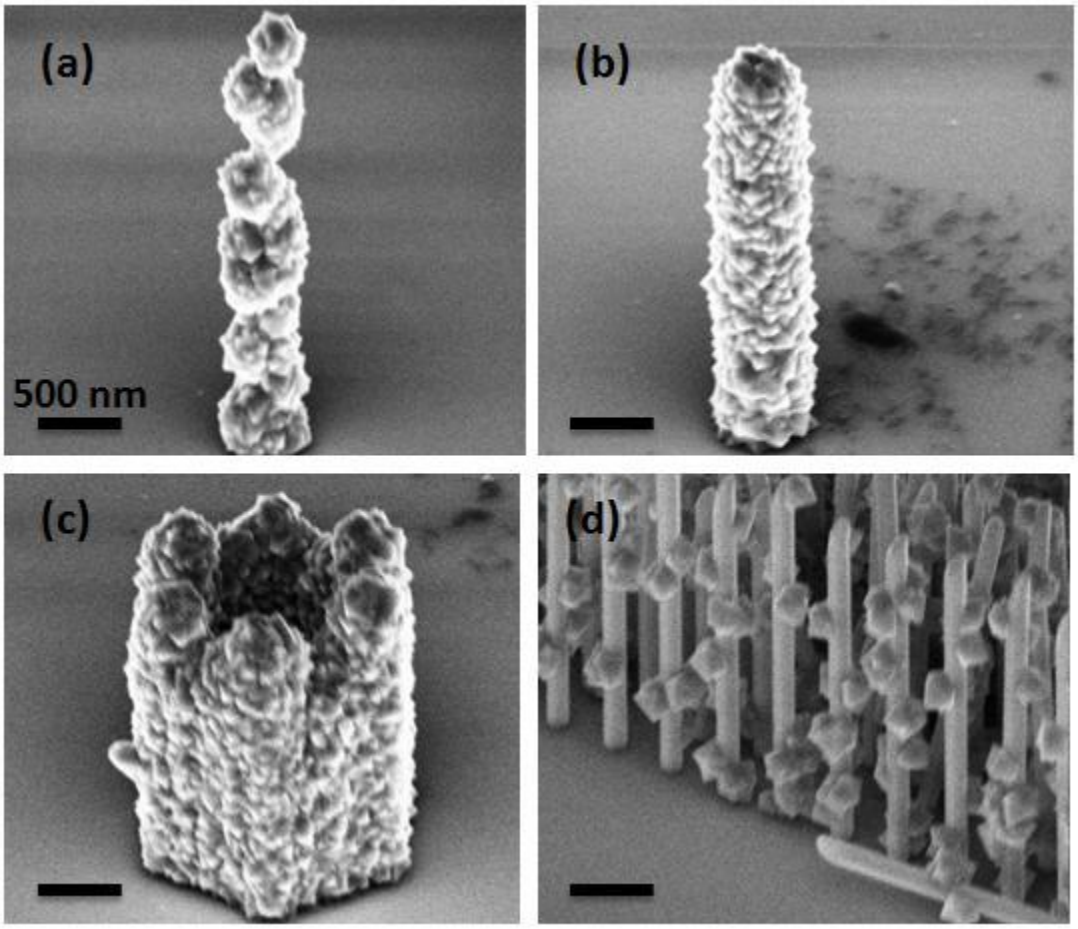

Figure 3.21: SEM images of InAs NWs with different array sizes after electrodeposition of Cu for 30 s. (a) and (b) single wire, (c) 6 wires and (d) forest wires. All wires have the same size, and wire arrays in (c) and (d) have the same density.

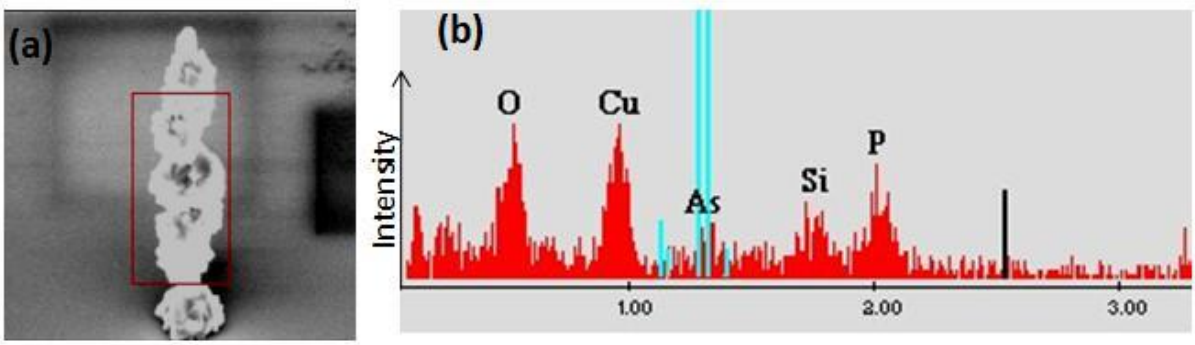

Figure 3.22: Left: SEM image of one of the InAs NW after deposition of Cu. Right: EDS spectrum of the rectangular area shown in (a).

3.4.1.B Electrodeposition of Fe

Electrodeposition at a total current 0.001 mA (estimated current density of 0.04 mA/mm^2) resulted in no evidence of deposition after 5 seconds based on SEM investigations. In a second attempt, at a total current of 0.002 mA (current density 0.1 mA/mm^2) deposition time 30 s, deposition was obtained. Figure 3.23 shows SEM images from a single NW and a small NW array from this experiment.

Comparing this result to Cu where the same current and deposition time was used, the Fe deposition is thinner. The cell voltage for the two depositions was different. For Cu deposition the cell voltage is 0.60 V while for Fe it was 1.08 V. The sample for Fe deposition was reused after the first attempt without additional cleaning. The 5 s deposition may have caused a change in the sample surface.

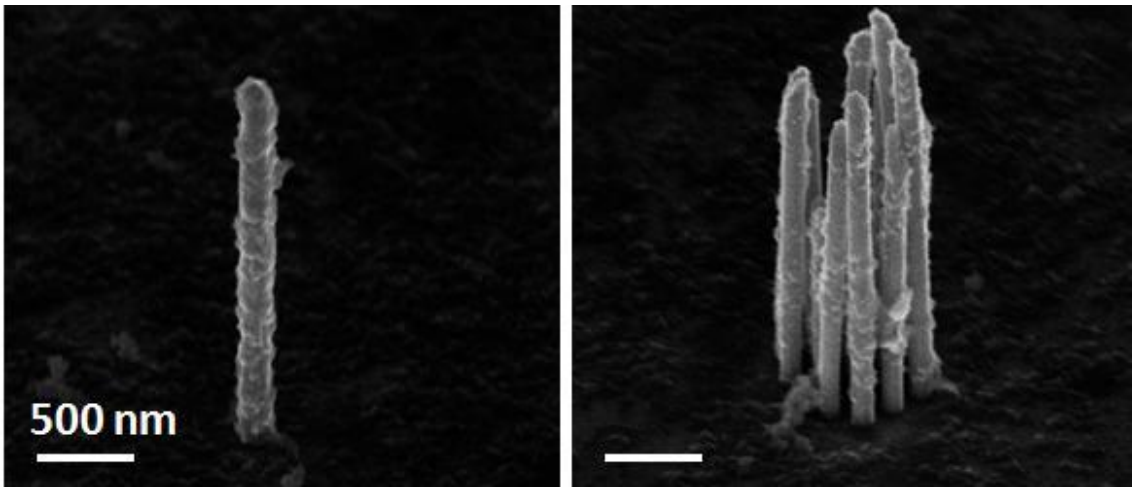

Figure 3.23: SEM images (45 ° tilted) of InAs NWs after electrodeposition of Fe for 30 s.

3.4.2 Electrodeposition of Cu on InAs NWs from Dr. Watkins' group

Figure 3.24 shows SEM images from the undoped InAs NWs from Dr. Watkins' lab. The wires are highly tapered with the top showing little evidence of Au particles. After deposition of Cu, we found solid Cu had grown around the NW with also some large Cu crystals randomly lying on the GaAs substrate surface.

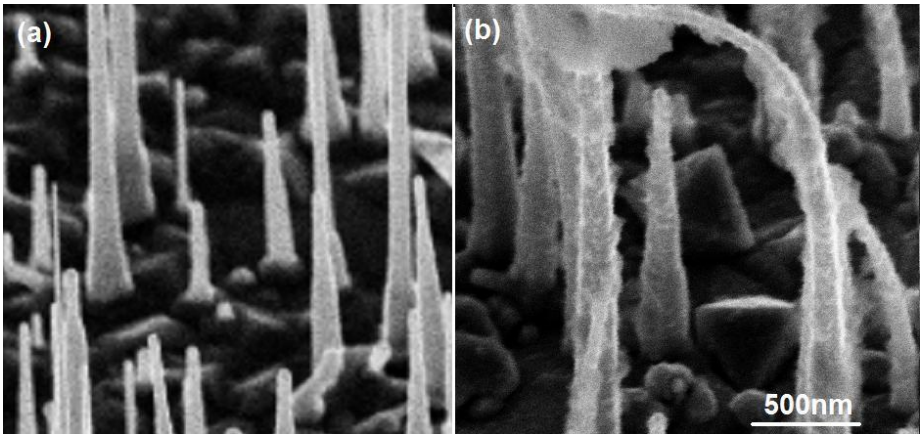

Figure 3.24: SEM images of InAs NWs before (a) and after (b) electrodeposition of Cu for 40 s.

3.5 Experiment with light illumination

Figure 3.25 shows SEM images of carbon-doped Type B GaAs NWs (TMGa precursors) after electrodeposition in the dark and under white LED flashlight illumination. We can see that with or without light during deposition, the Cu still prefers to grow at the NW top. Octahedrally faceted Cu crystals can be found in both samples. There is no significant difference in the Cu volume or deposition density.

Another experiment using the same sample was carried out involving simply putting the NW sample surface under LED illumination for 180 s. The sample is in the electrolyte and every other procedure is the same except that no current was supplied

(Keithley power supply off). A certain amount of metal growth will occur simply by providing the electrolyte. [32] SEM and EDS showed that the sample stayed the same as before, nothing was detected to have grown on the surface.

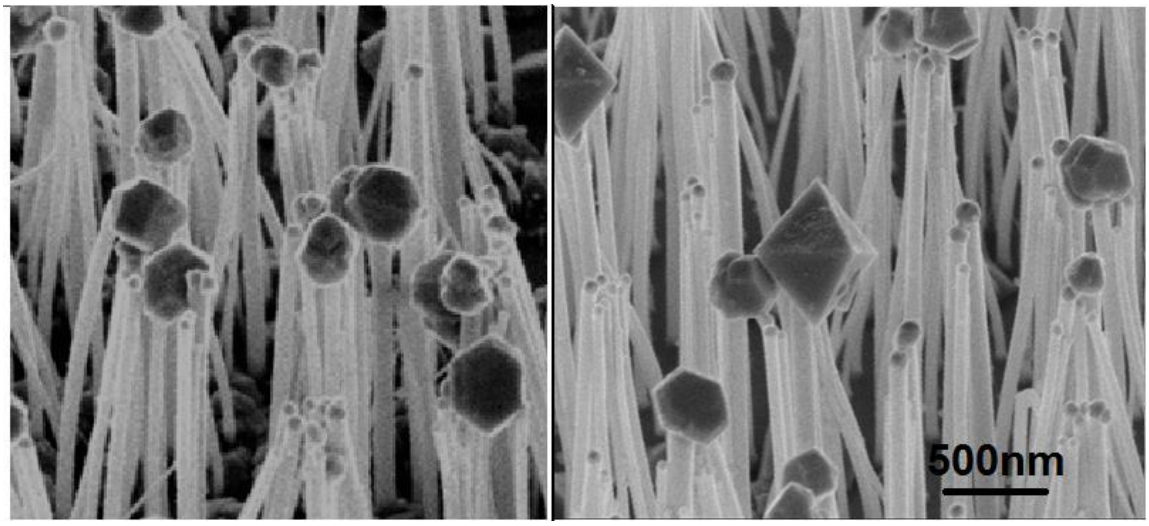

Figure 3.25: SEM images of GaAs NWs after electrodeposition of Cu for 30 s. Left: deposition in dark. Right: deposition under LED flashlight illumination.

3.6 Metal deposition without gold catalyst

3.6.1 Electrodeposition of Cu on gold nanoparticle samples

As a comparison experiment, we electrodeposited Cu on gold nanoparticle GaAs samples. The gold nanoparticle sample we used had a Au particle diameter distribution from 100 nm to 400 nm. By lowering the electrolyte beaker gradually during the deposition, we were able to change the deposition time of deposition on different areas of the sample in one experiment. As we can see in the series of SEM images in Figure 3.26, at first, Cu crystals grow on a small numbers of Au nanoparticles. Then as time goes by, more Au nanoparticles have Cu growth; finally all Au particles are covered by Cu islands.

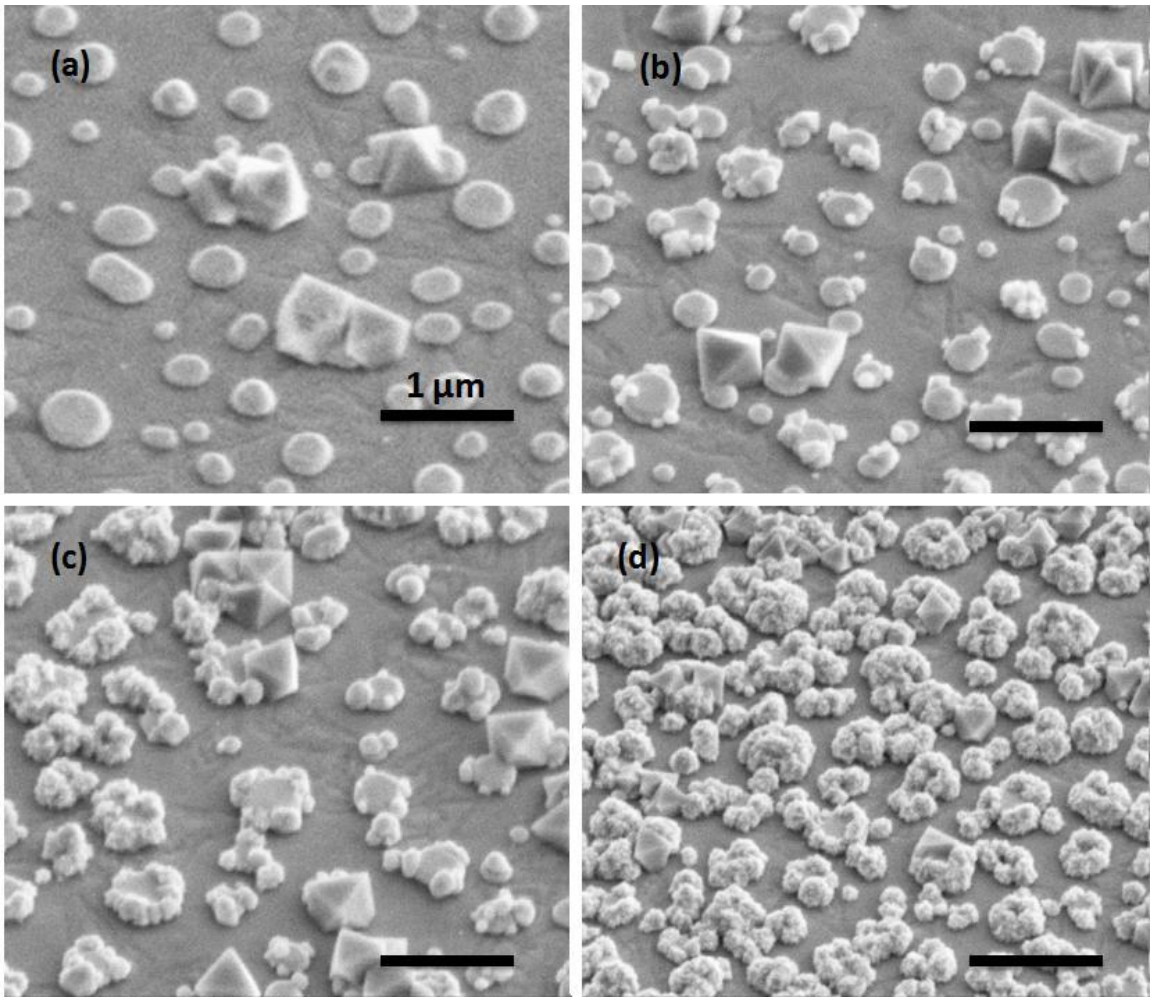

Figure 3.26: SEM images of Cu deposition on a gold nanoparticle/GaAs substrate sample as a function of deposition time obtained by moving the electrolyte in a stepped time series of (a) 3 s, (b) 6 s, (c) 8 s, and (d) 10 s.

3.6.2 Cu growth without gold catalyst

For this experiment we used carbon-doped Type A GaAs NWs (TEGa) with a range of NW diameters of 50 nm to 500 nm. The Au catalysts were etched as described in section 2.3. After making sure that most of the Au was gone (Figure 2.4), we used the sample for

electrodeposition following the same procedures as samples with Au. Figure 3.27 shows SEM images from wires showing the comparison between deposition with and without gold catalyst. We can see that with the Au catalyst, Cu hats are found on the tops of most NWs. In comparison, for the deposition without the Au catalyst, Cu still has a preference for growing on top of the NW but there is less growth on NWs having diameters smaller than 100 nm. Also, for the NWs with larger diameters, there is now more than one single crystal growing on top. Figure 3.28 shows two NWs with diameters of 125 nm (left) and 150 nm (right). The dark part on top of the 125 nm NW could be residual Au after the etching process. The 150 nm NW has a hexagonal-shaped Cu crystal growth on top and the contrast indicates that there is no Au catalyst left, supported by subsequent EDS analysis.

Figure 3.29 is a TEM image and associated SAD pattern from one NW with a diameter of 200 nm. The main periodic spots in the SAD pattern index to GaAs indicating that the NW is oriented with the electron beam perpendicular to a (112) GaAs plane. The expected Cu spot positions are shown by the added indexed diffraction rings. Considering the lattice mismatch between Cu and GaAs the Cu (111) atomic spacing (0.2087 nm) is most closely matched to GaAs (220) atomic spacing (0.200 nm) with a 4% lattice spacing mismatch. There are spots from Cu crystals that are consistent with more than one single crystal of Cu having grown on the top of the wire, consistent with our SEM analysis. There is no evidence of an epitaxial arrangement of the Cu on the GaAs.

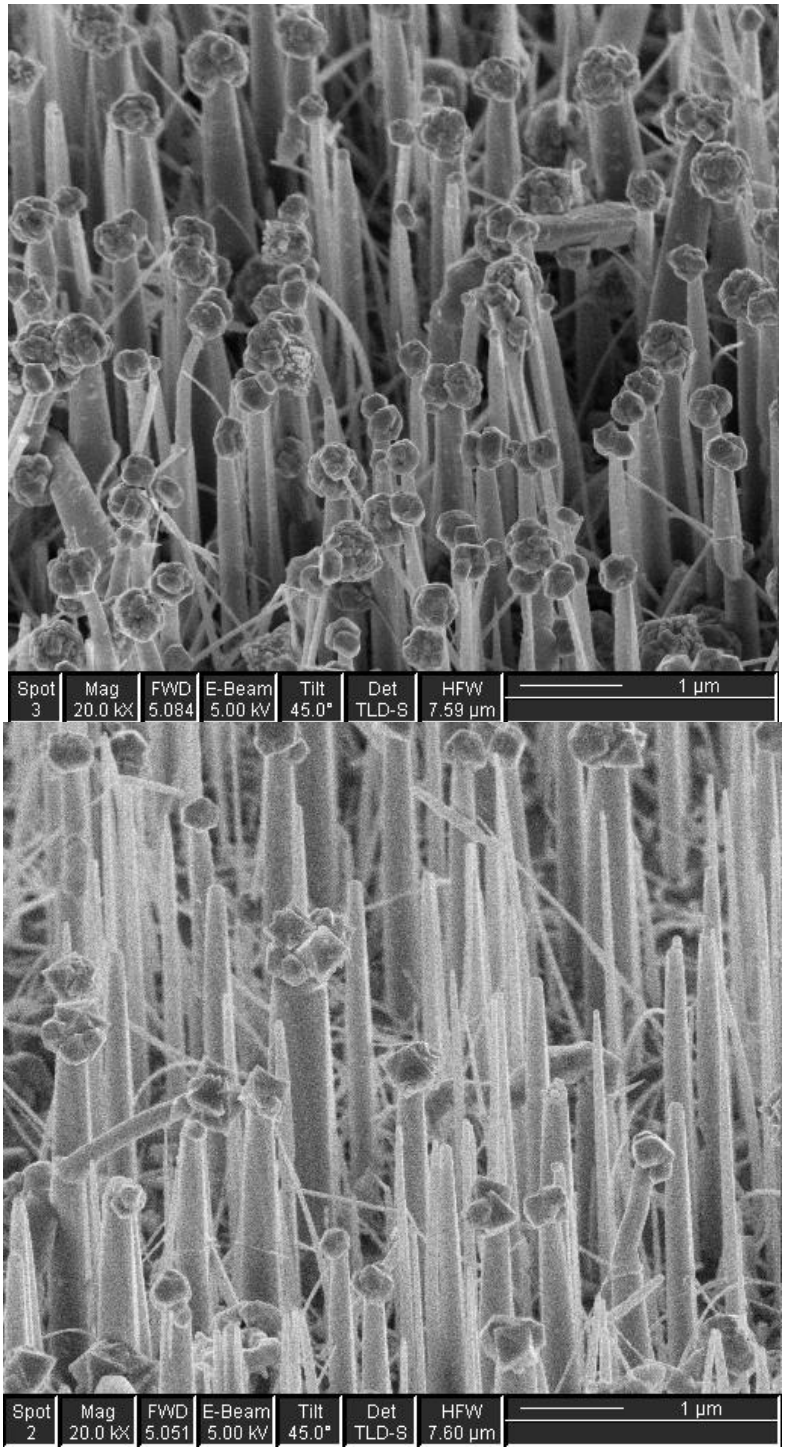

Figure 3.27: SEM images of carbon-doped GaAs NWs (Type A) after 40 s electrodeposition of Cu. The upper image is NWs with Au catalysts while the bottom image is after etching the sample in an HCl: potassium-tri-iodide solution to remove the Au catalysts.

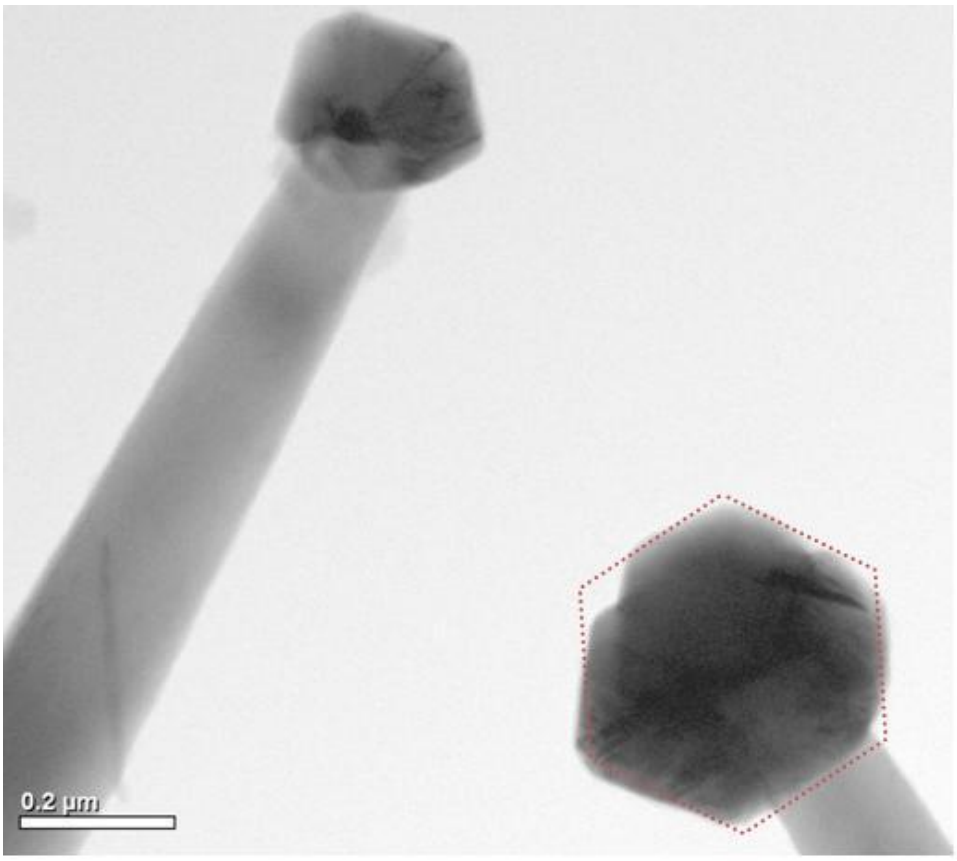

Figure 3.28: TEM images of GaAs NWs where the Au was etched prior to electrodeposition of Cu (40 s).

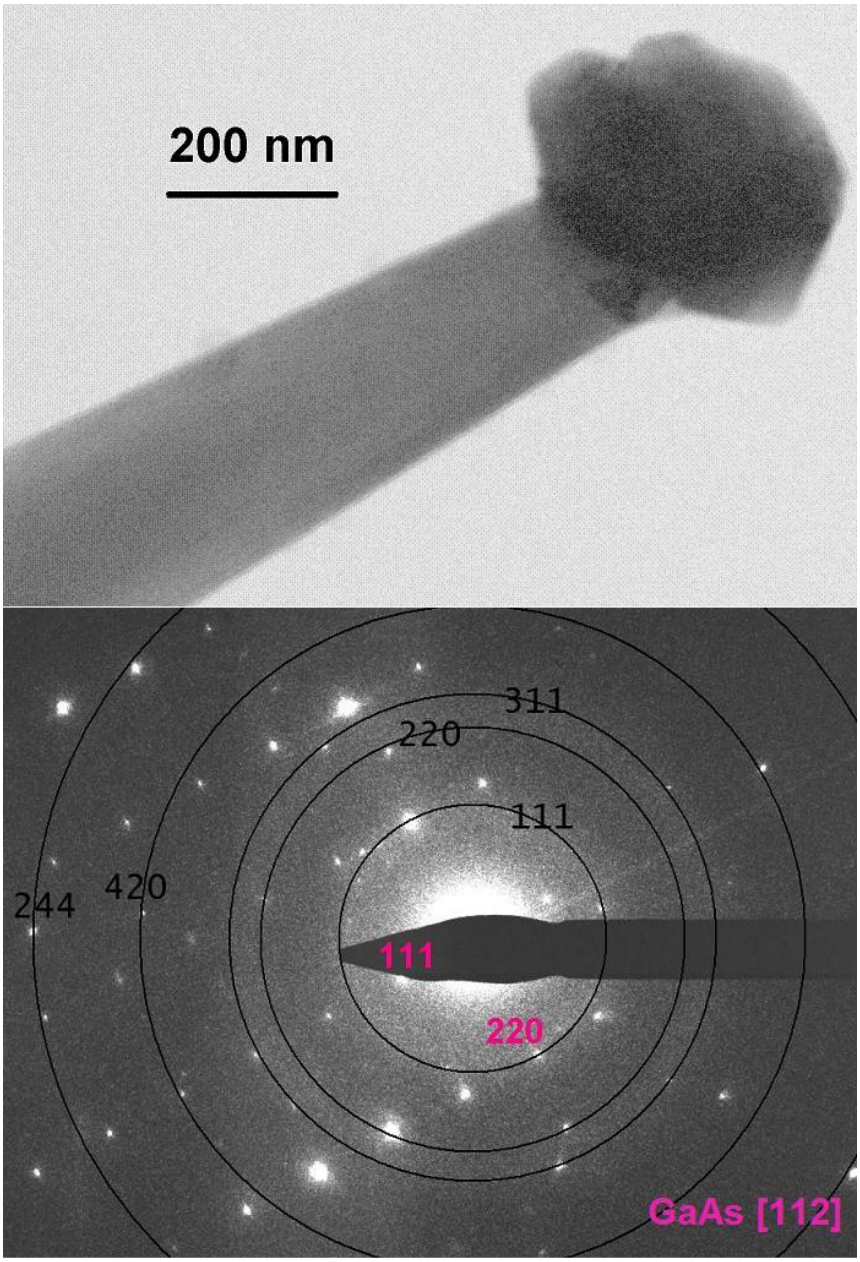

Figure 3.29: TEM bright field image of a zincblende GaAs NW with associated SAD pattern. The diffraction pattern indicates that the electron beam was perpendicular to a GaAs (112) plane. The (hkl) indices are GaAs diffraction spots while the labelled black circles are calculated diffraction rings for polycrystalline Cu.

4: DISCUSSION

In our experiments, we have tested samples with different morphology (metal nanoparticles on semiconductor, semiconductor NWs on top of semiconductor), conductivity (InAs NWs and GaAs NWs with different carbon doping levels) and structure (diameter, with and without gold catalyst at the growth end). The conductivity and actual dopant impurity concentration in the GaAs wires investigated was unknown. We found that metal deposition happened in different locations for different samples and we propose that this was due to variations in the conductivity. We discuss the growth mechanism as a function of sample surface, conductivity and morphology. COMSOL finite element analysis was carried out to simulate the experimental results based on the Butler-Volmer equation and Nernst-Planck equation.

4.1 Current and resistivity calculation

From the estimated Cu crystal volumes, *V*, as described previously in section 3.2, we can obtain the total charge, *Q*, that is transferred during deposition through the gold/electrolyte interface given by:

$$\mathrm{Q} = \frac{\rho}{\mathrm{A_r}} \mathrm{zeVN_A} \tag{4.1}$$

where ρ is the atomic density of Cu, A_r is atomic weight and N_A is Avogadro's number, z = 2 is the Cu ion valence. The total charge divided by the deposition time will give us the average current through the NW. The challenging part for further calculation of the NW resistance is that we do not know the voltage drop across the length of the NW. If we

ignore the voltage drop of the outer cell circuit (which is very small), our system primarily measures the potential drop between the cathode and anode. The *n*-type GaAs substrate and *p*-type C-doped GaAs NW interface is a forward biased *p*-*n* junction during deposition. Since the cathode is platinum and the anode wafer is heavily-doped *n*-type GaAs (350 ± 25 μm thickness), the voltage drop mainly occurs inside the semiconductor NW, the Helmholtz layer and the electrolyte. To make a rough approximation, we assumed 1.5 V out of the total 2 V voltage drop as the potential difference across the NW, from the NW base at the wafer surface to the gold tip. From TEM or SEM images we can measure the length and diameter of NWs, and then use

$$\rho = R\frac{A}{l} \tag{4.2}$$

for resistivity estimates.

Data for Cu volume versus NW diameter for the intentionally carbon-doped sample discussed in section 3.2.1 (type A) was shown in Fig. 3.9. This was used to calculate the average current and resistivity as a function of GaAs NW diameter via equations 4.1 and 4.2, respectively. . The current increases, up to 2.5 pA as the diameter increases. The 52 nm diameter NWs were more conductive than the 60 nm-90 nm ones, which might be due to a higher doping level [33]. Figure 4.1(b) is a plot of current versus NW cross-sectional area. The slope of the best linear fit line gives us the average current density, which is 0.24 ± 0.09 mA/mm^2, the same order of magnitude as the applied current density (total current divided by sample area times 40%, 0.1 mA/mm^2). The calculated average resistivity was 2 ± 1 x 10^4 Ωm, equivalent to bulk GaAs with a very low carrier density ~10^{10} cm^{-3} [34].

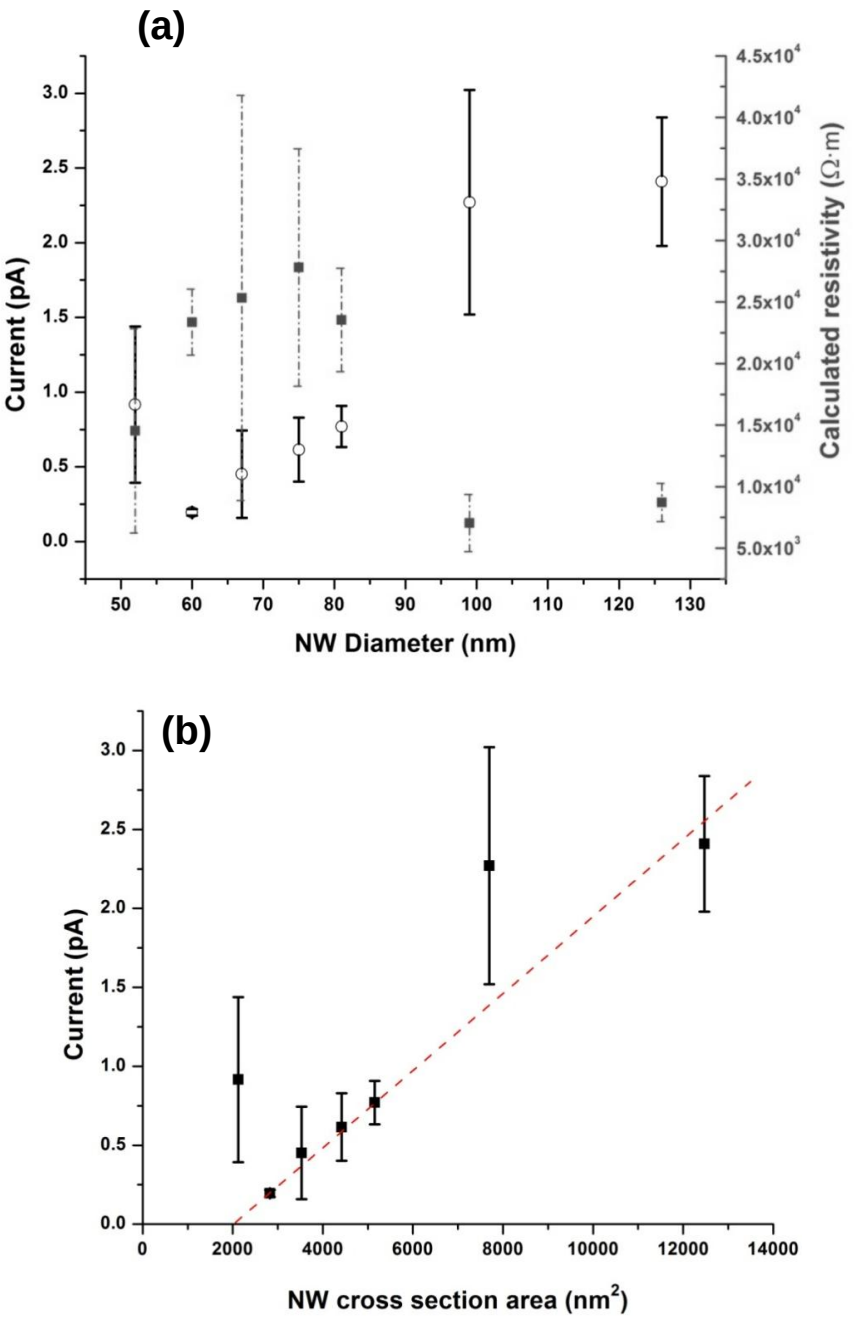

Figure 4.1: (a) NW current (solid circle point) and calculated resistivity (dashed square point) versus NW diameter and (b) current versus NW cross-sectional area for Cu deposition on carbon-doped GaAs NWs (type A) (section 3.2.1). The dashed line is the best linear fit with slope 2.4 ± 1 x10^{-4} pA/nm^2 (average current density: 0.2 ± 0.1 mA/mm^2)

Figure 4.2 shows the calculated current and resistivity for the Fe-deposited NWs grown on type A NWs with CB_4 doping for the initial part of the MOVPE growth, as discussed in section 3.3. In Figure 4.2 (a) the current increases up to 5.5 pA as the diameter increases. The intercept at 30 nm indicates that deposition on NWs with diameters smaller than 30 nm did not occur. From the slope of Figure 4.2 (b) the calculated average current density is 0.17 ± 0.05 mA/mm^2. The calculated average resistivity for this sample is also ~10^4 Ωm.

The same calculation was carried out using the Cu volume measurements from Cu-deposited onto undoped GaAs NWs (type A) described in section 3.1.1). The average current through these wires was 0.8 pA and the calculated resistivity is therefore, 2400 ± 900 Ωm, equivalent to bulk GaAs with a carrier density ~10^{11} cm^{-3}. The undoped wires are apparently slightly more conductive than those that were intentionally carbon-doped based on this model calculation. . It has been reported that the resistivity of VLS grown undoped GaAs NW is ~ 500 Ωm by transmission-line *I-V* measurement [35] comparable to our result. However, it is unlikely that the level of dopant impurities in our wires was less than typcial values for planar grown MOVPE GaAs (~10^{16}/cm^3). The calculated high resistivity indicates that all NWs grown with or without CBr_4 with diameters under 200 nm discussed in this section were likely fully depleted. We will discuss the depletion width in more detail in section 4.3.1.

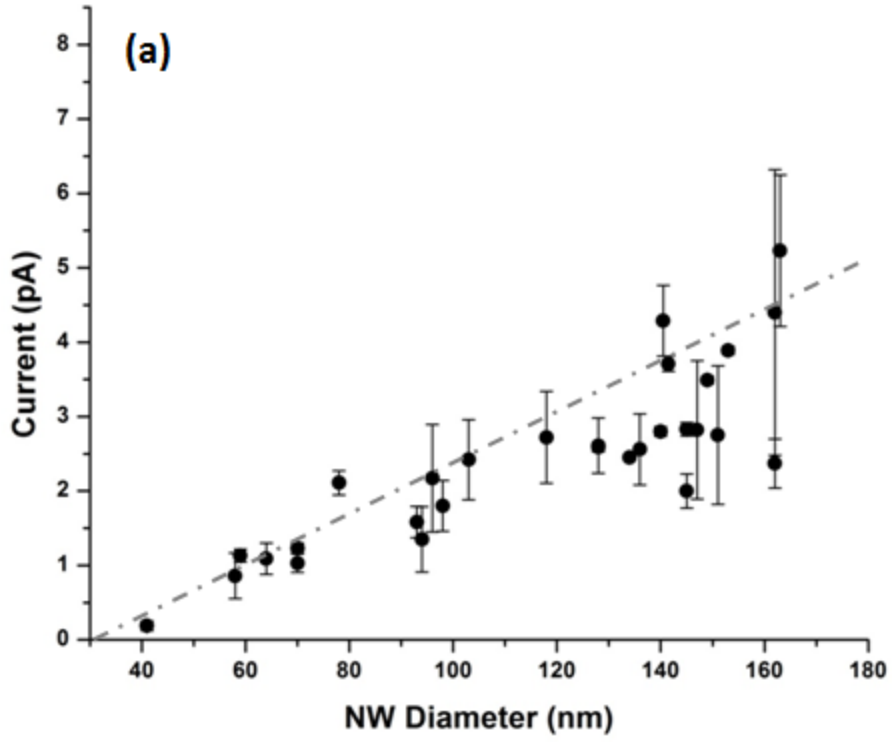
(a)
Current (pA)
NW Diameter (nm)
0
1
2
3
4
5
6
7
8
40
60
80
100
120
140
160
180

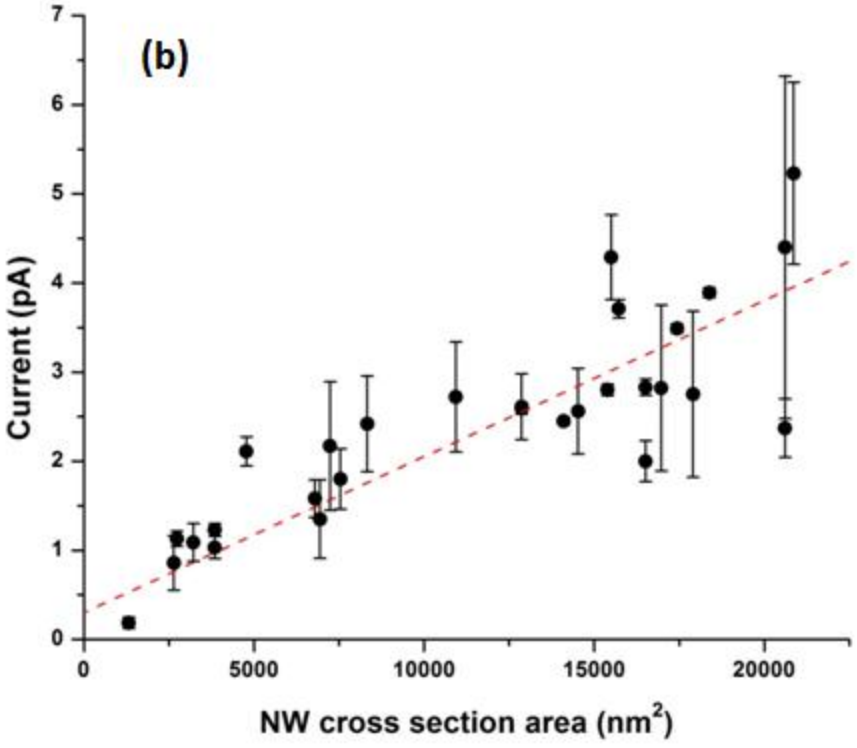
(b)
Current (pA)
NW cross section area (nm^2)
0
1
2
3
4
5
6
7
0
5000
10000
15000
20000

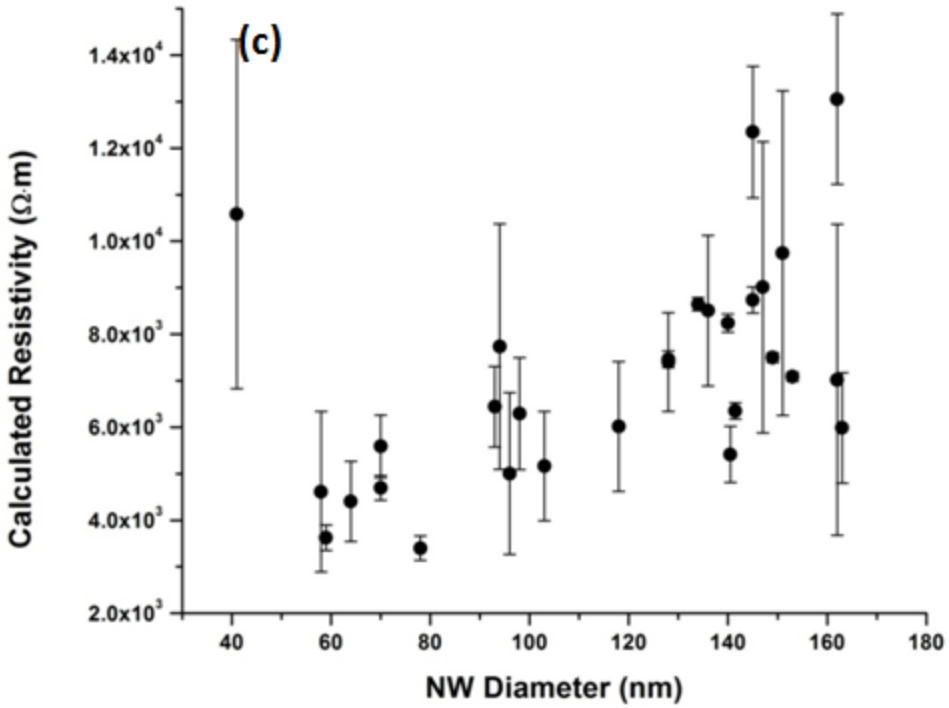

Figure 4.2: (a) Calculated current versus NW diameter and (b) NW cross-sectional area for Fe deposition on intentionally carbon-doped followed by undoped type A GaAs NWs (section 3.3). The dashed line in (b) is the best linear fit with slope of 0.17 ± 0.05 mA/mm^2. (c) Plot of the calculated resistivity as a function of NW diameter.

4.2 COMSOL simulation

To better explain the deposition results, finite element simulation was carried out using COMSOL® Multiphysics. We started with the simplest situation: the deposition process for a quasi-metal (InAs) NW without a gold catalyst. The model was built with the Chemical Engineering Module using the Nernst-Planck equation. [36] We simulated the electric field distribution for our electrochemical cell as applied to GaAs NWs using the AC/DC Module.

4.2.1 Cu deposition on InAs NWs

For the NRC InAs NWs sample, there were no gold catalysts. NWs grew from the InP substrate via openings in a deposited SiO_2 insulating layer. InAs NWs are naturally highly conductive due to their smaller bandgap (0.36 eV) and a surface accumulation layer [37]. All of these facts made the system easier to simulate.

The model system is designed by using the material balance for the ions involved: Cu^{2+} and SO_4^{2-} and the electroneutrality condition. The model geometry is depicted in Figure 4.3. The cell is fully filled with electrolyte. The anode is represented by the upper horizontal boundary while the cathode substrate is placed at the bottom a distance 30 μm away from the anode.

To make the model simple and not introduce other ions, we used Cu as the anode material. Thus, it is a copper dissolution process (reverse of deposition) on the anode. For the cathode, only the InAs NW portion of the sample has a current distribution. The vertical walls of the model cell are assumed to be insulating similar to the glass container of the real cell.

The flux of ions in the electrolyte is given by the Nernst-Planck equation [9]:

$$N_i = -D_i \nabla c_i - z_i u_i F c_i \nabla \phi_i \qquad (4.3)$$

where N_i denotes the flux of moving ions (mole m^{-2} s^{-1}), D_i is the ion diffusivity (m s^{-2}), c_i the concentration of ion in the electrolyte (mole m^{-3}), z_i the charge on the ionic species, u_i the mobility of the charged species ($m^2 s^{-1} J^{-1} mole^{-1}$) , F Faraday's constant (As $mole^{-1}$) and ϕ_i the potential in the electrolyte (V). The material balance is expressed by:

$$\frac{\partial c_i}{\partial t} + \nabla \cdot N_i = 0 \qquad . \qquad (4.4)$$

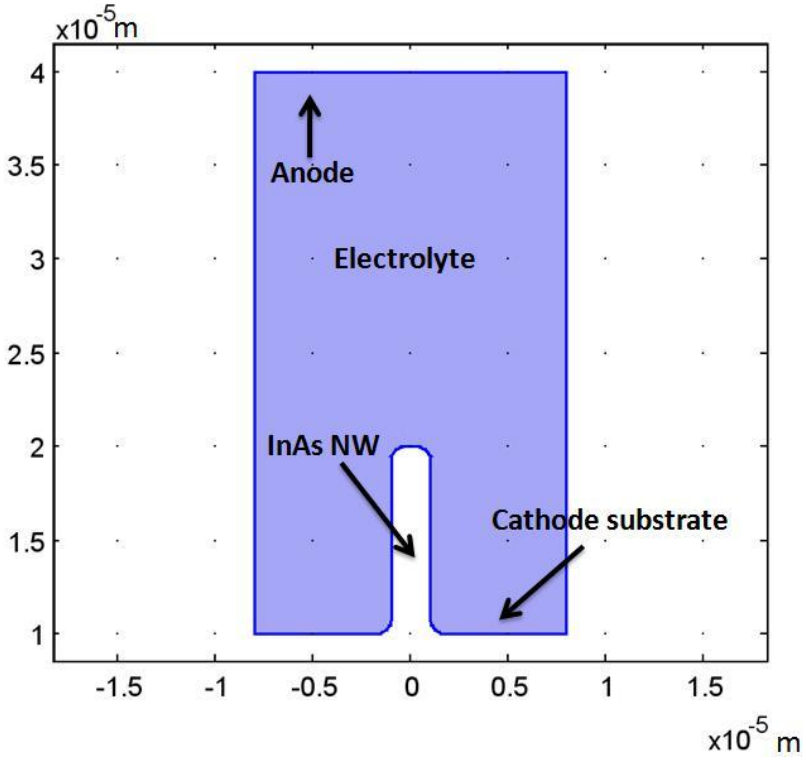

Figure 4.3: Sketch of the deposition cell model dimensions with anode, and cathode boundaries and insulating walls.

The electroneutrality condition is given by:

$$\sum_i (z_i c_i) = 0. \tag{4.5}$$

The boundary conditions for the upper anode and InAs NW cathode are given by the Butler-Volmer equation for copper deposition. The deposition process can be simplified into two steps:

$Cu^{2+} + e^- = Cu^+$

$Cu^+ + e^- = Cu$,

where the first reaction is the rate determining step[38]. This gives the following relation for the local current density as a function of potential [38].

$$i = i_0\left(\exp\left(\left(\frac{1.5F\eta}{RT}\right) - \exp\left(-\frac{0.5F\eta}{RT}\right)\right)\right) \quad (4.6)$$

where η denotes the overpotential:

$$\eta = \phi_{s,0} - \phi_l - \Delta\phi_{eq} \quad (4.7)$$

$\Phi_{s,0}$ denotes the electronic potential of the respective electrode, Φ_l the electronic potential of local electrolyte and $\Delta\phi_{eq}$ the relative equilibrium potential (which we set to 0 V). We set current density i_0 to be 100A/m^2 (0.1 mA/mm^2) and cathode potential -0.15 V and anode potential 0.15 V. For electrolyte potential, we set it to decrease uniformly from 0.15 V to -0.15 V from top to bottom. Then, for the InAs NW cathode:

$$N_{Cu^{2+}} \cdot n = -\frac{i_0}{2F}\left(\exp\frac{1.5F(\phi_{s,cathode}-\phi_l-\Delta\phi_{eq})}{RT} - \exp\left(-\frac{0.5F(\phi_{s,cathode}-\phi_l-\Delta\phi_{eq})}{RT}\right)\right). \quad (4.8)$$

The condition at the anode is:

$$N_{Cu^{2+}} \cdot n = -\frac{i_0}{2F}\left(\exp\frac{1.5F(\phi_{s,anode}-\phi_l-\Delta\phi_{eq})}{RT} - \exp\left(-\frac{0.5F(\phi_{s,anode}-\phi_l-\Delta\phi_{eq})}{RT}\right)\right), \quad (4.9)$$

where ***n*** denotes the normal vector to the electrolyte/electrode boundary.All other boundaries are insulating:

$$N_{Cu^{2+}} \cdot n = 0 \ . \quad (4.10)$$

For sulphate ions, insulating conditions apply everywhere:

$$N_{SO_4{}^{2+}} \cdot n = 0 \quad . \quad (4.11)$$

The initial concentration is set to be

$$C_{SO_4{}^{2+}} = C_{Cu^{2+}} = C_0 = 100\ \mathrm{mol/m^3} \quad . \quad (4.12)$$

Equation (4.4) (4.5) and (4.8) to (4.12) can be solved using the Nernst-Planck Equation interface by COMSOL. To keep track of a time-dependent deposition, we can calculate the growth rate by:

$$N = \frac{i_{cathode} M_{Cu}}{\rho z_i F} \quad , \tag{4.13}$$

where *M* denotes molar mass. The moving boundaries are treated through an arbitrary lagrangian eulerian (ALE) method incorporated inside COMSOL.

Simulation results

Figure 4.4 shows the simulation results after 1 s of deposition. The deposited Cu is represented by the blank part between the original domain boundary and the colourful mesh. From Figure 4.5 we can see that, as time goes by, the tip region has a slightly greater copper growth compared to the bottom. After 5 s deposition the simulation shows greater copper thickness at the tip compared to other parts, but the difference is relatively small. From the isopotential lines around the NW we can tell that the top part is denser which means a larger electric field. The model results tell us that if we have quasi-metal NWs (without gold catalysts) in the electrochemical system, under reasonable overpotential, Cu will deposit uniformly around the NW without a significant preference for the tip.

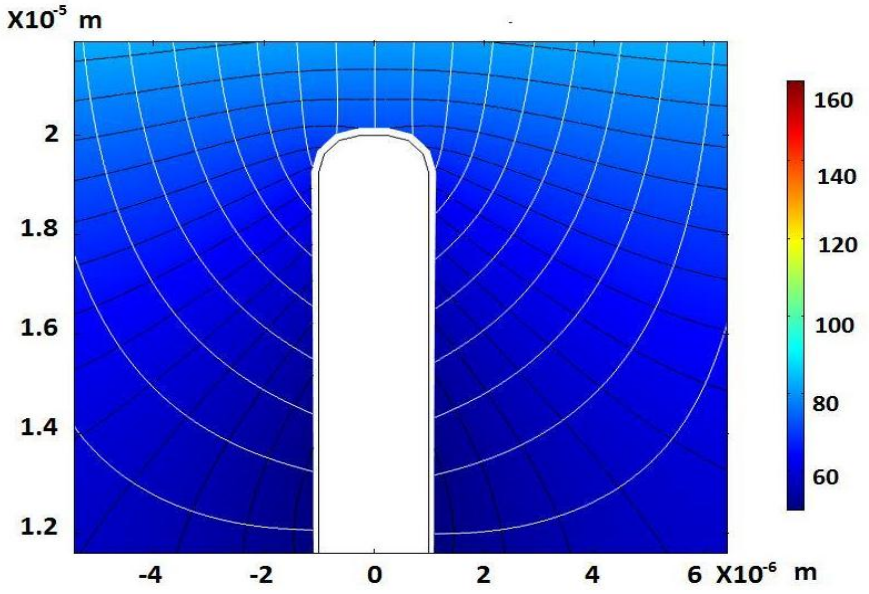

Figure 4.4: Copper ion concentration (mol/m^3), isopotential lines (black), total flux stream lines (white), and electrode displacement in the cell after 1 second of operation. The scale bar represents the copper ion concentration value.

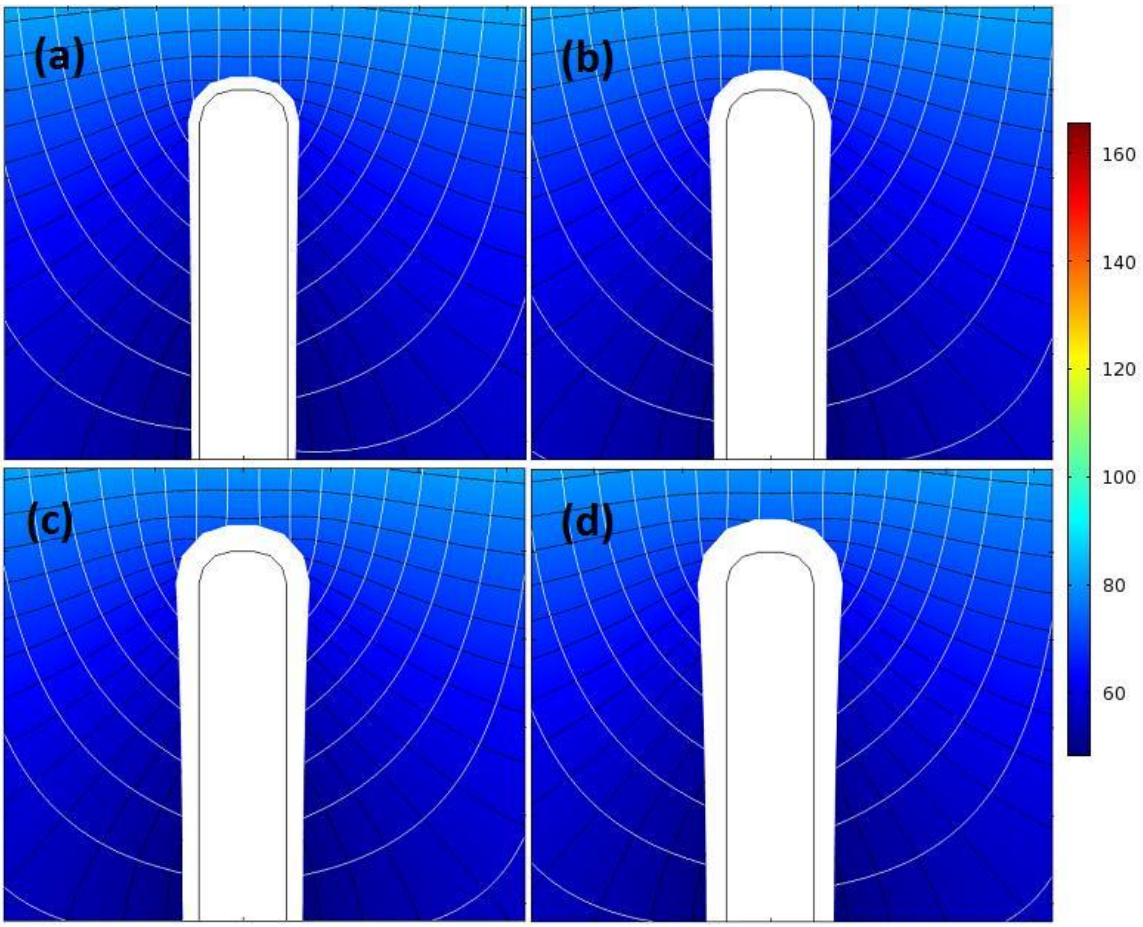

Figure 4.5: Copper ion concentration (mol/m^3), isopotential lines, total flux stream lines, and electrode displacement in the cell after (a) 2 s, (b) 3 s, (c) 4 s and (d) 5 s of operation. The scale bar represents the copper ion concentration value.

4.2.2 Electric field simulation for low conductivity GaAs NWs

For low conductivity GaAs NWs samples, there is no basic theory available to predict current flow when we have both semiconductor and metal as the nanoscale electrode. We found Cu only deposited around the NW bottom and at the top for the undoped and intentionally-doped GaAs NWs presented in 3.1.2 and 3.2.2. Also we found that Cu still had a preference for growing on the top even after we etched away the gold catalysts for

intentionally-doped NWs. If we compare our electrified NW to a high building in Figure 4.6, the gold catalyst at the tip of the NW acts like the lighting rod. The tip growth preference might be due to the higher electric field.

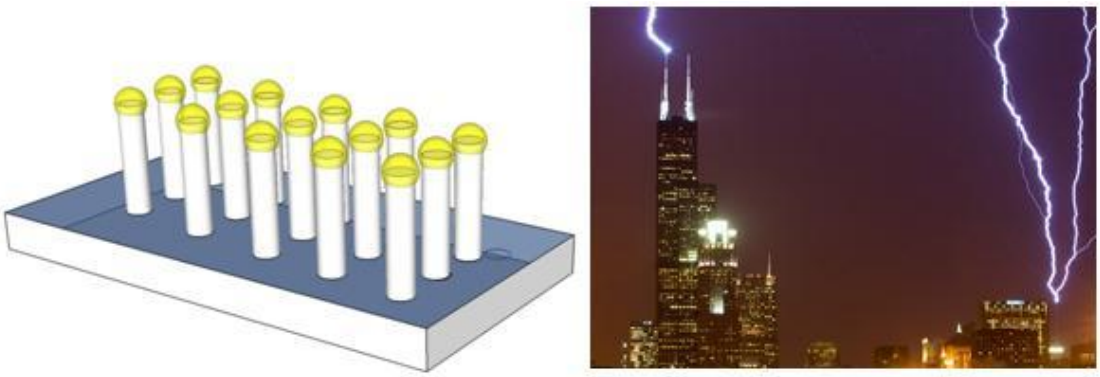

Figure 4.6: GaAs NW sample sketch and lightning rod picture from Nick Suydam; Flikr, Yahoo!; January 2008.

To improve our understanding of the electric field distribution inside the cell, we used the AC/DC module in COMSOL to simulate the electrostatic fields. Here we treated 0.1 mol/L copper sulphate as a solid material with a conductivity 85.9 Sm^{-1} at room temperature. [39]

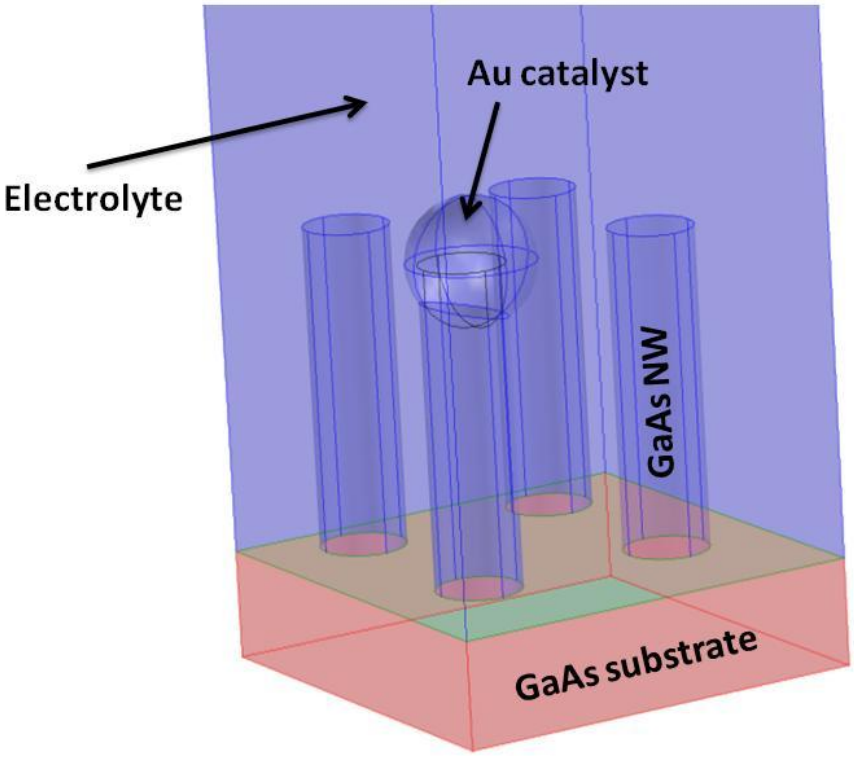

Figure 4.7: Geometry of the electrolytic cell: GaAs substrate and GaAs NWs with or without a Au tip as a cathode. The cell is filled with copper sulphate and there is a platinum anode at the very top.

The cathode consists of GaAs substrate and GaAs NWs with or without a gold catalyst. The current in the domain is controlled by the continuity equation:

$$-\nabla \cdot (\sigma \nabla V) = 0, \tag{4.14}$$

where V is the potential and σ is the conductivity (S/m).

The ground potential boundary is set to be at the platinum/electrolyte interface. External current at a current density of J_e= -100 A/m^2 is applied to the bottom surface of the GaAs substrate. In a stationary coordinate system, the point form of Ohm's law states that:

$$\boldsymbol{J} = \sigma \boldsymbol{E} + \boldsymbol{J_e} \quad . \tag{4.15}$$

$$\boldsymbol{E} = -\nabla V \quad . \tag{4.16}$$

As shown is Fig 4.9, copper sulphate is filled in the cell and the outer boundaries of the domain are insulating:

$$\boldsymbol{n} \cdot \boldsymbol{J} = 0 \tag{4.17}$$

The conductivity of the *n*+ GaAs substrates is set to 10^5 S/m (10^{18}cm^{-3} doping level) and the GaAs NWs to low or high conductivities between of 10^{-3} S/m and 10^6 S/m, respectively.

Simulation results

Fig 4.8 shows the simulation results for two non-conductive GaAs NWs the left one with Au and the right one without Au. We can see that very low current goes through the NWs because the electrolyte is more conductive than the wire in this situation. The electric field is largest at the top part for both NWs with Au and without a Au catalyst.

Figure 4.9 shows the simulation results for conductive GaAs NWs with and without a Au catalyst. The current through the wires is much larger than the current through the electrolyte. The electric field is larger at the top part as well as at the bottom around the NW, which is consistent with our experimentally observed Cu nucleation sites as shown in Figure 3.11. Also the Au catalyst of the left NW attracts more current compared to the one without a Au catalyst on top at right. This model is producing results that more closely match our experiment. The corners at the NW/substrate interface will cause a higher electric field around the bottom of the NW.

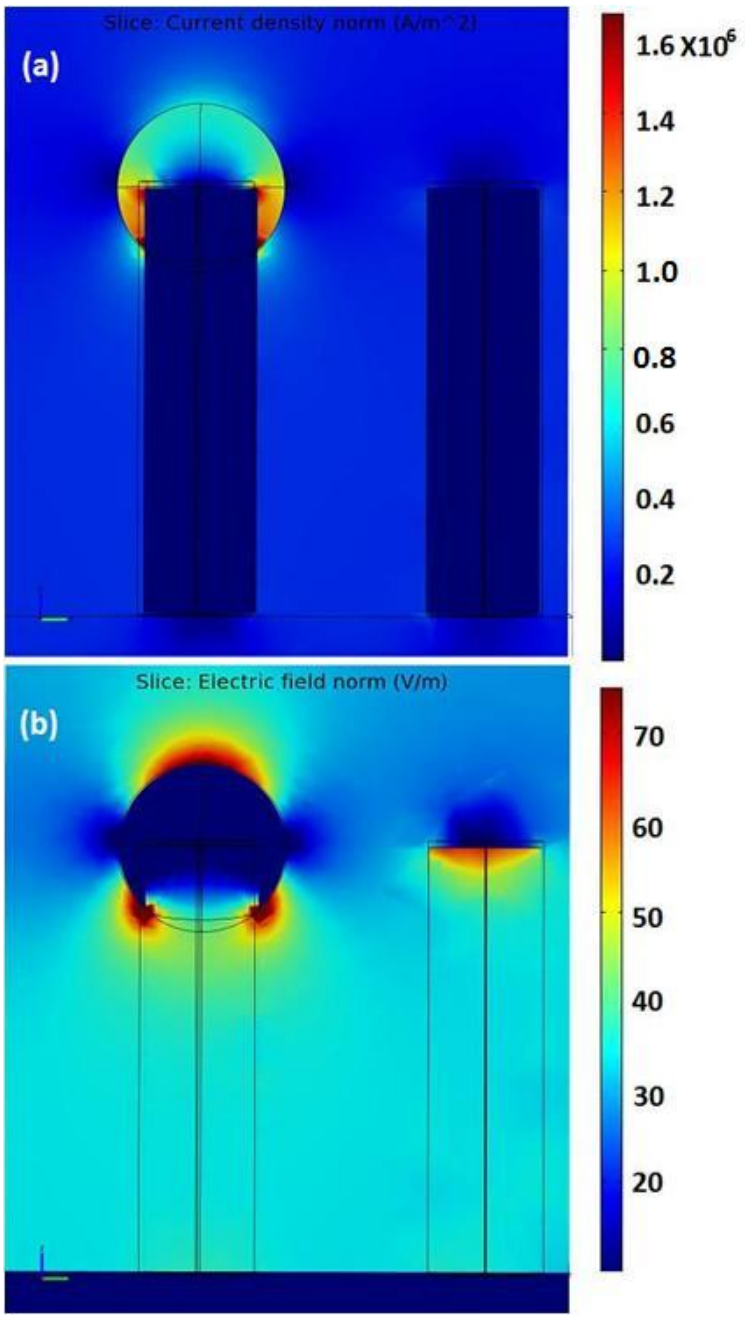

Figure 4.8: Simulation results of (a) current density (A/m^2) and (b) electric field (V/m) distribution in the cell for GaAs NWs with low conductivity 10^{-3} S/m with and without a Au catalyst.

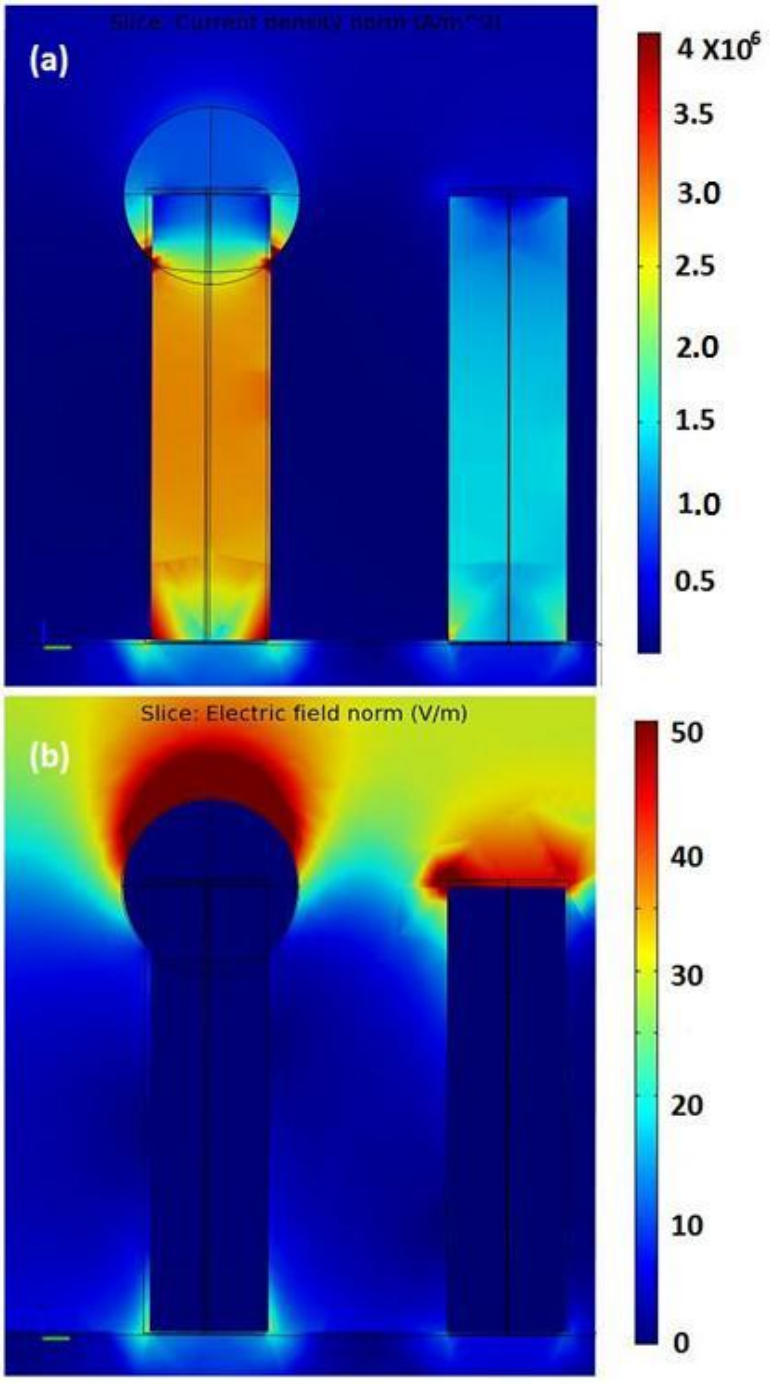

Figure 4.9: Simulation results of (a) current density (A/m^2) and (b) electric field (V/m) distribution in the cell for GaAs NWs with conductivity 10^6 S/m with and without a Au catalyst.

4.3 Other factors important to metal nucleation

4.3.1 Geometry and depletion width

From Fig 3.10 we saw that for type A GaAs NWs with large diameters (~1 μm) copper also nucleated and grew on the GaAs sidewalls NW, right below the Au tip. Conversely, referring to Fig 3.14, we did not find Cu growth on greatly tapered NWs. Furthermore, from measurements of Cu or Fe volume versus wire diameter there was a threshold wire diameter below which the metal did not form. If the wires were of identical conductivity and length then the current density would have been the same. However, the total current available for nucleation will eventually be too small for smaller wires for nucleation to succeed. Alternatively, if the wire conductivity is a function of diameter decreasing with decreasing size, then smaller wires would become too resistive for nucleation. Although the electric field is theoretically higher at smaller wire tips, their shrinking cross-sectional area and increasing resistance, lowers the available current.

On the other hand, the sidewall Cu growth of the type A GaAs NWs with large diameters (~1 μm) in Fig 3.10 means these wires with large diameter are more conductive than the wires with small diameters, which indicates that they are not fully depleted. Thus, the depletion width is between 65 nm and 400 nm if we assume there is a 200 nm conductive core for the 1 μm diameter wire. The depletion width for GaAs NWs can be calculated as [40]:

$$d = \sqrt{\frac{2\varepsilon_0 \varepsilon_r V_s}{en}} \quad , \tag{4.18}$$

where n is the concentration of charge carriers, ε_r = 13.1 is the relative permittivity of GaAs and V_s = 0.45 V is the surface potential for p-GaAs [41]. If we reverse the

calculation assuming d = 65 to 400 nm we get a carrier concentration in the range of 3.7 x 10^{15} cm^{-3} and 1.4 x10^{17} cm^{-3}. If we do the same calculation for the core-shell GaAs NWs discussed in 3.2.3, whose depletion width should be smaller than 40 nm, the relative calculated carrier concentration is larger than 3 x 10^{17} cm^{-3}. These values for the actual C-dopant impurity concentration for CBr_4 MOVPE growth are more consistent with planar results.

4.3.2 Gold catalysts

In section 3.6.2 we showed that Cu still prefers to grow on the ends of the NW even after we etched off the Au catalysts. This indicates that either the gold was not all removed or that gold is not necessary for the Cu tip nucleation. However, we do see Cu nucleation on NWs of smaller diameters (< 100 nm) with Au catalysts still there, which we do not see as frequently for NWs of the same diameter without Au catalysts. This is again likely due to the increased conductivity of Au versus the semiconductor , as discussed in section 1.2. Without a Au catalyst on the top end, the NW still has to face a depletion region at the semiconductor/electrolyte interface. The current of the smaller diameter NW is not large enough to form a stable nucleus.

4.3.3 Overpotential

Cu electrodeposition is reversible, but there is a minimum nucleus size necessary for continued metal growth [42]. The number of Cu ions, N, in each critical nucleus is a function of the overpotential:

$$N_{crit} = \frac{\pi \varepsilon^2 s}{(ze_0\eta)^2} \tag{4.19}$$

where *s* is the area of one metal atom, and *z* is the number of electrons each ion carries (2 for Cu^{2+}). We can see that the size of the critical cluster will decrease as the overpotential increases. On the other hand, if we apply an extra high overpotential, the current through the NW will increase, thus increasing the number of electrons that tunnel through the depletion barrier.

Figure 4.10 shows the experimental results for Cu deposition on GaAs NWs with an extra large current density, i.e. large overpotential. Cu growth can be detected around the NW extending into dendrites growing out the top of the NW.

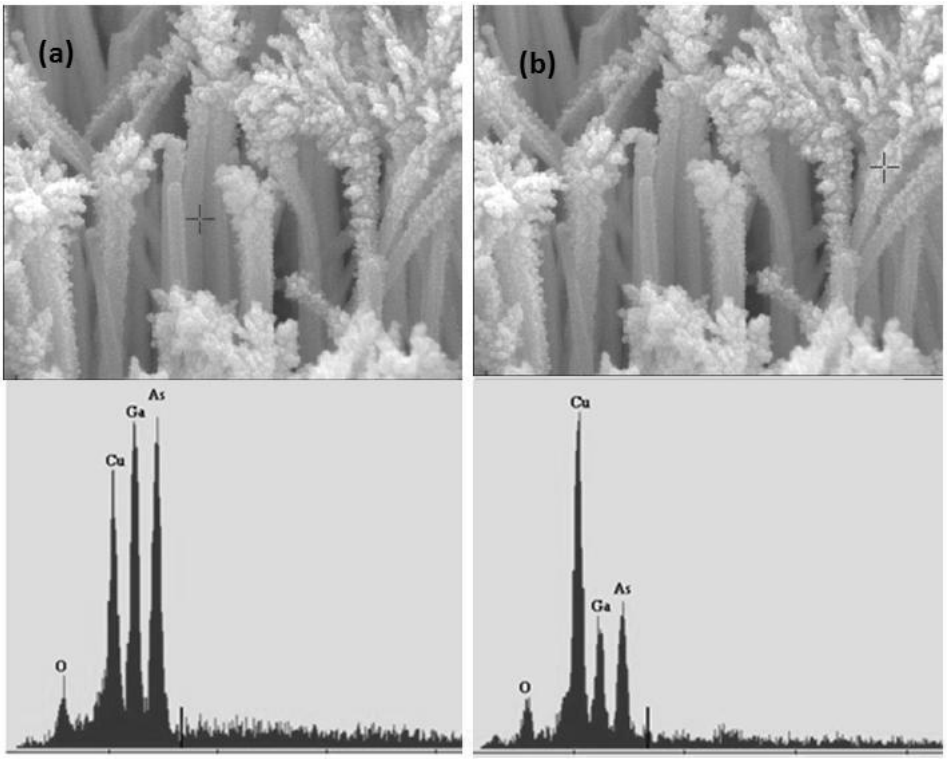

Figure 4.10: SEM image of GaAs NWs after Cu deposition for 5 s with 40 mA/mm2 current density and relative EDS spectrum from two different spots of the GaAs NW.

4.4 Sample surface

In this section, we focus on the chemical composition of the electrode surface in our experiments.

4.4.1 Surface oxidation

A previous report found Ni growth only on the Au catalysts at the top end of P-doped Si NWs. After removing the Si NW surface oxide (1% HF), they found Ni particles also deposited along the sidewalls of the NWs [43]. They concluded that the surface oxide on their *p*-doped Si NWs, acted as an insulating layer which prevented metal deposition on the sidewalls.

In our experiment, a dilute ammonium hydroxide solution was used to etch the GaAs NW surface oxide. Contact angle measurements indicated that the resulting surfaces of the NW samples were then hydrophilic. Yet for the unintentionally-doped GaAs NWs, Cu electrodeposition also occurred predominantly only at the Au ends of the wire. Was this due to poor oxide etching, poor wetting of the NWs by the electrolyte, or simply poor NW conductivity? Evidence that the electrolyte reached the substrate is that Cu electrodeposition was also visible at the bottom of unintentionally-doped GaAs NWs. Once the wires were of higher conductivity, including the core-shell doped GaAs NWs and InAs NWs, we found Cu growth around the sidewalls to the substrate. This further supports the conclusion that surface oxides were removed by ammonium etching in all cases, and that the NWs were completely immersed in the electrolyte for both InAs and GaAs NWs. Variations in the location of metal growth were due to variations in wire conductivity.

We know GaAs in the ambient environment forms a layer of native oxides, a mixture of Ga_2O_3 and As_2O_3. This electrically insulating layer could inhibit or prevent entirely sidewall Cu growth. Also gold does not oxidize in air or water. Thus, as a suggestion for a future experiment, leave the oxide on the wire, remove organic impurities with ethanol instead of ammonium hydroxide, then tip only deposition should be feasible.

4.4.2 Incorporation of carbon

Our results indicate that Cu grows only around the Au catalyst at the top end of undoped GaAs NWs and doped GaAs NWs, while Cu grew along the length of core-shell doped GaAs NWs. The most likely conclusion is that the degree of carbon doping that occurs during the VLS NW growth is much lower than during the growth of a shell onto an existing GaAs core. In VLS-doped NWs the carbon concentration is too low to make sufficient difference to the conductivity.

4.5 Cu contact for *I-V* measurement

The initial purpose of this project was to make ohmic contacts for NW *I-V* measurements. A tungsten probe tip was installed inside the SEM so that individual wires could be contacted. The probe radii are about 150 nm, much larger than the diameter of most of our GaAs NWs. Fig 4.11 shows that a large copper contact provides a larger contact surface, makes the contact process easier and more visible, compared to trying to contact the smaller Au catalyst directly without a copper contact. Measurements of *I-V*

from individual NWs is left for future work.

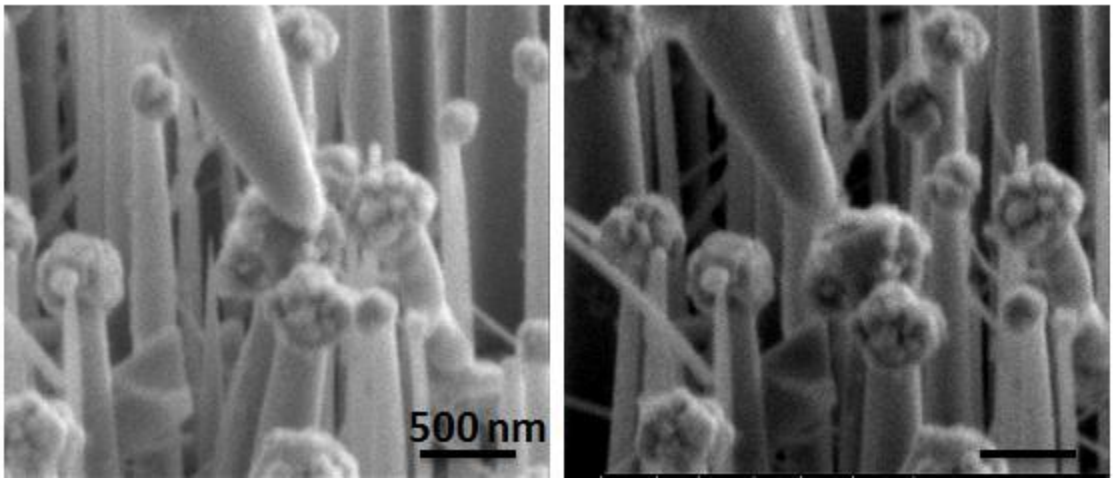

Figure 4.11: SEM images of a nanoprobe touching electrodeposited Cu on a GaAs NW head.

5: SUMMARY

For low-doped (non-conductive) NWs, both COMSOL simulation and experimental results find that electrodeposition happens at the top part of the NW, as shown in Figure 5.1. This preferential growth is due to a large depletion region barrier on the semiconductor sidewalls and the higher electric field on the NW top. The top growth preference did not change when we removed the gold catalyst, as shown in Figure 3.27. The square in the figure is the sample substrate while the grey bar represents a low-doped NW. The deposited metal is represented by the darker regions.

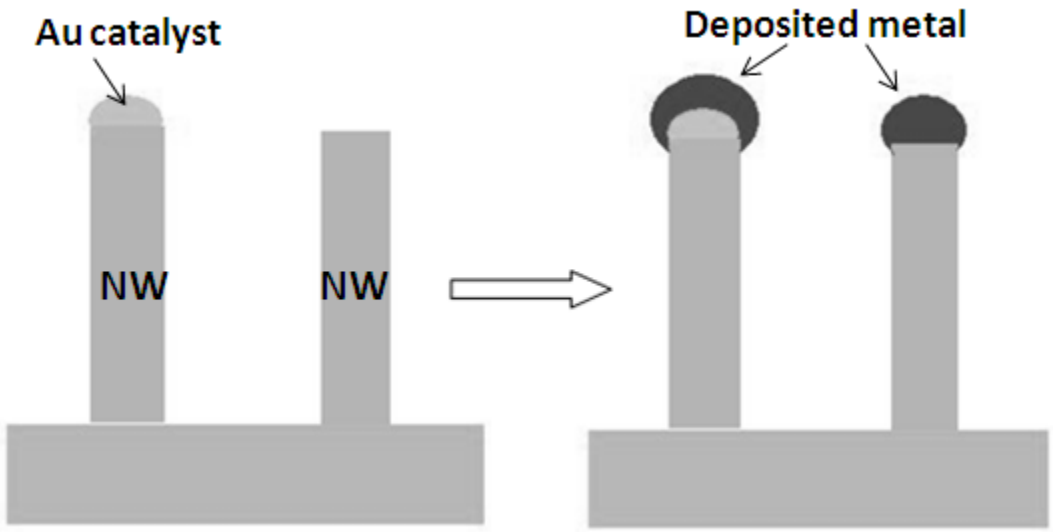

Figure 5.1: Sketch of low-doped NW sample before and after electrodeposition.

For our individual GaAs NW samples, we found Cu or Fe grows preferentially on top of the gold particles used for GaAs nanowire growth. Copper was epitaxial whereas iron was randomly oriented. Removal of the gold catalyst did not change the location of preferential growth.

Sidewall deposition on low-doped NWs can be achieved by applying higher current density (higher overpotential) within a short time. Three electrode systems are required for further investigation of the relationship between cathode overpotential, deposition time and film thickness.

For highly-doped (conductive) NWs, we would expect metal deposition everywhere around the wire, and a large head growth if there is a Au catalyst at the end, as shown in Figure 5.2. Sidewall metal growth should be prevented by keeping the native-oxide film around the nanowire. For GaAs NW sample, this might be achieved by etching the sample with ethanol instead of ammonium hydroxide right before deposition. Future experiment needs to be done to test this.

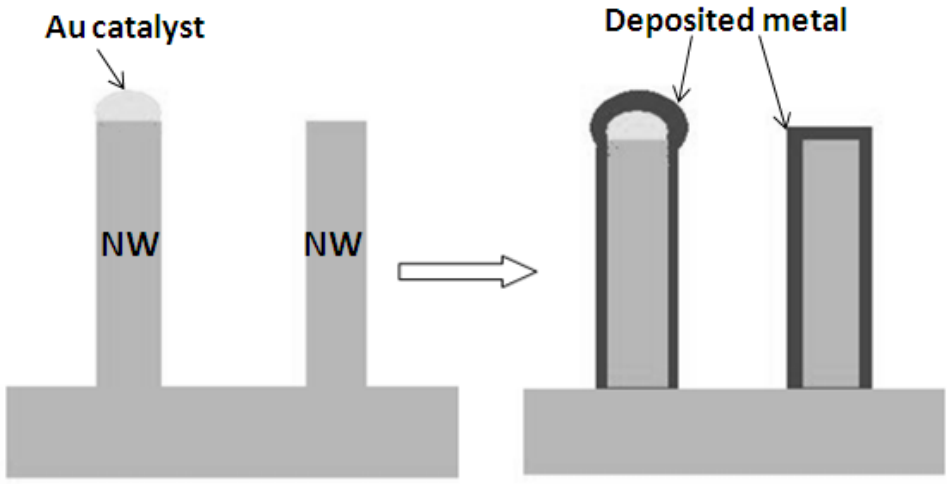

Figure 5.2: Sketch of highly-doped NW sample before and after electrodeposition.

A summary of the experimental results regarding metal nucleation locations for all samples investigated is shown in Table 2.1.

Through our experiment on GaAs NWs, we can conclude that direct carbon-doping of GaAs shell layers is more effective than carbon-doping via the Au catalyst (C-doped Type A or B). The effective resistivity of the undoped and CBr_4 doped NWs was estimated to be 10^3 Ωm and 10^4 Ωm, respectively, limited by surface depletion. Three electrode, potentiostatic electrodeposition systems might be useful for a more precise control of GaAs surface voltage, and thus rate of metal nucleation.

APPENDICES

Appendix A : Potential time relation

The potential drop across the deposition cell has been recorded during electrodeposition. Figure A. 1 shows plots of potential versus time for seven different experiments. We can see that it usually takes 2~3 seconds for the voltage to become stable. The voltage change for Au nanoparticle samples was different compared to the NWs whether GaAs or InAs. The potential dropped abruptly during the first 8 s then gradually decreased further to a stable value. While for all other samples, the potential dropped to a minimum value at the first 5 s as we immersed our samples into the electrolyte, and then increased gradually towards a constant value likely due to the establishment of diffusion-limited Cu ion transport in the electrolyte. This difference might be due to the nature of the electrolyte diffusion profiles for a flat substrate compared to nanowires. Another factor might be that the contact area of the Au NP/semiconductor interface increases as deposition goes on if Cu began to deposit directly on the GaAs substrate.

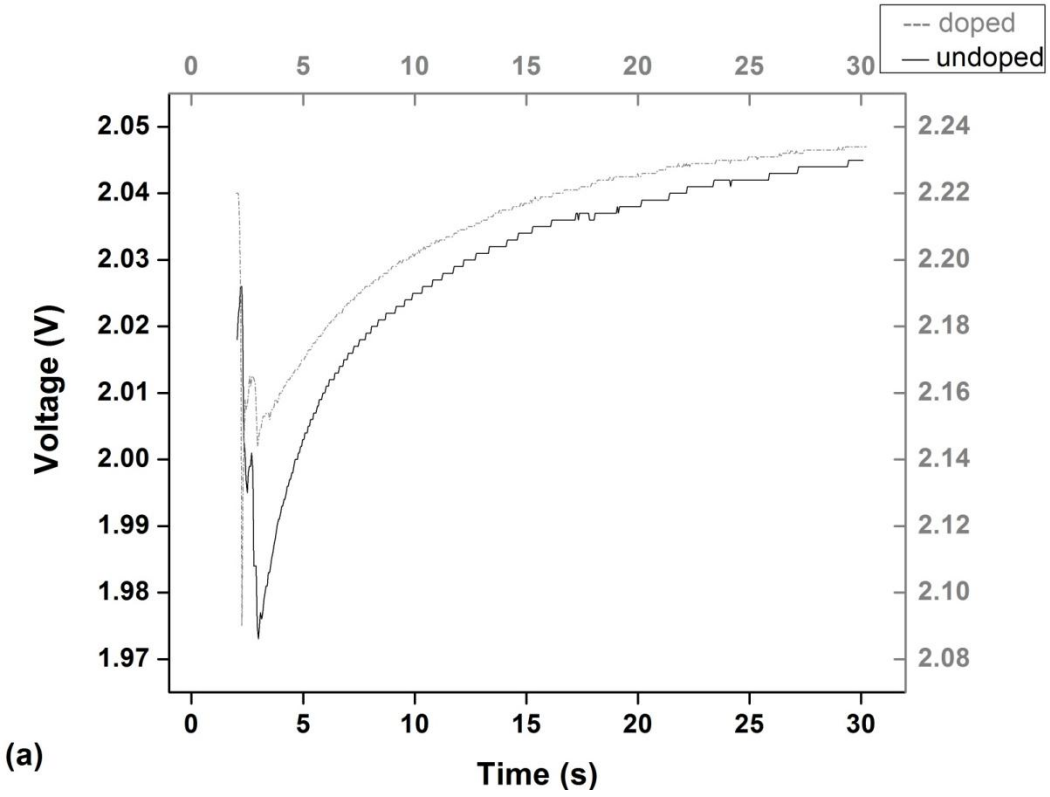
--- doped
— undoped
Voltage (V)
Time (s)

(a)

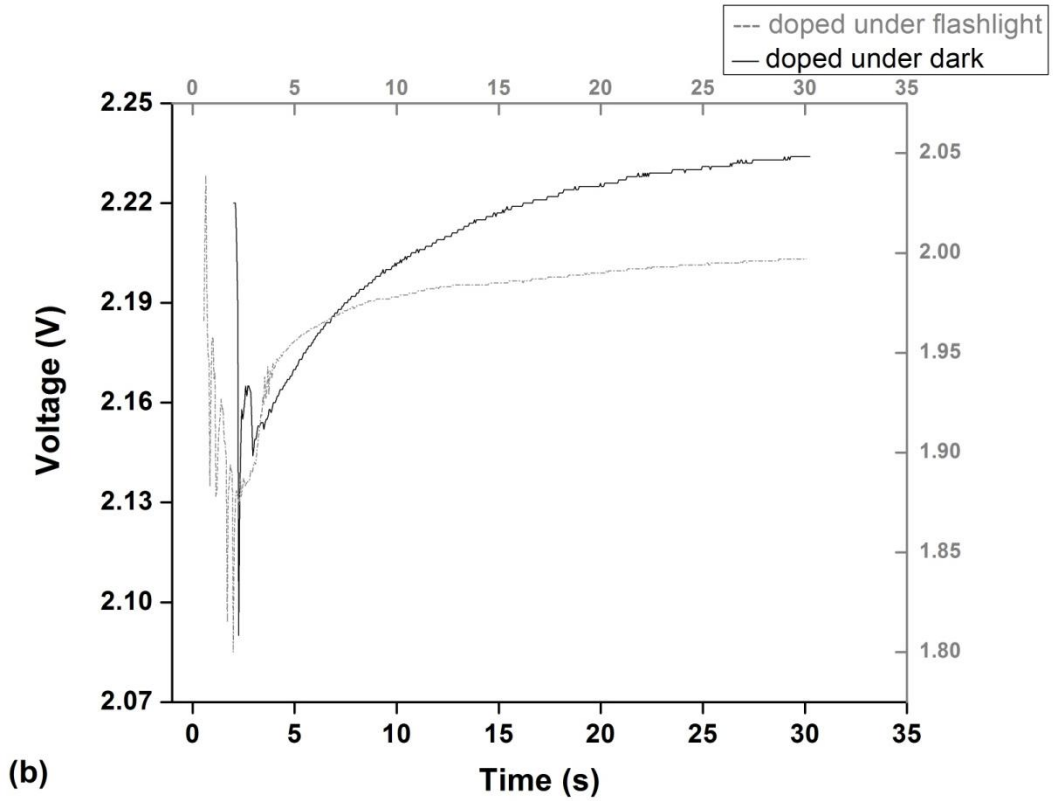
--- doped under flashlight
— doped under dark
Voltage (V)
Time (s)

(b)

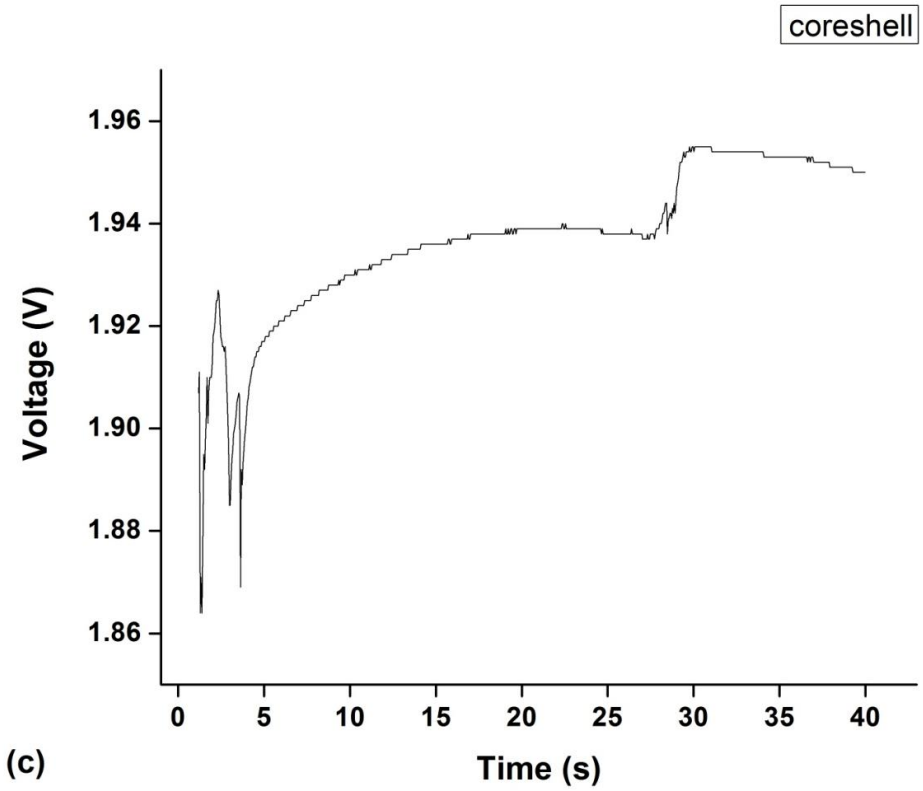
coreshell
Voltage (V)
1.96
1.94
1.92
1.90
1.88
1.86
0
5
10
15
20
25
30
35
40
Time (s)

(c)

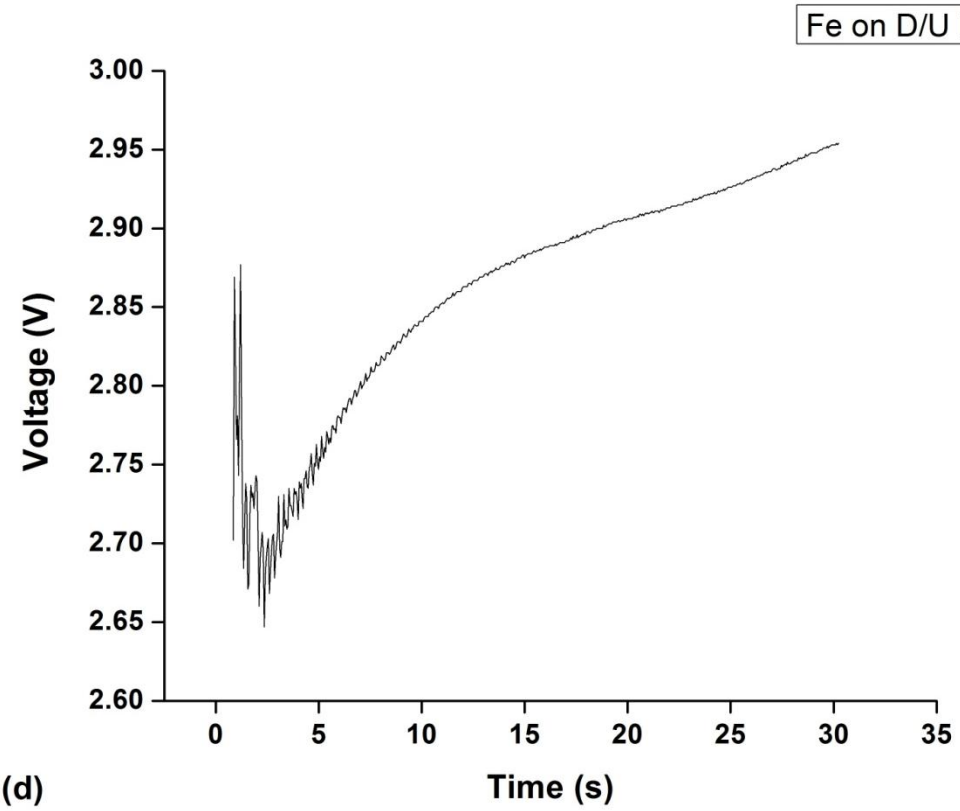
Fe on D/U NWs
Voltage (V)
3.00
2.95
2.90
2.85
2.80
2.75
2.70
2.65
2.60
0
5
10
15
20
25
30
35
Time (s)

(d)

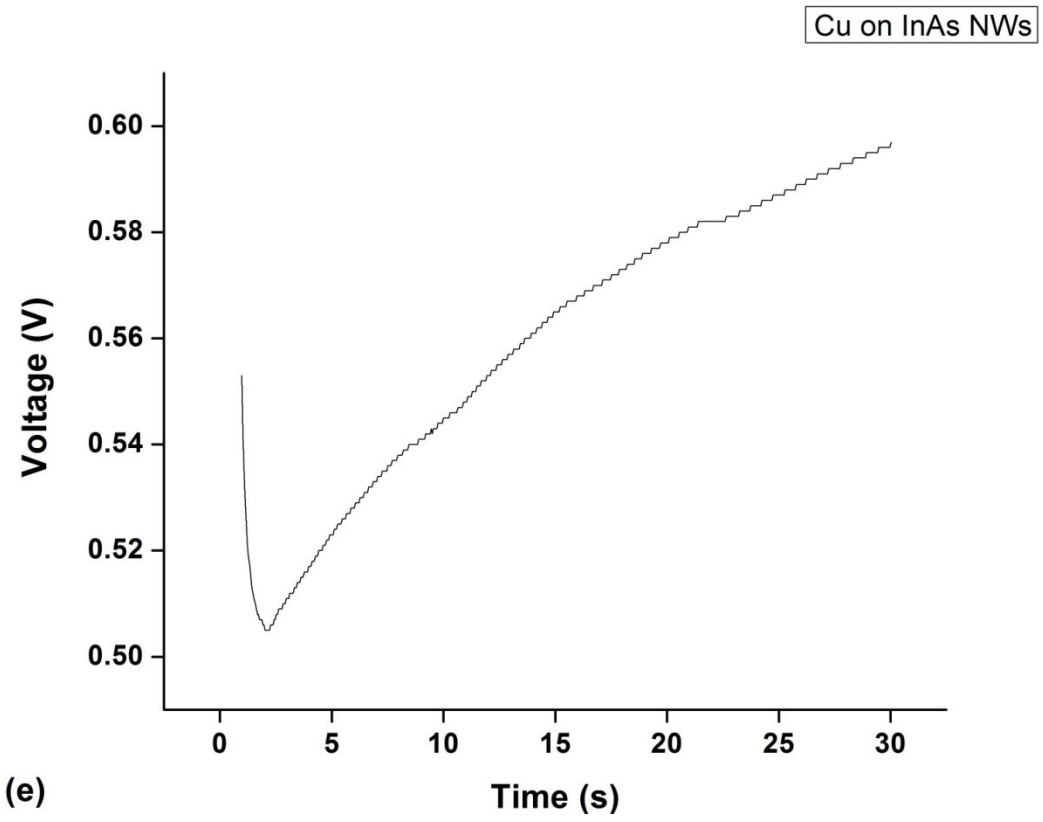
Cu on InAs NWs
Voltage (V)
0.60
0.58
0.56
0.54
0.52
0.50
0
5
10
15
20
25
30
Time (s)

(e)

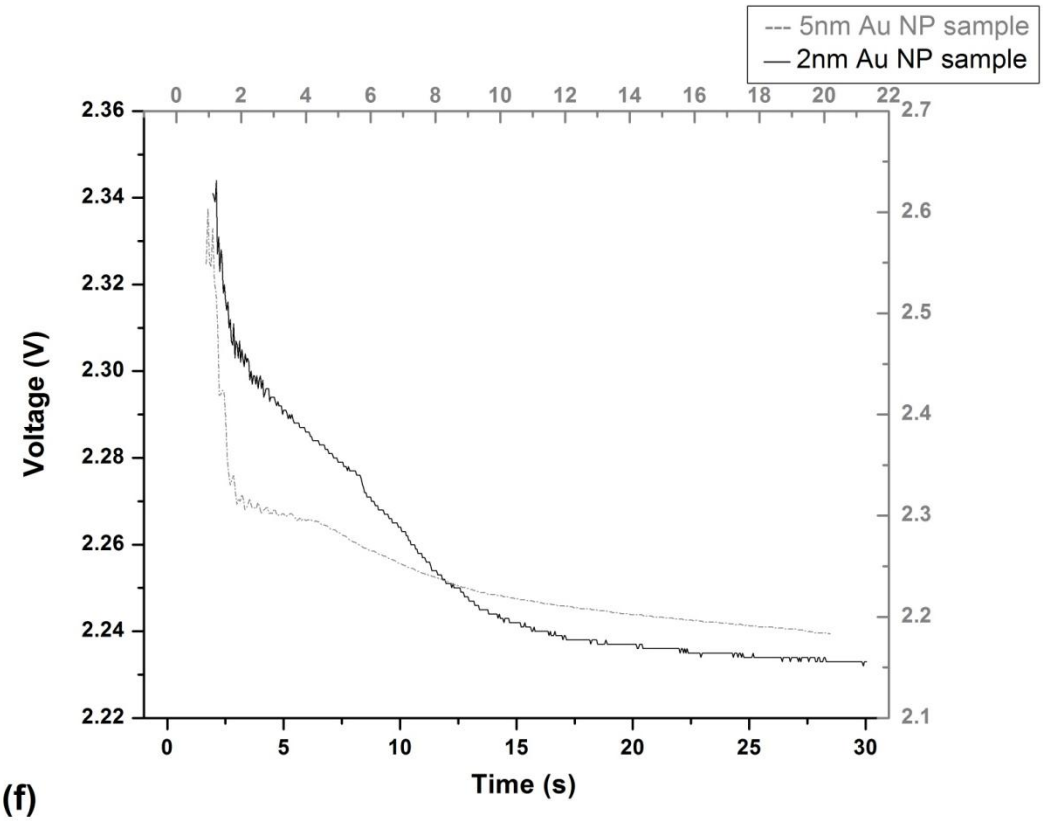
--- 5nm Au NP sample
— 2nm Au NP sample
Voltage (V)
2.36
2.34
2.32
2.30
2.28
2.26
2.24
2.22
0
2
4
6
8
10
12
14
16
18
20
22
2.7
2.6
2.5
2.4
2.3
2.2
2.1
0
5
10
15
20
25
30
Time (s)

(f)

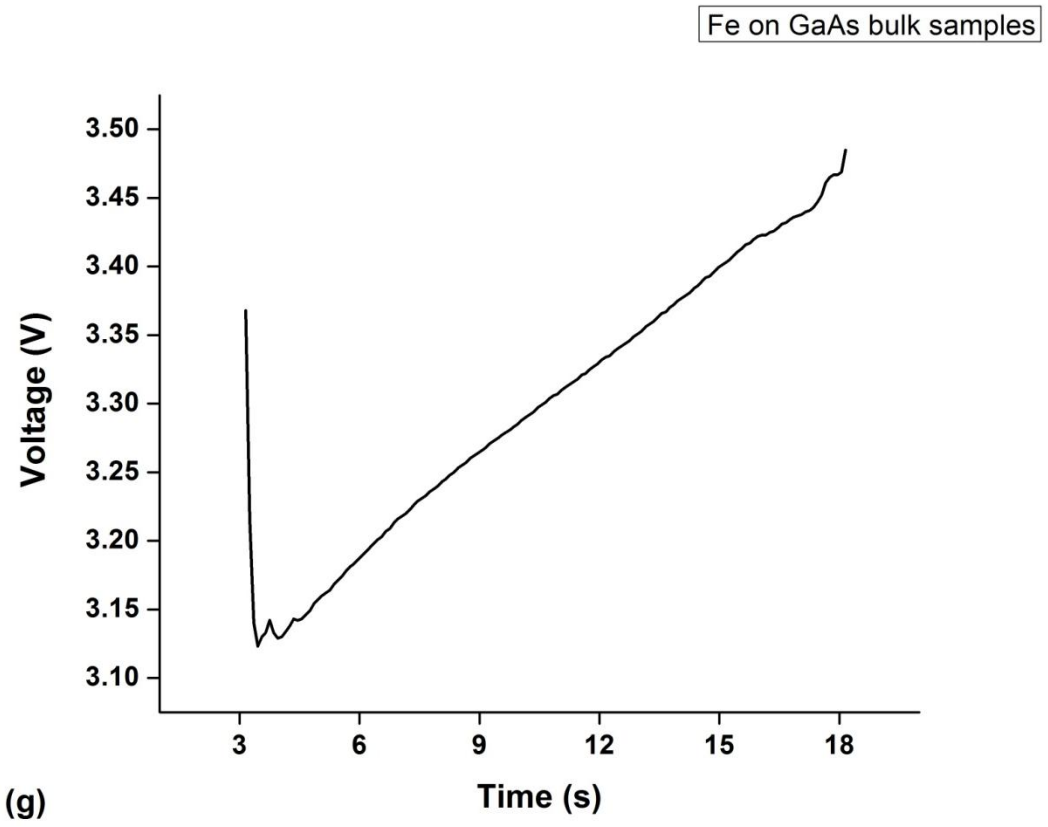

Figure A.1: Potential change as a function of deposition time for: (a) Cu deposition on Type B GaAs NWs with CBr_4 or without CBr_4, (b) Cu deposition on Type B GaAs NWs with CBr_4 in the dark or illuminated with a LED flashlight, (c) Cu deposition on core shell GaAs nanowires. The sample was lifted up a bit (thus reaction area decreased) at 27 s after the start of deposition. (d) Fe deposition on Type A doped/undoped GaAs NWs. (e) Cu deposition on InAs NWs from NRC. (f) Cu deposition on Au nanoparticle samples with 2 nm and 5 nm Au thickness before annealing and (g) Fe deposition on GaAs bulk samples.

BIBLIOGRAPHY

[1] M. Bockrath, D. H. Cobden, P. L. McEuen, N. G. Chopra, A. Zettl, A. Thess, and R. E. Smalley, Science 275, 1922 (1997).

[2] Y. Cui, X. Duan, J. Hu, and C. M. Lieber , J. Phys. Chem. B 104, 5213 (2000).

[3] Stephen B. Cronin, Yu-Ming Lin, Oded Rabin, Marcie R. Black, Jackie Y. Ying, Mildred S Dresselhaus, Pratibha L Gai, Jean-Paul Minet and Jean-Paul Issi, Nanotechnology 13, 653 (2002).

[4] S.Ingole, P.Aella, S.J.Hearne, and S.T.Picraux, Appl. Phys. Lett. 91, 033106 (2007).

[5] S.Ingole,P.Manandhar, J.A.Wright, E.Nazaretski, J.D.Thompson, and S.T.Picraux, Appl. Phys. Lett. 94, 223118 (2009).

[6] Hohn OM. Bockris, Amulya K.N.Reddy, Maria Gamboa-Aldeco, Modern Electrochemistry, 2nd edition, Kluwer Academic (1998).

[7] John C. Kotz, Paul Treichel and Gabriela C. Weaver, Chemistry and chemical reactivity, Cengage Learning (2006).

[8] Michio Okamura, Electric Double Layer Capacitors and Power Storage Systems, Nikkan Kogyo Shimbun Ltd. (2001).

[9] Santos, Elizabeth and Schmickler, Interfacial electrochemistry, 2nd edition, Springer (2010).

[10] Z. L. Bao, S. Grist, S. Majumder, L. B. Xu, E. Jensen, and K. L. Kavanagh, J. Electrochem. Soc. 156 (2009) D138.

[11] Zhi Liang Bao, K. L. Kavanagh , J. Appl. Phys. 98, 066103 (2005).

[12] O Salehzadeh and S P Watkins, Nanotechnology 22, 165603 (2011).

[13] O. Salehzadeh, S.P. Watkins, J. Crystal Growth 325, 5 (2011)

[14] T.S.Chow, J. Phys.: Condens. Matter, 10, 27 (1998).

[15] Yu-Hung Cheng, C.K Chou, C. C. Chen, and S.Y.Cheng, Chem. Phys. Lett. 397, 17 (2007).

[16] C.-T. Lee, K.-L. Jaw and C.-D. Tsai, Solid-State Electronics 42, 871 (1998).

[17] S. Osakabe and S. Adachi, J. Electrochem. Soc. 144, 290 (1997).

[18] K. Sefiane , L. Tadrist, and M. Douglas, Int J Heat Mass Tran 46, 4527 (2003).

[19] Don W.Green and Robert H.Perry, Perry's Chemical Engineer's Handbook, McGraw-Hill Professional (1984).

[20] MicroChemicals, Germany "Wet Chemical Etching of Gold." http://www.microchemicals.eu/technical_information

[21] B.L. Weiss, J. Mater Sci. 11, 1596 (1976).

[22] Jacob H. Woodruff, Joshua B. Ratchford, Irene A. Goldthorpe, Paul C. McIntyre, and Christopher E.D. Chidsey, Nano Letters 7,1637 (2007).

[23] S. Thunich, L. Prechtel, D. Spirkoska, G. Abstreiter, A. Fontcuberta i Morral, and A. W. Holleitner, App. Phys. Lett. 95, 08311(2009).

[24] Raffaella Calarco, Michel Marso, Thomas Richter, Ali I. Aykanat, Ralph Meijers, Andre´ v.d. Hart, Toma Stoica, and Hans Luth, Nano Letts 5, 981 (2005)

[25] Ronald H. Micheels, Allan D. Darrow and R. David Rauh, Appl. Phys. Lett. 39, 418 (1981).

[26] Saulius J, Akira Y, Hidekazu I, Shigeki M, Hitoshi T, and Hiroaki M, Jpn. J .Appl. Phys. 40, 4246 (2001) .

[27] Hung-Chun Lo, Yi-Fan Huang, Surojit Chattopadhyay, Chih-Hsun Hsu, Chia-Fu Chen, Huei-Hsien Chen and Li-Chyong Chen Nanotechnology 17, 2542 (2006).

[28] David B.Williams and C. Barry Carter, Transmission Electron Microscopy, Plenum Press (1996).

[29] Yang Tang, Dongxu Zhao, Jie Chen, Nelia Wanderka, Dezhen Shen, Fang Fang, Zhen Guo, Jiying Zhang, and Xiaohua Wang, Mater Chem Phys. 121, 541 (2010).

[30] Justin J. Hill, Kelly Haller, Brittany Gelfand, and Kirk J. Ziegler, ACS Appl. Mater. 2, 1992 (2010).

[31] MTchernycheva, J C Harmand, G Patriarche, L Travers and G E Cirlin, Nanotechnology 17, 4025 (2006).

[32] Taleb Mokari, Eli Rothenberg, Inna Popov, Ronny Costi and Uri Banin, Science, 304, 1787(2004).

[33] O.S. Einabad. Carbon doping of GaAs nanowires. Master's Thesis, Department of Physics, Simon Fraser University, 2010.

[34] S.M. Sze and J.C. Irvin, Solid State Electronics 11, 599 (1968).

[35] Michael J. Tambe, Shenqiang Ren, and Silvija Gradecˇak, Nano Letts. 10, 4584 (2010).

[36] COMSOL Model Gallery, "Copper deposition in a trench" http://www.comsol.fi/showroom/gallery/2112/

[37] Alexandra C. Ford, Johnny C. Ho, Yu-Lun Chueh, Yu-Chih Tseng, Zhiyong Fan, Jing Guo, Jeffrey Bokor and Ali Javey, Nano Lett., 9, 360 (2009).

[38] E.Mattson and J.O'M. Bockris, Trans. Far. Soc. 55, 1586 (1959).

[39] Marija Besˇter-Rogac, J. Chem. Eng. Data 53, 1355 (2008).

[40] D. Stichtenoth, K. Wegener, C. Gutsche, I. Regolin, F. J. Tegude, W. Prost, M. Seibt and C. Ronning. Appl. Phys. Lett. 92, 163107 (2008).

[41] L. G. Meiners, Appl. Phys. Lett. 33, 747 (1978).

[42] A.A. Yasseri, S. Sharma, T.I. Kamins, Z. Li and R. Stanley Williams, Appl. Phys. A. 82, 659 (2006).

[43] Ingole, S. Manandhar, P. Wright, J. A. Nazaretski, E. Thompson, J. D. Picraux, S. T. Appl. Phys. Lett, 94, 223118 (2009).